Image analysis for realistic electromagnetic

imaging systems

by

Mabel Delice Rámirez Vélez

B.S., University of Puerto Rico at Mayaguez, 2002

M.S., University of Puerto Rico at Mayaguez, 2003

A thesis submitted to the

Faculty of the Graduate School of the

University of Colorado in partial fulfillment

of the requirements for the degree of

Doctor of Philosophy

Department of Electrical and Computer Engineering

2009

This thesis entitled:

Image analysis for realistic electromagnetic imaging systems

written by Mabel Delice Rámirez Vélez

has been approved for the Department of Electrical and Computer Engineering

_____

Prof. Zoya Popović

_____

Prof. Mark Hernández

Date _____

The final copy of this thesis has been examined by the signatories, and we

Find that both the content and the form meet acceptable presentation standards

Of scholarly work in the above mentioned discipline.

Rámirez Vélez, Mabel Delice (Ph.D., Electrical Engineering)

Image analysis for realistic electromagnetic imaging systems

Thesis directed by Prof. Zoya Popović

This thesis focuses on the choice and implementation of different image and signal processing algorithms adapted to address specific hardware challenges in realistic electromagnetic imaging systems and their applications. A wide range of imaging systems and frequencies with related image processing needs is studied: (1) low-frequency medical brain activity imaging at kHz frequencies for epileptic seizure detection; (2) near-field microwave scanning in the several hundreds of MHz range for non-destructive silicon chip defect detection; (3) Synthetic Aperture Radar (SAR) in the 8-12GHz band for automatic focusing of ground maps; (4) multispectral infrared and visible images for embedded target detection; and (5) passive broadband imaging from 100GHz to several THz for concealed weapon detection.

As with many imaging systems and object recognition applications, there exists a need for pre-processing raw data provided by the imager to improve the quality of the measured scene. In the cases studied in this work, the following limit the image quality and processing requirements: high data dimensionality; low signal-to-noise ratio; scanning position drifts; unknown target characteristics; low number of pixels; broadband integration; and detector non-uniformities. In the widely published fields of image processing and imaging systems, the design of image processing algorithms that match hardware limitations has been lacking, and this is precisely what is addressed in this thesis. The techniques used in this work, as they apply to the five imaging systems listed above, include:

- dimensionality reduction based on principal component analysis and Laplacian Eigenmaps, applied to epilepsy detection and multispectral IR imaging;

- two dimensional interpolation using windowing and filtering, applied to near-filed scanning, SAR and THz imaging;

- manifold learning and classification, applied to epilepsy detection, multispectral IR and THz imaging;

- dynamic background correction and contrast enhancement, applied to THz imaging; and

- thresholding, applied to data obtained by all five imaging systems.

These image and signal analysis techniques are presented in this thesis as an approach to finding an integrated set of solutions addressing hardware and sensor platform limitations. The trade-offs between performance and optimality of an algorithm solution were considered, with the need for pseudo-real time analysis in most cases.

Dedication

Acknowledgments

Contents

Bibliography   128

List of Figures

List of Tables

Chapter 1

Introduction

This thesis focuses on the choice and implementation of different image and signal processing algorithms adapted to address specific hardware challenges in realistic electromagnetic imaging systems and their applications. A wide range of imaging systems operating over most of the electromagnetic spectrum , all with related image processing needs, is studied as summarized in Table 1.1.

Starting from the low frequency end, brain activity imaging at kilohertz (**kHz**) frequencies obtained with 64 scalp electrodes was processed for epileptic seizure detection. This required non-linear processing and was done in collaboration with Dr. Mark Spitz from the University of Colorado - Health Sciences Center, Prof. Dan S. Barth from the University of Colorado Psychology Department and Prof. François G. Meyer from the University of Colorado, Electrical, Computer and Energy Engineering Department. The scalp electroencephalogram (EEG) is a powerful tool for neurophysiology and has been used extensively to study epilepsy. Modern EEG systems can use up to 128 electrodes to sample and record the time domain electrical activity of the brain [1]. The signals from the electrodes are mixtures of neural signals and thus, some signal processing needs to be applied in order to separate them and detect a seizure. Usually, the EEG recordings are assumed to be a linear combination of and the detection is done by clinicians by visual inspection of the EEG recordings. This thesis examines the validity of this assumption by comparing the effectiveness of linear and non-linear processing

Table 1.1: Realistic electromagnetic imaging systems operating over most of the electromagnetic spectrum and the related image processing needs discussed in this thesis

Frequency	Application	Collaboration	Modality	Resolution	Processing	Outcome
kHz	medical (EEG)	UC-HSC	passive, near-field	temporal/ spectral (1 Hz)	PCA+ nonlinear mapping	seizure detection
MHz	defect detection	NIST (EM)	active, near-field	spatial (μm)	upsampling interpolation	sub-surface detection
GHz	ground mapping	MIT-Lincoln Laboratory	active, far-field	spatial (m)	filtering, thresholding	auto-focusing
THz	security	NIST (OE)	passive, far-field	spatial (cm)	filtering, interpolation segmentation	concealed weapon detection
10^3 THz	defense	LMCO	passive, far-field	spatial (m)/ spectral ($\lambda \approx \mu$m)	PCA+ nonlinear mapping	target detection

for epileptic seizure detection.

In the megahertz (**MHz**) range, images from near-field microwave scanning for non-destructive chip defect detection were processed in order to improve resolution, signal-to-noise ratio, and enhance sub-pixel features. This work was done in collaboration with Jonathan D. Chisum in the Microwave Group and Dr. Pavel Kabos' group in the Electromagnetics Division at NIST. Near-field microwave probing has been used in the past few decades for material property measurements by loading a resonant circuit with the unknown material, usually in the form of a planar slab [2–4]. For example, small microstrip probes implemented at 900 MHz were used for metal conductivity measurements [4]. The probing system described in this work had the goal to dramatically reduce the size of the resonant probe circuit while preserving the main performance metrics, such as high quality factor and detection of very small features. The resolution of the images obtained with this method is limited by the size and height of the probe

and without interpolation, and filtering of the raw data sub-surface features were not detectable.

In the gigahertz (**GHz**) range, autofocus post-processing for X-band Synthetic Aperture Radar was applied to processed radar data in order to eliminated errors due to uncompensated motion of the aircraft carrying the radar. This work was done in collaboration with Dr. Gerald Benitz from the MIT Lincoln Laboratory, Intelligence, Surveillance and Reconnaissance Group. The algorithms described in this thesis were included in the LiMIT SAR Testbed, which is used for high resolution ground mapping. Existing autofocusing techniques such as eigenvector phase gradient autofocus algorithm [5] were used as a starting point and the modification detailed in this thesis includes wavelet denoising and thresholding which improves correction for uncompensated motion errors.

In the terahertz (**THz**) range, single pixel and linear array broadband passive radiometric images with poor SNR and low pixel count were processed to enable visual concealed weapon detection. This collaboration was made possible by Dr. Erich Grossman and Dr. Charles R. Dietlein in the Optoelectronics Division at NIST, where the millimeter wave and terahertz passive imagers were developed and calibrated [6–8]. For concealed weapon detection (CWD) and security, active systems are usually seen as a health threat and cause privacy concerns. Hence, passive millimeter wave imaging systems have become preferable in settings such as airport security check points. Recently, several passive millimeter wave imaging systems were set up in selected airports across the United States for testing and checking passengers for concealed objects [9]. The automation of the detection process is essential and can aid personnel security by offering faster and more accurate image analysis. Classical image processing, pattern recognition, and target detection techniques are well fitted for the CWD application.

Finally, in the infrared and visible range ($\sim$**1000THz**), multispectral narrowband images were processed by non-linear classification and dimensionality reduction to enable embedded target detection [10]. This work was done in collaboration with Lockheed Martin in Boulder, Colorado and Prof. François G. Meyer. The application for

this work was plume detection for missile seekers. In general, multispectral and hyperspectral sensors acquire a large amount of spectral information, e.g., Airborne Visible/Infrared Imaging Spectrometer (AVIRIS) obtains data between $0.4\,\mu$m to $2.45\,\mu$m at $10\,$nm intervals in 224 channels. For specific targets a subset of this information is needed and dimensionality reduction is used to speed up the processing and remove noise in non-relevant bands.

As with many imaging systems and object recognition applications, there exists a need for processing raw data provided by the imager to improve the quality of the measured scene. In the cases studied in this work, the following limit the image quality and processing requirements: high data dimensionality; low signal-to-noise ratio; scanning position drifts; unknown target characteristics; low number of pixels; broadband integration; and detector non-uniformities. In the widely published fields of image processing and imaging systems, the design of image processing algorithms that match hardware limitations has been lacking, and this is precisely what is addressed in this thesis. The techniques used in this work, as they apply to the five imaging systems listed above, include:

- Dimensionality reduction based on principal component analysis and Laplacian Eigenmaps, applied to epilepsy detection and multispectral IR imaging. These are a combination of linear and nonlinear methods that operate on data when temporal (frequency) resolution is of interest [11, 12].

- Two dimensional interpolation using windowing and filtering [13], applied to near-filed scanning, SAR and THz imaging;

- Manifold learning and classification [10, 12], applied to epilepsy detection, multispectral IR and THz imaging;

- Dynamic background correction and contrast enhancement [14], applied to THz imaging; and

- Thresholding [13], applied to data obtained by all five imaging systems.

These image and signal analysis techniques are presented in this thesis as an approach to finding an integrated set of solutions addressing hardware and sensor platform limitations. The trade-offs between performance and optimality of an algorithm solution were considered, with the need for pseudo-real time analysis in most cases.

The thesis is organized as follows:

- Because the five imaging systems are often studied in diverse fields of engineering and physics, a brief background and hardware description is given at the beginning of every chapter.

- For all imaging applications the raw data was provided by collaborators who have built the hardware and were familiar with the physical non-idealities of the imaging systems that needed to be corrected by the processing.

- The lowest frequency application (EEG for epilepsy seizure detection) and the highest frequency system (IR and visible data for target detection). Both are processed by using similar techniques which is a combination of linear and nonlinear methods. Therefore, the EEG and the hyperspectral imager research is described in the appendices. The other three applications involve linear processing and comprise the main body of the thesis.

- Chapter 2 discusses the Synthetic Aperture Radar autofocusing of high resolution X-band images. In this case, we had little access to the hardware and autofocusing algorithms already existed. The work in this thesis was an addition to an existing algorithm and thus a good starting point for introducing the advantages of post-processing.

- Chapters 3 and 4 present results on the single pixel NIST passive terahertz imager. In this collaboration we had access to the hardware and several relevant quantities were measured as a starting point for the processing. For example, Chapter 3 presents measured antenna radiation pattern at $95\,\mathrm{GHz}$ and $238\,\mathrm{GHz}$ and in general gives information on the imaging system. Chapter 4 focuses on the

specific processing algorithms developed for this hardware.

- Chapter 5 extends the processing for the single pixel imager to a row-based and conical-based linear array terahertz scanners. All three chapters focus on noise reduction, feature detection, and correcting for hardware non-idealities such as varying detector response and non-uniform sampling.

- Chapter 6 presents processed images for a first generation near-field UHF and microwave scanning probe for sub-surface defect detection on CMOS chips. In this case, the resolution of the system is low as well as the SNR, filtering, upsampling, and interpolation are necessary to detect differences between two nominally identical CMOS chips.

The thesis concludes with a discussion and recommendations for future work.

Chapter 2

Autofocus for High Resolution X-Band SAR Imagery

This chapter is organized as follows. Section 2.1 gives fundamentals of Synthetic Aperture Radar. Section 2.2 presents a brief theoretical background on EV-PGA, wavelet decomposition, and wavelet shrinkage. Section 2.3 presents some examples from the experiments performed on the high resolution X-band SAR imagery, and Section 2.4 contains the final remarks and recommendations based on the results of this work.

2.1 Introduction

Airborne radars are commonly used for ground mapping, environmental monitoring, and military systems applications. Creating a high resolution image using a radar requires achieving resolution simultaneously in range and cross-range. This can be done with an electrically large antenna, which at microwave frequencies can be physically quite large and difficult to fly on an aircraft. Therefore, aperture synthesis is often used increase the larger aperture by adding the phase information of each of the radar returns with accompanying heavy signal processing. There are two main acquisition modes in synthetic aperture radar: spotlight-mode and strip-map mode. This chapter will focus mainly on spotlight-mode images which are used in areas where a larger spatial

resolution is desired. The collection geometry for spotlight mode will be shown in the next section and the mathematical definitions will follow the conventions used in [15]. The image formation details for the spotlight collection geometry are further discussed in Sec. 2.1.1.

An example of a SAR platform aircraft at Sandia National Laboratories is shown in Fig. 2.1. The aircraft carries an RF front-end for dual band at both Ka (32.6 - 37.0 GHz) and Ku (14 - 16 GHz)Ku bands. Two spatial resolutions from 1 cm to 2 cm are achieved from the dual band system. The collection range varies from 2 to 15 km and is processed into images in real-time. Sample images are shown in Fig. 2.2.

Figure 2.1: Sandia National Laboratory SAR platform aircraft carrying a complete data collection system including radar, GPS-aided IMU, fully gimballed antenna, real-time image formation processor, high capacity data storage system, and optionally a real-time automatic target recognition processor. Photograph used with permission from Sandia National Laboratory.

SAR images carry phase information that is extracted from the deconvolution of the transmitted pulse and returned signal from the scatterer. Generally during acquisition the acquired signal is processed using on-board motion correction units and adding global positioning system (GPS) information. Some of the signals can be out of focus due to uncompensated errors that are left uncorrected by the real-time processing. These uncompensated errors are produced by, e.g., relative flight trajectory deviations.

Traditional algorithms like the phase gradient (PGA) [16], and the eigenvector phase gradient autofocus (EV-PGA) [5,17] can correct for some of these uncompensated errors. Additional examples of focused images are shown in Fig. 2.2.

(a)   (b)
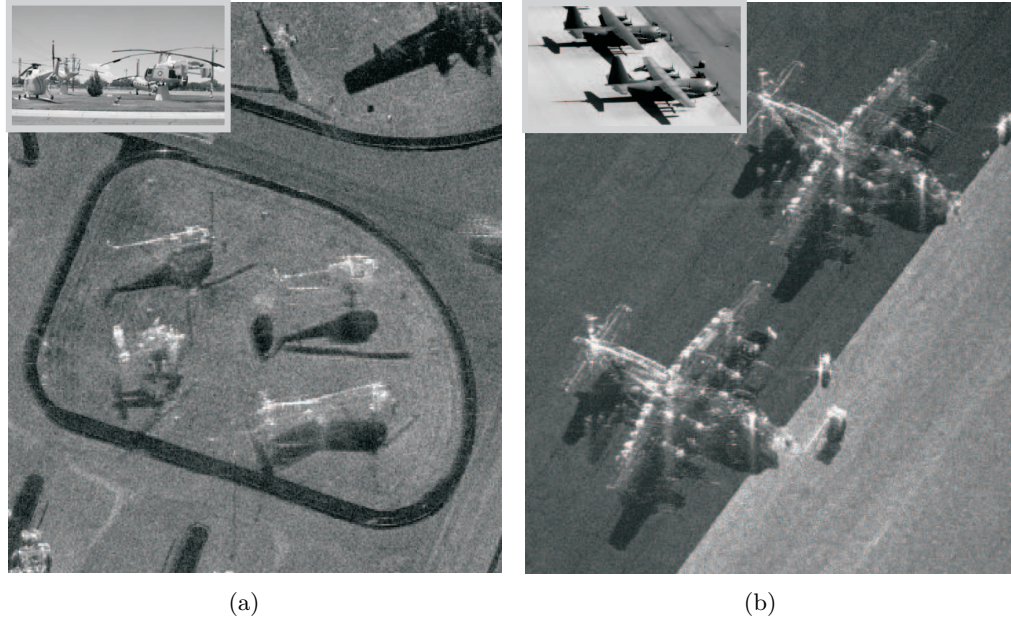
Figure 2.2: SAR 4 in resolution images obtained by Sandia National Laboratories, (a) Ka-Band static display of historic rescue helicopters on the ground, (b) Ka-Band C-130's on flight line

2.1.1 Spot-light mode SAR image

Following the geometry in Fig. 2.3, the spotlight mode can be seen as a collection of line integrals of the same reflectivity function along the range direction as pulses are transmitted at different viewing angles θ. The most relevant characteristic of the SAR spotlight mode is that the antenna beam always aims at the center of the ground patch as it moves along the flight path. The transformed coordinates $(\bar{x}, \bar{y})$ represent the cross-range and range directions in the ground plane, rotating (x, y) by the viewing angle θ. Thus, the coordinate transformation is:

$$\bar{x} = x\cos(\theta) + y\sin(\theta) \tag{2.1}$$

$$\bar{y} = -x\sin(\theta) + y\cos(\theta). \tag{2.2}$$
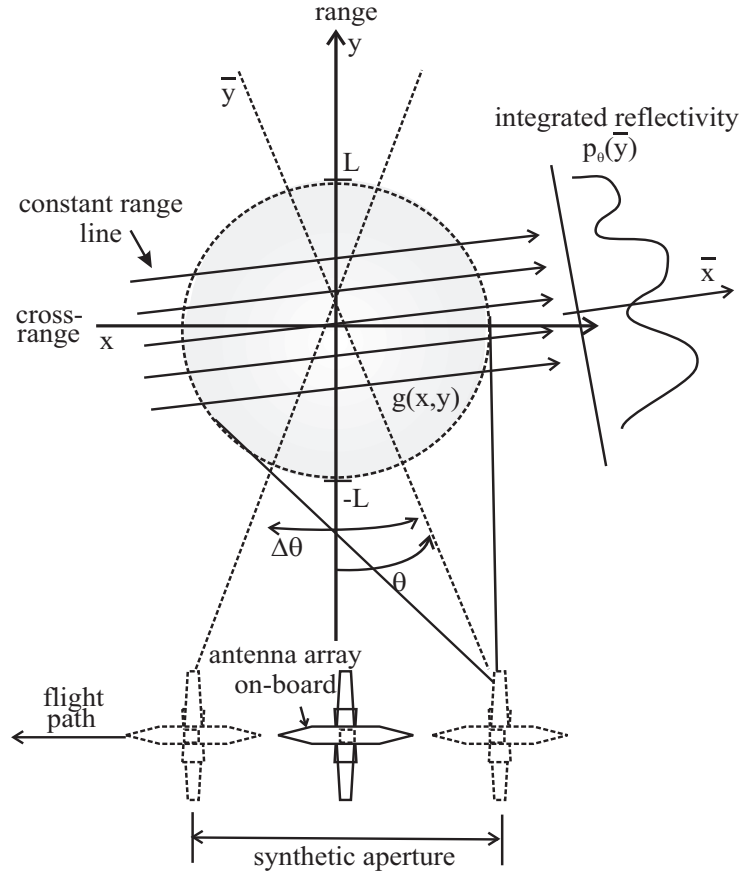
Figure 2.3: Sketch of Synthetic Aperture Radar imaging concept. The pulses are transmitted in the direction of a ground patch as the aircraft moves along x-path. The longer the flight path the higher the cross-range resolution; creating a longer physical antenna synthetically by using signal processing. The antenna is steered to continue aim at the center of the patch.

An integrated microwave reflectivity function can be now defined as $p_\theta(\bar{y})$ as a function of the scene reflectivity $g(x,y)$. The scene reflectivity $g(x,y)$ is assumed to be zero outside the circle of radius L, and the reflectivity is

$$p_\theta(\bar{y}) = \int_{-L}^{L} g(x,y)d\bar{x} \tag{2.3}$$

The synthetic aperture is constructed from the flight path of the aircraft as it transmits and receives the pulses. A collection of p_θ becomes the acquired SAR image. In SAR imaging the goal is to estimate a three dimensional radar reflectivity density function $g(x,y,z)$ obtained from for the ground patch illuminated by the antenna. Also, $g(x,y,z)$ can be described as a two-dimensional projection of the scene reflectivity func-

10

tion onto a plane, as depicted in Fig. 2.4. This figure describes the three-dimensional signal collection surface created in a SAR spotlight mode as defined in [15]. Each pulse sent by the radar receives a line segment of data from the ground in 3D Fourier space. The phase history data on the slant plane lies on a polar raster format on the coordinate axes (X', Y'). The angular orientation of the line in the phase domain is the same as the direction of the pulse transmission in the image. These samples are projected on the ground plane turning the (X', Y') coordinate system into (X, Y) following a polar-to-rectangular interpolation. This projection will allow for range spatial frequencies to be transformed the ground range spatial frequencies, leading to a ground-plane reconstructed image [15].
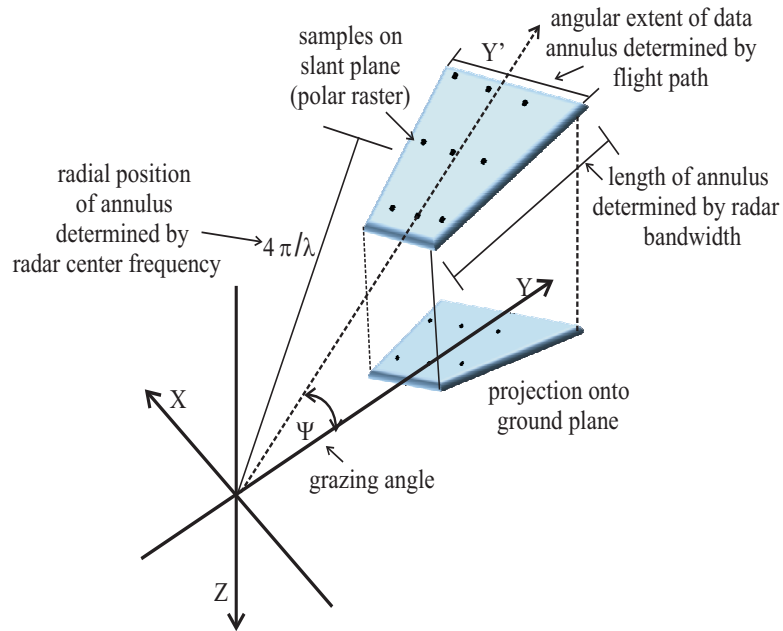
Figure 2.4: Three-dimensional signal collection surface in SAR spotlight mode as defined in [15]. Each pulse gives a line segment of data in 3D Fourier space. The angular orientation of the line in the phase-history domain is the same as the direction of the pulse transmission in the image.

In order to reconstruct the image from the phase history, a two-dimensional scene function, $g(x', y')$, can be defined as before and its 2D Fourier transform is $G(X', Y')$. The new image is produced by the inverse Fourier transform of the observed data as,

$$g(x', y') = \int_{-\infty}^{\infty} \int_{-\infty}^{\infty} G(X', Y') \exp^{j(x'X' + y'Y')} dX' dY'. \tag{2.4}$$

The above function $g(x', y')$ now becomes the 2-dimensional projected image of the collected radar returns.

2.1.2 Phase errors on SAR images

When reconstructing a SAR image it is important to be able to calculate relative uncertainties in the pulse to pulse distance. This is done normally using error correction equipment on the aircraft, but as the flight path becomes longer, for higher resolution images, there could be more drift on the flight. These uncertainties can be removed by using ultra-high-accuracy inertial sensors, but can also be corrected using auto-focus algorithms which are less costly and can correct demodulation errors independent of where the error is coming from. Several phase error correction algorithms have been studied in [5, 16–23]. Some of these techniques use fundamentals on inverse filtering, e.g., [16, 17], others are based on optimization of sharpness metrics [24, 25]. These algorithms are a type of image restoration mechanisms where the goal is to correct for unknown phase aberrations. The errors induced in the data are related to Fourier phase shifts in the imaging data and can be modeled by a constant phase plus a phase ramp. In the case of spotlight SAR collection mode, a series of pulses are sent to create a two dimensional *ribbon* [15]. Using several pulses at different instants in time can induce errors on the range compressed phase data. In order to correct for these errors, a compensating aperture phase error function is estimated. Letting a new 2D image corrupted with error be described as:

$$g_\varepsilon(k, n) \qquad = IFFT_m \left\{ \bar{g}_\varepsilon(k, m) \right\} \tag{2.5}$$

where m and k are given by the aperture and range positions, respectively, the phase error function can be estimated from inverse Fourier transforms and basic convolution theorems. Eqn. 2.5 now turns into,

$$g_\varepsilon(k,n) = IFFT_m \left\{ \exp^{j\phi(m)} \right\} \otimes g(k,n) \tag{2.6}$$

From Eqn.2.6, an estimate of the phase-error function can be found. This $\phi(m)$ will provide the correction factor to remove the defocus degradation on the 2D corrupted image data.

There are two types of errors in the image data: 1) those caused by relative aircraft motion, and 2) propagation induced errors. Autofocusing algorithms can correct for both of these cases. Several phase error correction algorithms have been developed previously to address this problem, e.g. shear averaging [22], sub-aperture autofocus [26], inverse filtering or phase gradient autofocus (PGA) [16, 17], and a modification of PGA using eigenvectors [5]. This chapter will focus on the Eigenvector Phase Gradient Autofocus developed by [5] and a modification proposed here to improve residual noise on the estimated phase error function.

2.1.3   Autofocusing X-Band SAR imagery

The image shown in Fig. 2.5 is used to demonstrate the need for autofocusing. It was obtained with an X-band SAR at Ft. Huachuca, Arizona and shows the roof of a gas station. After the EV-PGA algorithm is applied (Fig. 2.5b), there is obvious improvement in the level of focus, however, sometimes this technique can lead to a correction where the phase error estimate is noisy. This usually occurs in areas of the image where the target-to-clutter ratio is small and can be observed in Fig. 2.5b as streaks in the cross-range direction. The goal of this chapter is to obtain a higher level of focusing by introducing an additional step in the EV-PGA algorithm.

Given that the data acquisition platform is known to have a smooth motion as the radar collects the data, it is sensible to assume that the uncompensated errors in the image should be represented as a smooth version of the estimated phase function. It becomes of interest to study a technique to enhance the result of this estimator by using a denoising mechanism. We show that indeed the smoothing reduces the noise on the phase function leading to an improved focused image. The phase denoising is
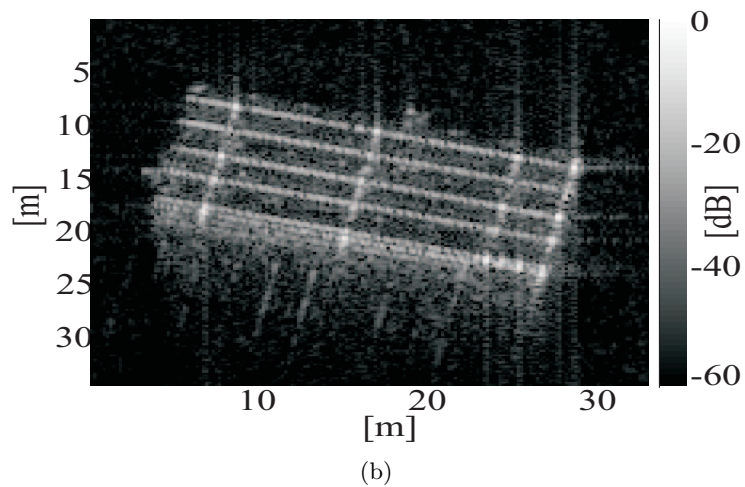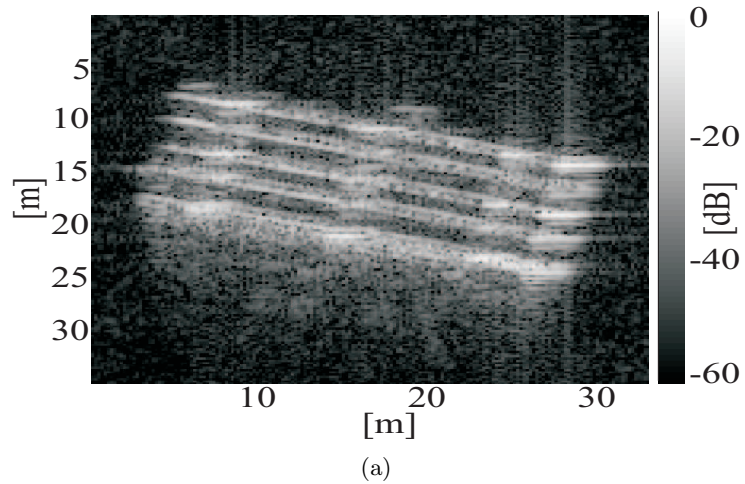
Figure 2.5: Relative airplane motion during image acquisition and uncompensated errors that remain uncorrected after processing the SAR data result in a unfocused SAR image due to uncompensated phase errors (a). Top of a Shell gas station. The EV-PGA algorithm [5] produces a focused image by correcting estimated phase error function (b). The streaks in the image are phase error estimate noise induced by the algorithm.

implemented as an additional step to EV-PGA developed in [5] and based on the wavelet shrinkage techniques and thresholding developed in [27, 28]. The wavelet shrinkage and thresholding is applied to a multi-level wavelet decomposition of the phase only eigenvector representing the phase error needed to correct the image. An illustration of the effect of specific phase noise error introduced into a actual image is shown in Fig. 2.6. This image shows a focused image of six aircrafts on a landing strip taken with the same SAR as in Fig. 2.5. A noisy quadratic phase error shown in Fig. 2.6(b) has been synthetically added to it, resulting in defocusing as shown in Fig. 2.6(c). This type

14

of defocusing is a characteristic result of uncompensated motion.

(a)

(b)

(c)
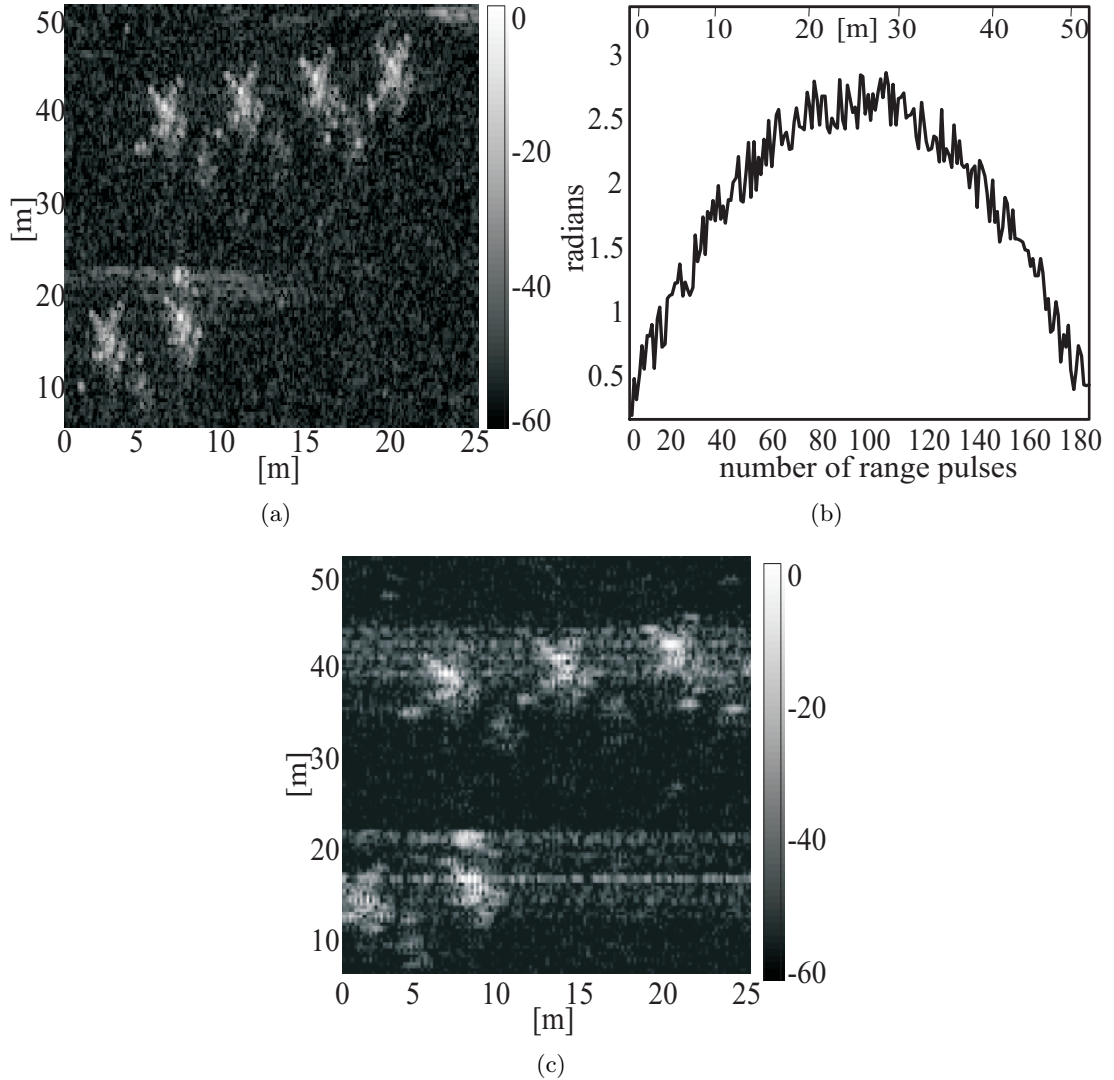
Figure 2.6: Illustration of effects of phase error (a) Focused image of 6 aircraft on landing strip. (b) Added quadratic phase error which simulates uncompensated relative motion. The vertical axis is the added phase in radians while the horizontal axis corresponds to cross-range (columns of the image) (c) Unfocused image of aircraft with quadratic phase error function and noise added to focused image obtained from EV-PGA.

2.2   Algorithm Background

The Phase Gradient Autofocus (PGA) algorithm proposed in [5] is based on a Maximum Likelihood algorithm that estimates the phase error function describing the existing arbitrary errors in a SAR image. The EV-PGA is presented as a post processing technique

for autofocusing and correcting uncompensated errors in the SAR imagery. Further details of the derivations of the EV-PGA algorithm are given in [5, 29]. The modification of EV-PGA in this work is illustrated in Fig. 2.7 as a step incorporated in the original algorithm prior to error thresholding. After step 5 of Figure 2.7, the output signal is modified as described below.
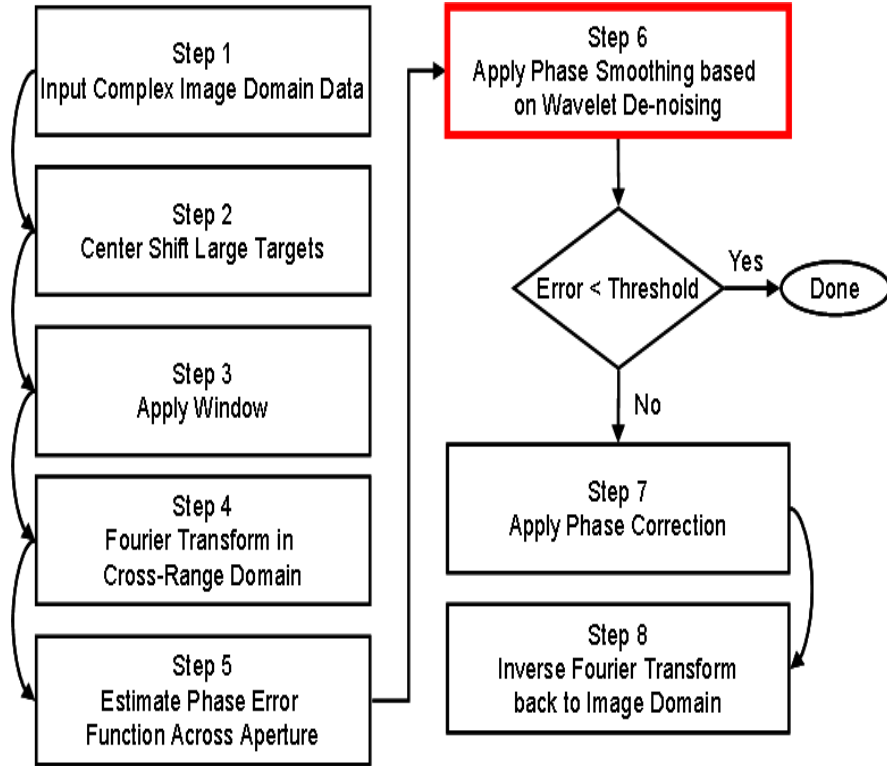
Figure 2.7: Flowgraph of the algorithm as described in [5], with a modification shown in step 6. The phase smoothing and wavelet denoising is applied before the error thresholding with the purpose of noise reduction in the already processed image.

2.2.1   Wavelet packet decomposition

The Continuous Wavelet Transform (CWT) is applied to the estimated phase signal. This gives a signal representation on a time-scale domain by decomposing a signal in a set of orthonormal basis. It is dependent on the choice of a given first wavelet, referred to as a mother wavelet, $\Psi_{s,\tau}(t)$. The CWT notation can be represented as $CWT\{s(t)\} = <s(t), \psi_{s,\tau}(t)>$, where s is the scale and τ is the displacement, and the mother wavelet is represented by:

16

$$\psi_{s,\tau}(t) = \frac{1}{\sqrt{s}}\psi\left(\frac{t-\tau}{s}\right). \qquad (2.7)$$

To create an efficient and practical algorithm, the CWT is sampled at discrete intervals. The Discrete Wavelet Transform (DWT) approximates the continuous wavelet transform by down-sampling the signal on a dyadic scale. Let the DWT for a given signal $s(t)$ be given by $\psi_{a,b} = < s(t), \psi_{a,b}(t) >$ where a,b are scaling and shift parameters. The mother wavelet now becomes,

$$\psi_{j,b}(t) = \frac{1}{\sqrt{2^j}}\psi\left(\frac{t-2^j}{2^j}\right) \qquad (2.8)$$

in which j denotes the scale, b the translation, and j,k are integers.

The discrete wavelet transform can be seen as a filter bank, as shown in Figure 2.8, $g[n]$ represents a low pass filter and $h[n]$ a high pass. The signal $s[n]$ decomposition into $d[n]$ and $a[n]$ provides what are referred to as the detail and approximation coefficients, which are later used to reconstruct the signal.

Higher order frequencies in the function can be filtered to generate a smoother estimated phase function. Therefore, the decomposition shown in Figure 2.8 is an appropriate representation since it automatically allows elimination of certain frequency components from the signal. For example, for a decomposition tree with L levels, up to 2^{L-1} decomposition coefficients can be eliminated. The more high frequency components are eliminated, the smoother the phase function. However, this will be at the expense of loosing features of the signal that can affect the quality of the focusing. The algorithm design consists of choosing the number of L levels and the particular $h[n]$ that will be eliminated in order to achieve optimal focusing. In this case focusing is defined by the 3-dB beamwidth of a point scatterer spatial pattern.

An efficient mechanism to find the optimum wavelet packet decomposition tree is described in [30]. Referring to Figure 2.8, the decision to add another decomposition level is based on the Shannon entropy, E, calculated as follows at each level:

$$E(y_{j,k}) = -\sum_{j,k}(s_{j,k})^2 \log y_{j,k}^2 \qquad (2.9)$$

17
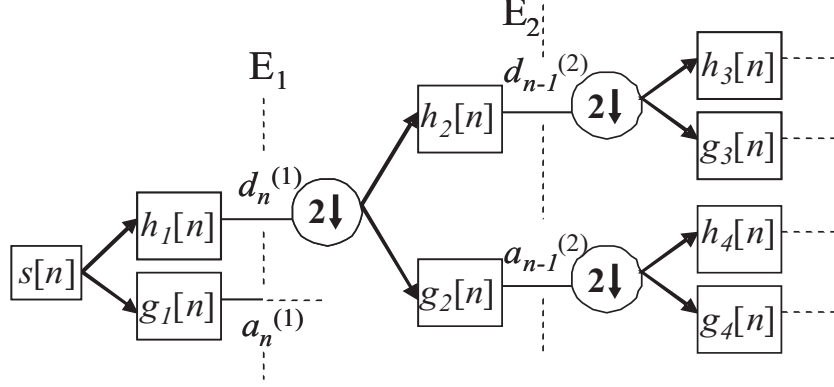
Figure 2.8: Wavelet packet decomposition tree. The signal $s[n]$ is decomposed at L-levels. Each stage, L contains a high pass and low pass orthogonal filters given by $h_i[n]$ and $g_i[n]$. These filters are different at each decomposition level. A down-sampling is used at each level to increase computation efficiency.

where $s[n]$ contains high and low frequency components.

An example of a decomposition using wavelet packets is shown in Figure 2.9 where the quadratic phase error function obtained from PGA is analyzed with a 3rd order Coiflet mother wavelet. The choice of Coiflet wavelet was dictated by its compact support and N number of vanishing moments that are directly related to the desired smoothness of the function for which the phase error estimate is being analyzed.

2.2.2 Thresholding and denoising

A thresholding technique was used to eliminate the high frequency components per level of decomposition of $s[n]$. The methodology used in this work is based on wavelet shrinkage and soft thresholding described by [27]. Let the signal of interest be $s(t) = y$. The wavelet transform and coefficients of y can be represented as $w = Wy$. The reconstruction of y is described in terms of a sum of wavelet basis given by

$$y_i = \sum_{j,k} w_{j,k} W_{j,k}(i); j = 0, ..., J - 1; k = 0, ..., 2^{j-1};$$ (2.10)

where J represents the maximum possible level of decomposition dependent on the length of the signal, N. If $w_{j,k}$ is allowed to be the set of wavelet coefficients for the PGA estimated phase error function, then the representation of the wavelet decomposi-
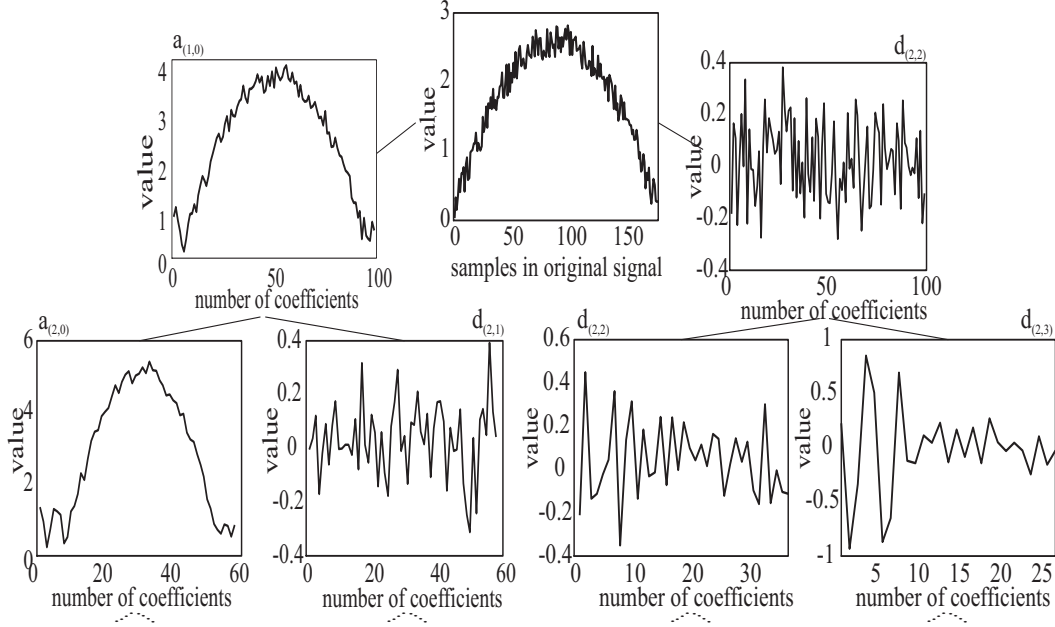
Figure 2.9: Specific example of decomposition algorithm for Fig. 2.8. The initial signal $s[n]$ is the sampled phase error function that comes from the processed SAR data. In the first step of decomposition the right hand branch carries the high frequency components of the signal. The left hand branch contains the main signal information. The goal is to optimally choose a combination of the coefficients to reconstruct the denoised signal.

tion of y can given by $y_{j,k} = w_{j,k} + \sigma z_{j,k}$ where $z_{j,k}$ is iid noise $\mathbb{N}(0,1)$ (white noise). At this time the goal becomes the thresholding of $y_{j,k}$ in order to denoise the estimate of the phase error obtained from EV-PGA. The threshold used in this work is based on a soft threshold by minimizing the quadratic loss function found on Stein's Unbiased Risk Estimator (SURE). Each of the wavelet coefficients per scale in the wavelet decomposition are taken to be a multivariate normal estimation problem and the threshold, t^* is given by $t^* = \arg\min_{0 \le t \le \sqrt{2logd}} \text{SURE}(t; y)$ where y is described above. The reader is referred to [27] for further proofs and derivations of the thresholding methodology.

2.3   Numerical Experiments

The analysis for this work was performed on a high resolution (0.3 m) X-band SAR image dataset of size $N = M = 6554$. The imagery was collected from Ft. Huachuca in Sierra Vista, Arizona. For all of the results shown in this section, the EV-PGA analysis

(a)   (b)   (c)
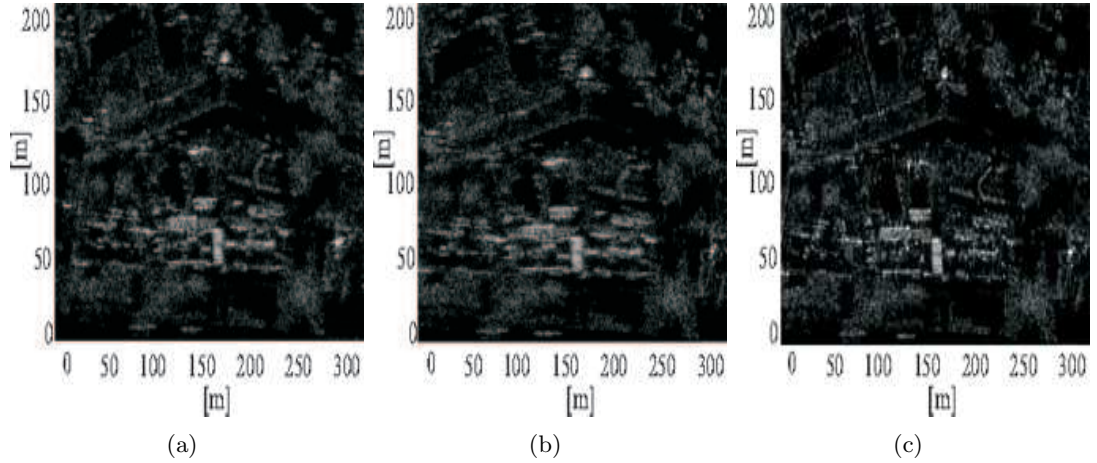
Figure 2.10: Selected region of Sierra Vista image to show autofocusing results using eigenvector phase gradient autofocus and EV-PGA with wavelet smoothing: (a) original unfocused image (b) autofocusing using PGA algorithm, (c)autofocusing PGA with wavelet smoothing. The gray scale is normalized power in dB.
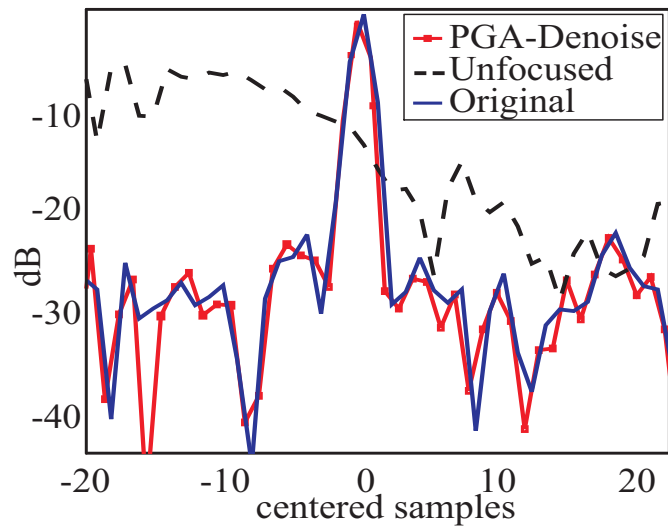
Figure 2.11: Comparison of focusing algorithm with and without the addition of denoising. The dashed line shows the unfocused scatterer that was degraded by adding an arbitrary phase error function to the image, the original sample scatterer is shown in solid line with no symbols, and the auto-focused and denoised sample scatterer (solid line).

used of 512 samples from the image and computed the sample covariance matrix using 30 contiguous range pulses for every block of the original image. The following experiments show a comparison of the autofocusing using PGA without using a denoising mechanism
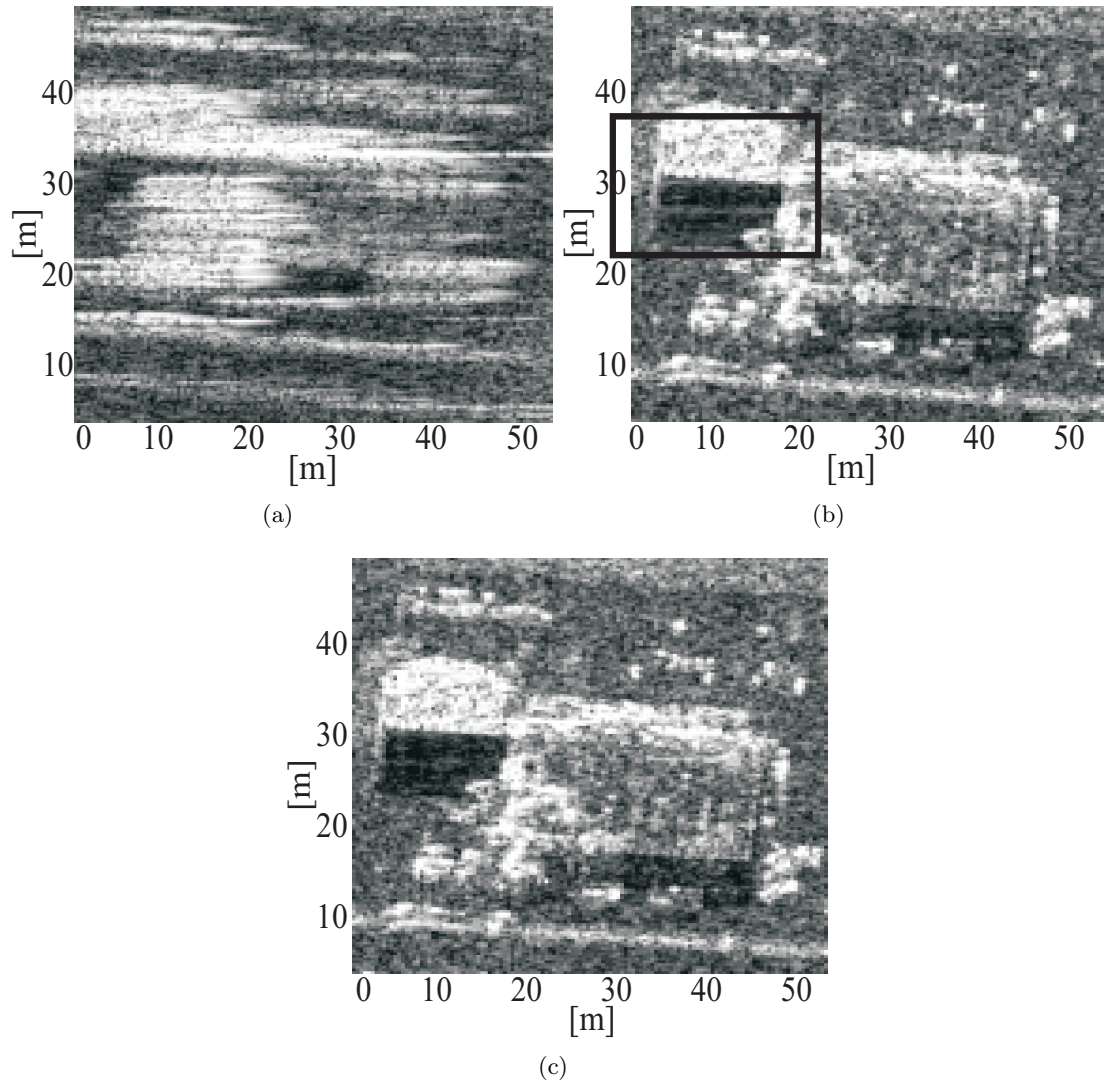
Figure 2.12: Effects of autofocusing and denoising on the removal of streaks in the image caused by EV-PGA (a)Unfocused image with induced phase error, (b) Autofocusing using PGA algorithm, (c)Autofocusing using PGA and denoising.

applied to the estimate of the phase error function and results of PGA with denoising. After 8 iterations, the results of the EV-PGA algorithm with and without denoising are shown.

A common metric used to measure the quality of the autofocusing is to use the 3-dB width of a point-like scatterer spatial impulse response. The spatial response of a focused scatterer has a narrower main lobe and a significant reduction of the sidelobes when compared to an unfocused scatterer response. Figure 2.13 shows a particular part of the image from Figure 2.10 which contains a point-like scatterer. It shows different levels of focusing corresponding to the two different algorithms. The algorithm presented in this chapter shows an improved autofocusing effect, although the sidelobes are still present. However, it is important to note that the addition of the denoising step to EV-PGA improves the images quality but does not degrade the focus. Figure 2.13 shows a horizontal cross section of the point scatterer response for the unfocused, and the focusing algorithm with an ideal point-like scatterer of the same size.

Another benefit of using denoising is the reduction of induced streaking in the image caused by the autofocusing mechanism. The denoising mechanism improves the quality of the image and does not degrade the focusing, as it is shown on a 3-dB beamwidths plots in Fig. 2.13 and 2.11.

2.4   Final Remarks

This work presented an application of wavelet coefficient thresholding for denoising the phase error estimates obtained from EV-PGA in SAR imagery. As shown in the experiments, the use of a wavelet denoising mechanism achieves improved focusing on the image set. Figure 2.13 and 2.11 show a comparison of the 3-dB widths for an ideal and a focused scatterer from a focused image. When testing the algorithms several factors were varied: (1) number of eigenvectors, (2) block image size, (3) number of iterations, (4) overlapping of eigenvectors. The latter was shown not to have an effect.

Intuitively, it makes sense that larger image block should give a better estimation
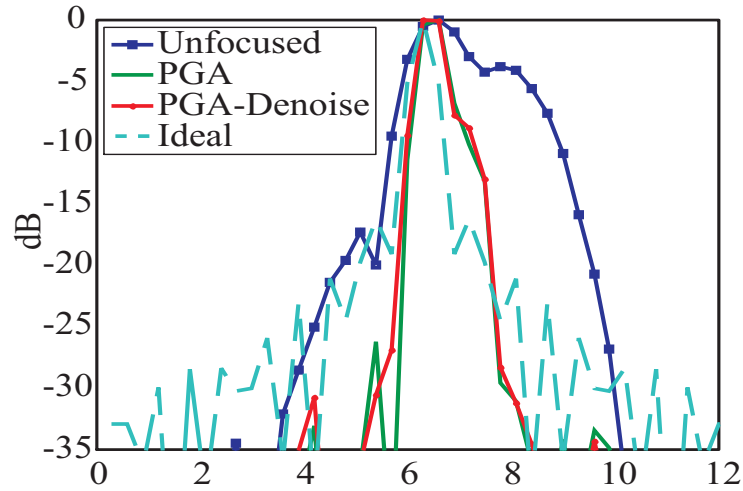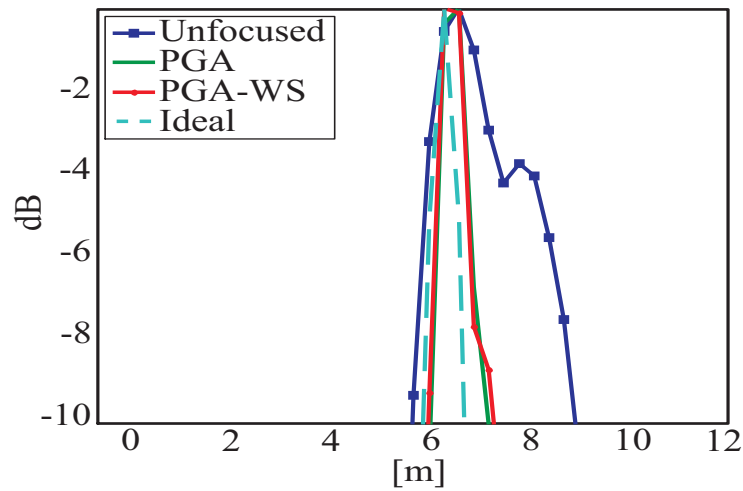
Figure 2.13: Impulse response of a selected bright scatterer from the processed SAR image in Fig 2.12. Comparison of autofocusing methods: (solid line-squares) Unfocused bright scatterer from image, (solid) Autofocused using PGA, (solid line-circles) Autofocused using PGA with Wavelet Denoising (PGA-Denoise), (dashed) Ideal scatterer for a known spatial resolution.

of the eigenvectors, and this was indeed confirmed by simulation. This is especially true for images containing a high content of clutter and an absence of distinctive bright scatterers. The size increase in the image block provides the estimation process with more information to generate the estimate of the phase error function. As described in [5], the EV-PGA achieves the Cramér-Rao lower bound for variance for size images for large N. Taking into consideration the aforementioned observations, this work proposes

an increase in the block size of the image from $N = 512$ to $N = 1024$ for high resolution imagery in which there exists a low target-to-clutter ratio. There was an improvement observed when the number of iterations is increased. As the resolution of the image increased from $1\,\mathrm{m}$ to $0.3\,\mathrm{m}$, it was observed that the convergence of EV-PGA algorithm did not reach an acceptable set value of variance of the estimator unless the number of iterations was increased for images with small target-to-clutter ratio.

It should be noted that there exists a tradeoff between the amount of acceptable variance for the convergence of PGA and the number of iterations. If a larger variance is set, for example from $5°$ to $20°$, to increase the wideband performance, then the algorithm should be allowed larger block image sizes even if the number of iterations remains set to a lower value ranging from 8-10. However, it the computational cost of EV-PGA is not a priority concern, for higher resolution image, the number of iterations should increase $i > 10$ and use a suggested block size of $N = 1024$. The number of eigenvectors to use for the approximation of the phase error function and the overlapping of one to two pulses for the covariance estimation did not seem to affect the results of the PGA autofocusing.

In summary, in this chapter, physical parameters of an airborne radar (velocity, phase, and range) are described with a two-dimensional function $g(x, y)$ representing the phase of the reflected radar return. Signal processing methods were then applied in order to reduce effects of the varying velocity vector. This allows for higher-quality images obtained at X-band, a wavelength of $3\,\mathrm{cm}$, with a spatial resolution of less than $1\,\mathrm{m}$. The next chapter discussed higher spatial resolution ($<1\,\mathrm{cm}$) using higher frequency ($>100\,\mathrm{GHz}$) imaging by defining an amplitude instead of a phase distribution function of (x,y). The algorithm presented in this chapter as a modification to EV-PGA was implemented and used in the Massachusetts Institute of Technology-Lincoln Laboratory LiMIT SAR Testbed.

Chapter 3

Single pixel millimeter wave imaging system: antenna properties

For a given antenna size, a higher frequency will give higher spatial resolution. For applications such as concealed weapon detection, a resolution of the order of less than $1\,\mathrm{cm}$ is crucial, implying the use of millimeter wave frequencies. The millimeter and sub-millimeter wave ranges are generally defined as those frequencies between $100\,\mathrm{GHz}$ to $10\,\mathrm{THz}$, with wavelengths in the range of $3\,\mathrm{mm}$ to $1\,\mu\mathrm{m}$. Material properties are often very different in the terahertz frequency region, compared to the lower (microwave) and higher (optical) frequencies. Measurements for common clothing materials at terahertz, for example, are shown in [31].

For imaging applications at microwave and terahertz frequencies, two different modalities can be used: 1) active and 2) passive imaging. There have been numerous millimeter wave imaging systems developed throughout the years, both in passive and active modalities. In active imaging systems the signal is dominated by reflections of the signal emitted by a source. In passive systems, the received signal is the frequency dependent

black-body emission. The black-body emission is described by Planck's law,

$$W_\lambda(\lambda, T) = \left(\frac{2\pi hc^2}{\lambda^2}\right) \left(\frac{1}{\exp^{hc/\lambda kT} - 1}\right) \tag{3.1}$$

where c is the speed of light, λ is wavelength, T is absolute temperature in Kelvin, h is Planck's constant of $6.625 \times 10^{-34} \, Ws^2$. The Boltzmann's constant is given by $k = 1.3805 \times 10^{-23} \, W \, s \, K^{-1}$ and W_λ is radiation emitted by the black-body source per surface area at a given λ. In a passive imaging system operating at millimeter wavelengths, the power due to black-body radiation is measured by the imager hardware and can be expressed in terms of temperature changes. These changes in temperatures are converted and calibrated into an image displaying each pixel from the acquired scene as a measure of radiometric temperatures. Each pixel contains the radiometric temperature information given by,

$$T_{rad} = \epsilon \, T_{physical} + (1 - \epsilon) \, T_{background}, \tag{3.2}$$

where T_{rad}, $T_{physical}$, $T_{background}$ are the radiometric, physical and background temperatures respectively, and ϵ is the emissivity of the object.

In [32], a passive single-channel millimeter wave imager at $94 \, \text{GHz}$ with a $1.2 \, \text{m}$ Cassegrain antenna and eight radiometer is presented. This system had the limitation of not operating in real time. In [33], the authors presented a near real-time application of a passive millimeter wave imager. The imager had diffraction limited performance at $25 \, \text{Hz}$ refresh rate using 32 direct detection receivers. The design of this imager is based on a Schmidt camera design without the use of a corrector plate, expected to be free of coma and astigmatism aberrations. An illustration for the ray trace and scanner of the system is shown in [33]. Another variation to the imaging system can be done by changing the scanning mechanism. Some systems use row-based raster scanning while others make use of conical scanners to cover larger areas at faster sampling rates. In [34] the authors use a $35 \, \text{GHz}$ imager with a $1.6 \, \text{m}$ aperture based on a folded conical scanner. An example of an image acquired by this system is shown in Fig. 3.1. The pseudo-image plane results on a racetrack field-of-view due to the sampling nature of

the conical scanner.

<center>(a)   (b)</center>
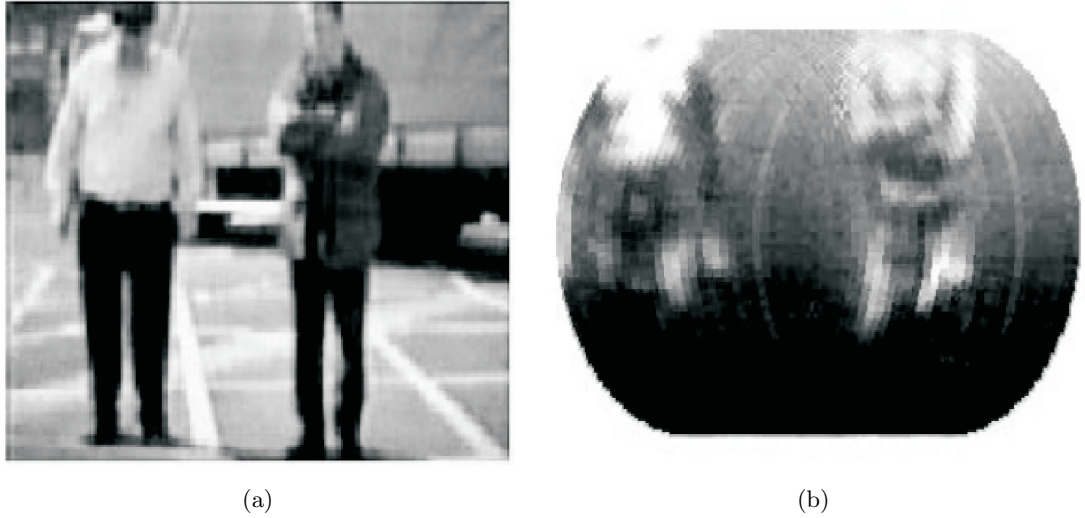
Figure 3.1: Image acquired by folded conical scan imager at $35\,\mathrm{GHz}$ with a $1.6\,\mathrm{m}$ aperture. The imager has a field of view of $20° \times 10°$ covering an adult at $4\,\mathrm{m}$ [33]. (a) Optical image of outdoor scene, (b) Image sampled with conical scanner at $35\,\mathrm{GHz}$ at $4\,\mathrm{m}$ standoff distance [33].

An example of an imaging system using millimeter wave technology for concealed weapon detection is described in [35] where the system is derived from microwave holography techniques using phase and amplitude information recorded over a two-dimensional aperture to reconstruct a focused image target. In [33] another imaging system is shown operating at $25\,\mathrm{Hz}$ frame update rate using 32 direct rate receivers from 28-33 GHz. In the same year, in [36], an antenna coupled thin film micro-bolometer designed for millimeter wave imaging arrays was presented, hence removing the coherent detection problem raised by previous architectures of active millimeter wave systems.

The passive imaging system for millimeter and sub-millimeter wavelengths shown in this thesis was developed by Dr.Erich Grossman's group at NIST in collaboration with UC-Boulder. The antenna used in the receiver is fabricated on a Si chip and a Nb micro-bolometer is placed in its feed. The designed bandwidth is around 0.2 THz achieved by using an ultra-wideband equiangular spiral antenna. Other relevant performance parameters have been thoroughly discussed elsewhere [37].

As with many imaging systems and object recognition applications there exists a

<center>27</center>

need for post-processing raw data provided by the imager to improve the quality of the measured scene. In this thesis, the following hardware parameters are taken into account in the image processing:

(1) broadband antenna patterns and coupling to the Gaussian beam of the receiver (Chapter 3);

(2) geometry of raster based scanning and radiometric temperature calibration (Chapter 4)

(3) detector non-uniformities in an eight element linear array (Chapter 5)

(4) oversampling due to conical scanning of the linear array (Chapter 5)

In this chapter, first a general description of the millimeter wave imaging system hardware used to collect the broadband images is presented, along with a brief description of the measurement setup used in the acquisition of radiation patterns for the broadband antennas and estimation of coupling to a fundamental mode Gaussian beam.

3.1   Prior work on passive imagers

For the images discussed here, simple direct detection with bolometric detectors is used, as illustrated in 3.2.

A bolometer changes resistance based on incident microwave power and this resistance change is measured by a bridge. Microbolometers much smaller than a wavelength were introduced by [38], and by reducing the size of the detector the response time and sensitivity increases. [39–41].In order to increase the capture area of such a small device, it is placed at a feed point of an antenna.

At millimeter waves the available black-body radiation power is in the order of nW and longer integration times or broadband antennas are usually required [42]. In the approach taken here, broadband spiral antennas with integrated micro-bolometer (detectors) are used in order to capture as much power as possible. Traditionally, passive
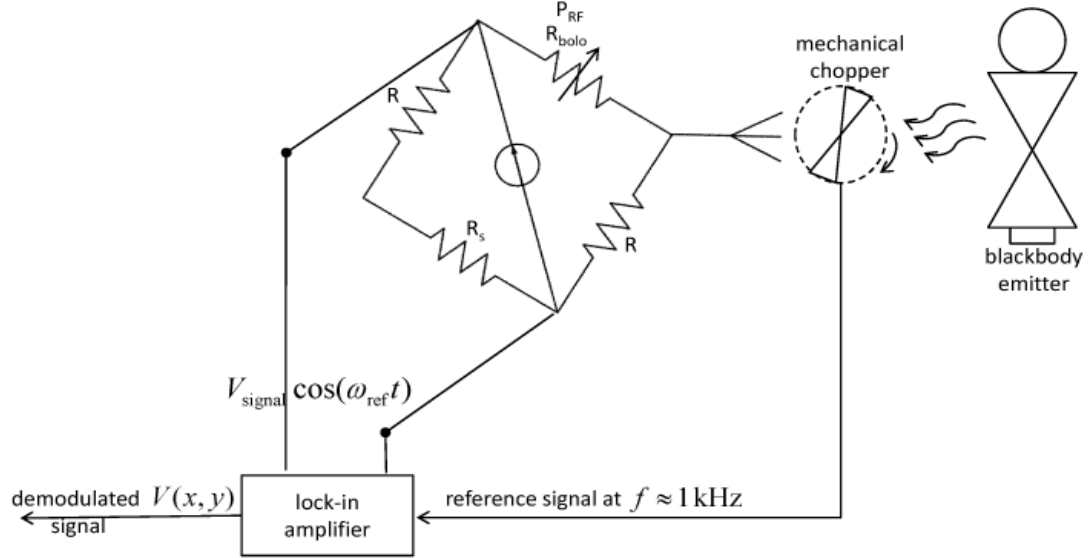
Figure 3.2: Basic passive millimeter wave imaging concept measuring the black-body radiation with an antenna coupled micro-bolometer at the receiver. The input signal is chopped mechanically at around 1 kHz and measured at the output of a lock-in amplifier. A scanning mirror (not shown) moves in the horizontal and vertical direction. Each measured incident power at position (x,y) is recorded onto a 2D array index position which is then calibrated to convert into a radiometric temperature image.

millimeter wave imaging use heterodyne receiver arrays. However, these present scalability limitations to large arrays because of higher costs. The broadband characteristics of spiral antennas have shown to maintain good coupling up to 30 THz [2].

Fig. 3.2 shows a block diagram of the antenna-coupled micro-bolometer operation used to acquire the images shown in Chapters 4 and 5. The input signal is chopped mechanically at around 1 kHz and measured at the output of a lock-in amplifier. A scanning mirror moves in the horizontal and vertical direction. The measured incident power at position (x,y) is recorded onto a 2D array index position which is then calibrated to convert to a radiometric temperature image. An example of a calibrated image acquired by this passive millimeter wave imager integrated over a band of 0.1 to 1.2 THz is shown in Fig. 3.3 [43].
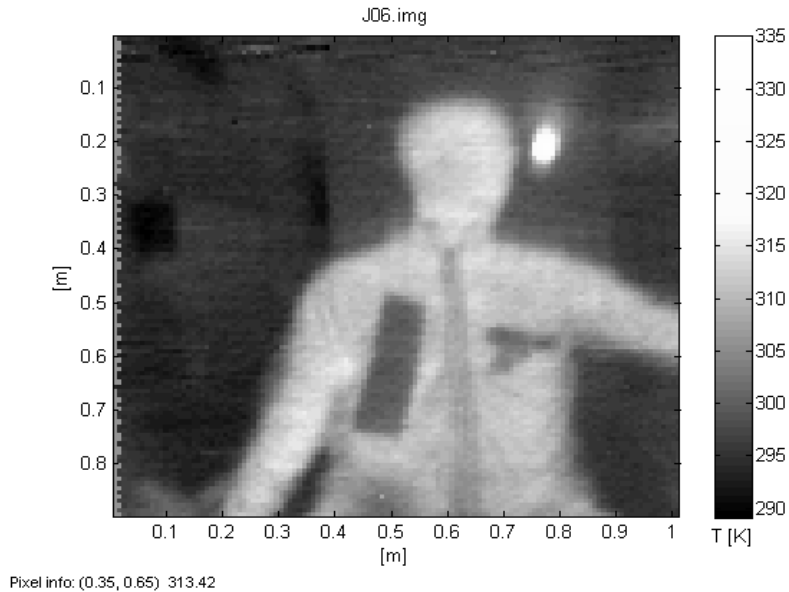
Figure 3.3: Temperature (Kelvin) calibrated image of individual at 1 m standoff distance concealing a metallic gun (right) and anechoic absorber (left) under a rain jacket. The image was acquired using broadband integration with a single pixel (detector), raster scanned.

3.2 Equiangular Spiral Antenna

Equiangular spiral antennas are categorized as frequency independent broadband antennas with near constant impedance and have been used extensively for many applications. The frequency limits of the equiangular spiral antenna are given by the outer and inner radii dimensions. The outer radius of $380\,\mu$m determines the lowest frequency limit of the antenna. The inner distance at the feed point determines the highest designed operating frequency. In this case, a Nb bridge-bolometer with dimensions of $20\,\text{nm} \times 1\,\mu\text{m} \times 24\,\mu$m with a high-frequency cutoff of $f_c = 1.8\,\text{THz}$ is used. An outline of a two arm equiangular spiral antenna is shown in Figure 3.4. This antenna is circularly polarized at higher frequencies, but at lower ones it behaves similarly to a linearly polarized dipole. A mathematical explanation for the shape of an equiangular plane spiral curve is given in [44, 45].

A scanning electron microscope (SEM) micrograph of the antenna coupled microbolometer detector used in this work is shown in Figure 3.4 [37]. The spiral antenna is
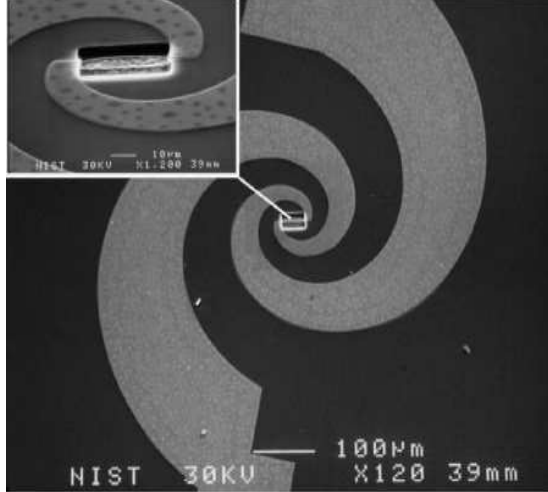
Figure 3.4: SEM micrograph of Nb bridge and Al/Nb spiral antenna. Obtained from [37] © IEEE. The antenna used as a receiver integrated on a Si chip with a microbolometer on its feed (inset). The designed bandwidth is around 0.2 THz. It has been quoted in previous publications [37] to provide noise equivalent temperature difference (NETD) of 125 mK, electrical noise equivalent power (NEP) of 26 fW/$\sqrt{Hz}$ and optical NEP of 0.4 pW/$\sqrt{Hz}$

patterned from an Al/Nb bilayer using electron-beam lithography, and the Nb micro-bolometer air bridge is formed by selective etching. The micro-bolometer resistance is matched to the input impedance of the antenna, which is $Z \approx 75\Omega$ [46]. The antenna is fabricated on a 5 mm square Si chip as shown in the diagram of Fig. 3.5, and a hyper-hemispherical substrate lens is used to couple the radiation. A detailed characterization of the detector responsivity is shown in [47] but for most of the measurements shown here the responsivity was 265 [V/W/mA].

3.2.1 Coupling of an antenna to a Gaussian beam

In the imaging system described in [47], the unpolarized plane waves produced by the scene are collected by a scanning curved mirror which produces a Gaussian beam. The antenna and micro-bolometer collect power from this Gaussian beam and therefore the interaction of the antenna with the Gaussian beam is of interest, since it will define the pixel of the image. Quasi-optical systems that are designed using Gaussian beams achieve a balance between nearly lossless propagation and processing of an RF signal
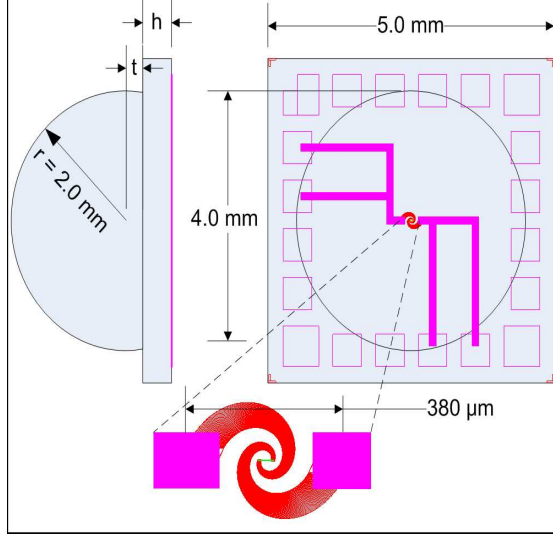
Figure 3.5: `Si` square chip with ACMB extension length of the hyper-hemisphere, $t = 0.33 \, \text{mm}$. Thickness of the Si substrate $h = 0.5 \, \text{mm}$ [48].

[49]. Coupling to the fundamental mode Gaussian beam allows for size reduction of the quasi-optical components in the imaging system.

The electric field in a propagating Gaussian beam is given in [50] as,

$$E(r,z) = \left(\frac{2}{\pi * w^2}\right)^{0.5} \exp\left(\frac{-r^2}{w^2} - jkz - \frac{j\pi\, r^2}{\lambda\, R} + j\phi_0\right) \tag{3.3a}$$

$$R = z + \frac{1}{z}\left(\frac{\pi\, w_0^2}{\lambda}\right)^2 \tag{3.3b}$$

$$w = w_0\left(1 + (\frac{\lambda\, z}{\pi\, w_0^2})^2\right) \tag{3.3c}$$

Equations (3.3b) and (3.3c) describe the radius of curvature and the beam waist radius of the Gaussian beam, respectively, as a function of position along the axis of propagation z. The Gaussian beam propagation along z is shown in Fig. 3.6. To find the coupling to a Gaussian beam of the spiral antenna, Eqn. 3.3a can be simplified and assumed to come from a radiating square aperture with constant phase as it propagates. In order to estimate the coupling, the electric field given in Eqn. 3.3a is fitted to an ideal Gaussian distribution estimated using the measured radiation pattern of the spiral antenna. The coupling to the Gaussian beam, or *Gaussicity* percentage, is then given by the estimated zero-lag cross-correlation between the measured electric field and its Gaussian fit.
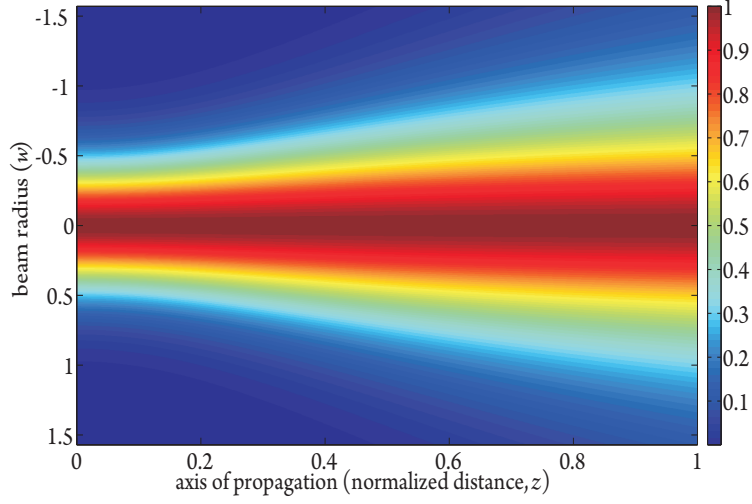
Figure 3.6: Normalized electric field intensity simulating a Gaussian beam propagation as a function of distance, z. The beam radius is wider as it moves away from the beam waist at $z = 0$. Both are normalized to the waist.

The optimal fit is found by minimizing the sum square errors (SSE) between a theoretical Gaussian beam and the measured data. An example of the optimally achieved 2D fit is shown in Figure 3.2.1. The optimum fit, for this case, was found by searching a space of $\mu = \{-5, 5\}$ and $\sigma = \{\delta, 15\}$. The parameter μ represents the position of the beam maximum in azimuth and elevation, and σ represents the beam waist at $(1/e)$. The computation of Gaussicity by means of the overlap integral can be described and approximated in terms of estimation theory. Specifically, the problem of estimating a cross-covariance matrix at *zero lag*, τ, for two random variables $\mathbf{X}, \mathbf{Y}$. The multivariate Gaussian probability density function is given by,

$$f(\mathbf{X}) = \frac{1}{2\pi^{d/2}|\Sigma|^{1/2}} \exp\left(-\frac{1}{2}(\mathbf{X} - \mu)^T \Sigma^{-1}(\mathbf{X} - \mu)\right) \qquad (3.4)$$

where $\mathbf{X} = (x_1, x_2, ...x_d)$, the expected value is μ, and Σ is the covariance matrix of $\mathbf{X}$ estimated from $E[(\mathbf{X} - \mu_x)(\mathbf{X} - \mu_x)^T]$. The covariance matrix is defined as

$$\mathbf{\Sigma} = \int_{-\infty}^{\infty} (\mathbf{X} - \mu_x)(\mathbf{X} - \mu_x)^T f(\mathbf{X}) d\mathbf{x}. \qquad (3.5)$$

For the case of having two random variables $\mathbf{X}, \mathbf{Y}$, the estimation of Σ becomes

$$\mathbf{\Sigma_{xy}} = \int_{-\infty}^{\infty} (\mathbf{X} - \mu_x)(\mathbf{Y} - \mu_Y)^T f_{xy}(\mathbf{X}, \mathbf{Y}) d\mathbf{x} \qquad (3.6a)$$

$$R_{xy} = \frac{\mathbf{\Sigma}_{xy}}{\sqrt{\mathbf{\Sigma}_{xx}\mathbf{\Sigma}_{yy}}} \qquad (3.6b)$$

where $f_{xy}(\mathbf{X}, \mathbf{Y})$ now represents the joint probability density function between $\mathbf{X}$ and $\mathbf{Y}$. In this case, $\mathbf{X}$ is given by the measured electric field and $\mathbf{Y}$ is the Gaussian fit to the E-field. Finally, by normalizing Σ_{xy} with respect to Σ_{xx} and Σ_{yy} results in a cross-correlation matrix, R_{xy}, in Eqn. 3.6b. Selecting the zero-lag correlation in 3.6b provides an estimate of the maximum similarity between the measured and fitted electric fields. For this particular Gaussian fit case a minimum was reached at $(\mu, \sigma) = (-1.70, 5.9)$. The Gaussicity values obtained using the zero-lag correlation were $G = 0.936$.
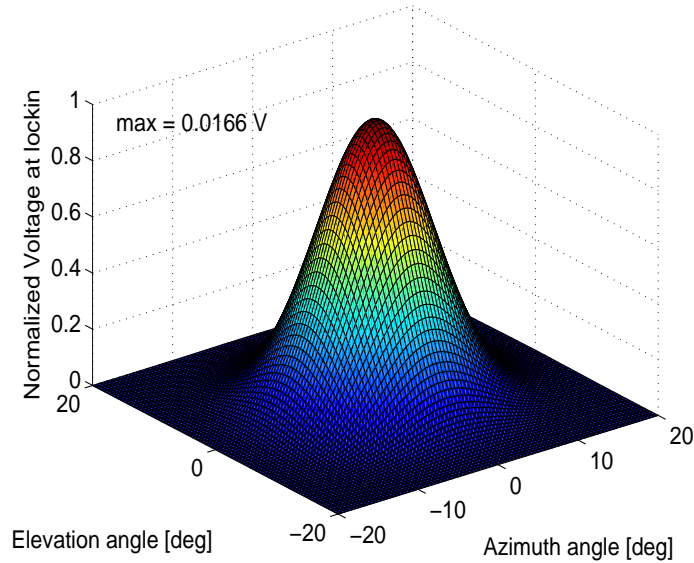
Figure 3.7: Optimum Gaussian fit to a measured electric field of spiral antenna at 95 GHz.

For ideal coupling the Gaussicity is unity and implies that the pixel size is given by $1/e$ point in the Gaussian profile, which is one standard deviation. For a Gaussicity smaller than one, the pixel is distorted. In subsequent image processing, this hardware limitation can be taken into account by different windowing.

3.3 Measured Radiation Patterns

Different radiation pattern measurements were taken to characterize the spiral antenna at 95 GHz and 238 GHz. A block diagram of the measurement setup used is shown in Fig. 3.8. In some cases a lens was used to focus the beam to the detector($f = 14.4$ cm and $f = 21$ cm). The spiral antenna measured is centered on a 5 mm square chip and placed on the back of a substrate lens of 2 mm radius. The lens and antenna are rotated by a the stepper motor controlled through a LabView Virtual Instrument. Depending on the frequency of the measurements two sources were used: a signal generator (HP 83624B) for W-band measurements and a 120 GHz Gunn diode followed by a doubler. In each case a standard gain horn is coupled to a quasi-optical setup onto a detector. The bolometer is current biased in an attempt to maximize the signal-to-noise ratio, and the signal out of the bolometer is amplified and then detected with a lock-in amplifier.

For the measurements at 95 GHz, the source was amplitude modulated at 1.1 kHz and the bolometer biased at 200 μA. At 238 GHz a Gunn oscillator was used followed by a frequency doubler. The beam was mechanically chopped at 80 Hz and bolometer biased at 550 μA. The Gaussicity for azimuth and elevation were 94% and 98% respectively. The 3-dB and 10-dB beamwidths for azimuth and elevation are presented in Table 3.3. We can observe from Table 3.3 that the beam tends to be narrower in elevation than in azimuth by about 10°. It should be noted that 95 GHz is well below the designed system operating frequency range from 0.2 GHz to 1.8 THz, and therefore we do not expect the pattern to be much different than a dipole at the lower frequencies.
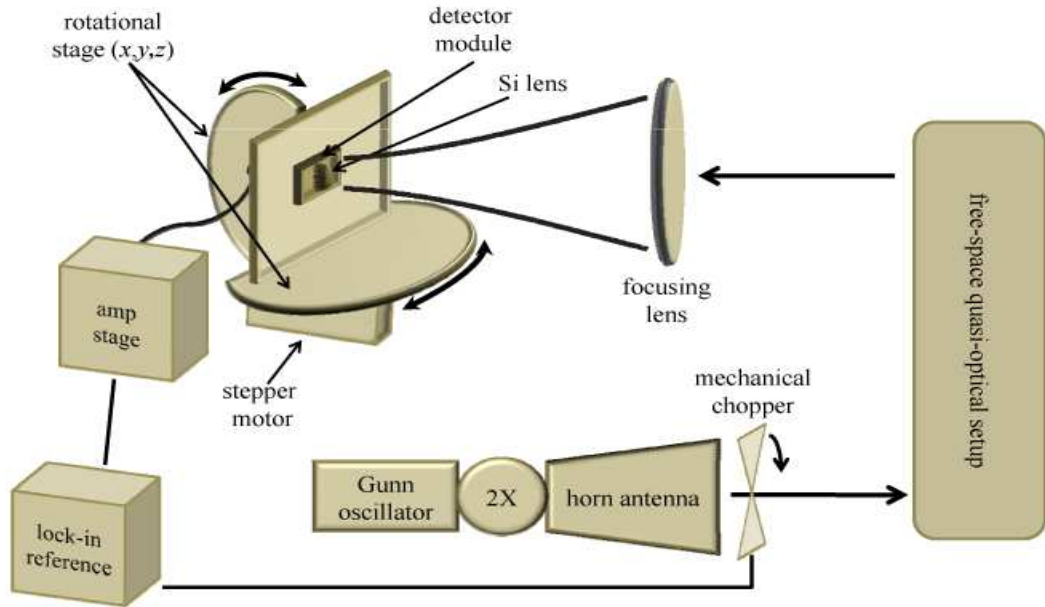
(a)

Figure 3.8: Measurement setup for radiation patterns of spiral antenna at 95 and 238 GHz. (a) Block diagram of setup showing the Gunn oscillator followed by a frequency doubler to produce 238 GHz. The beam passes through a set of guiding optics and polarizers until reaching a focusing element (lens) with $f = 21$ cm. The rotational stage is moved with a stepper motor that translates the platform holding the detector module on horizontal and vertical direction for $\pm$ 55 degrees on both axes; creating a 2D pattern measurement.

Table 3.1: Summary of measured beamwidths. Polarization and cut are referenced to the incident linearly-polarized field; co- and cross-polarization. Co- and cross-polarized measurements are defined here as those in which the incident linearly-polarized field is parallel with and perpendicular to the bolometer axis (and DC bias traces), respectively

Frequency	95 GHz		238 GHz	
Polarization	Cross	Co	Cross	Co
-3 dB E-plane	24.7	23.7	21.1	17.5
-10 dB E-plane	65.4	85.7	38.2	29.7
-3 dB H-plane	23.0	29.8	18.3	16.6
-10 dB H-plane	77.4	54.3	32.3	26.7
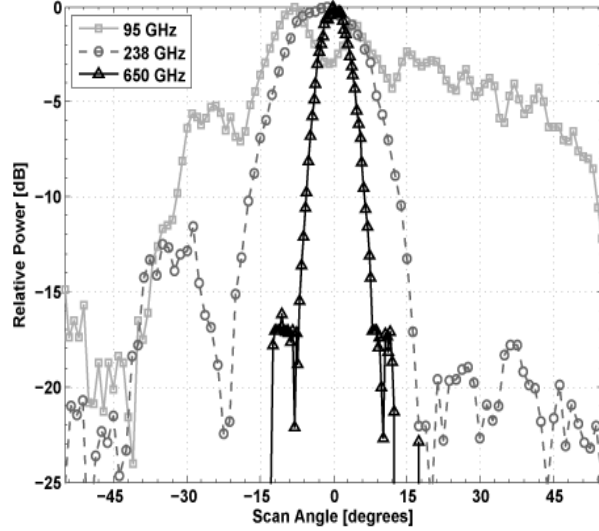
Figure 3.9: One-dimensional electric field cuts at 238 GHz and 95 GHz. A cut along 638 GHz is also shown for comparison, details in [48]. The electric field is parallel to the bolometer axis. The azimuth scan is in the same plane.

-0.2

The bolometer axis is taken as collinear to the bias traces extending from the arms of the antenna. Radiation polarized orthogonal (cross-polarization) to the bolometer near the lower limit of the operating frequency will not encounter any significant radiating structures of the antenna or DC traces. On the other hand, co-polarized radiation at or even below the operating region will still encounter the DC bias traces outside the antenna, which will tend to act similarly to an electrically-larger loaded dipole. Due to the lens mount blocking incident radiation at angles greater than 48° off broadside, the measured radiation pattern at these large angles is no longer a function of only the antenna, but of the entire fixture [47]. The results at 95 GHz for -10 dB co-polarized and -10 dB cross-polarized were affected by reflections off the mount on the positive elevation scans. After adjusting the measurements, taking into consideration these reflections, the E-plane co-polarized -10 dB beamwidth measurement is reduced to 64.2° and the H-plane cross-polarized -10 dB beamwidth becomes 75.8°.

In summary, from the measured radiation pattern we can calculate the Gaussicity at the two frequencies to be 94% and 98% respectively. In subsequent processing described in the next chapter, this quantity had an influence on the choice of windows and two-
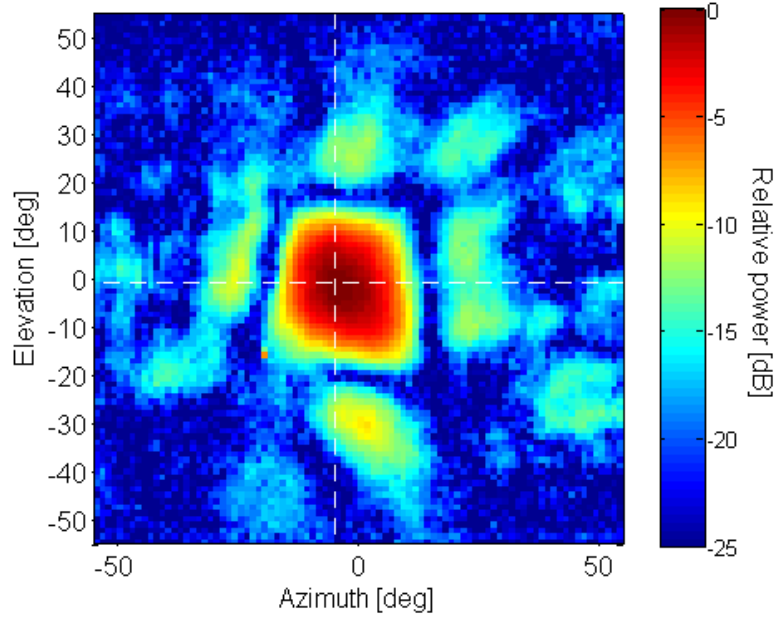
Figure 3.10: Two dimensional radiation pattern measured at 238 GHz. The incident electric field is linearly polarized and lies in the elevation plane, as well as the bolometer axis. The -3 dB beamwidths are 16.0° and 17.5° in azimuth and elevation, respectively.
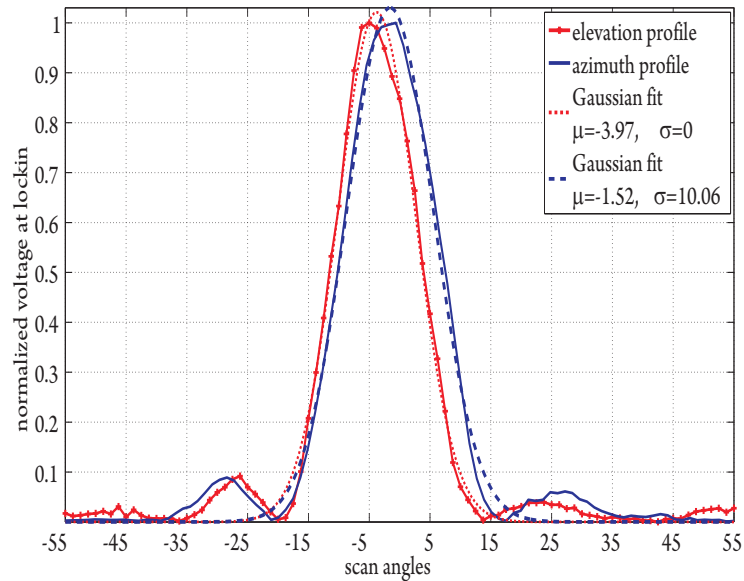
Figure 3.11: One dimensional cuts along horizontal and vertical axis at 0° from 2D patterns at 238 GHz. A Gaussian fit for both cases is also illustrated. The Gaussian fits are used to calculate the antenna's coupling to a Gaussian beam.

dimensional filters used.

Chapter 4

Single pixel millimeter wave imaging system: image processing

4.1 Introduction

This chapter presents a set of images acquired by the millimeter wave system described in Chapter 3 and discusses image processing with the goal of background noise suppression, edge detection. The images were acquired by: 1) linear scanning of a single pixel detector, 2) raster scanning a linear array of detectors, 3 conically scanning a linear array of detectors. The 0.1 to 1.2 THz images have 30,000 pixels and the goal is to detect concealed objects under clothing for images of a person at a range of 0.8 m-1 m with an integration time of 30 ms per pixel. The background temperature calibration is performed with a known hot-spot at 330 K, and the measured background fluctuation was 200-500 mK. Further details of the imaging system have been presented previously [6, 51–53].

Prior to image processing, the measured relative power data is calibrated and transformed into a radiometric temperature image in Kelvin. The algorithm presented here is described in Fig. 4.1. The image is pre-processed using an adaptive spatial noise removal filter which eliminates white Gaussian noise that is present in the scene and is caused by instrumentation. After filtering the image, a distance metric is computed on a pixel by

pixel basis. The image is then divided into eight different clusters. Each of the pixels are grouped based on the information obtained by the Euclidean and Mahalanobis distance calculation. The number of clusters is selected as a compromise between minimizing the centroid error within each cluster while maintaining a reasonable pixel count per cluster. Some prior knowledge of the scene is used for determining the number of clusters, e.g. knowing that the isothermal human body should be one cluster. Spatial information is added to the algorithm expecting that spatially neighboring pixels will not contain drastic temperature changes. This type of post-processing has been done in the past for hyperspectral image classification [54, 55].
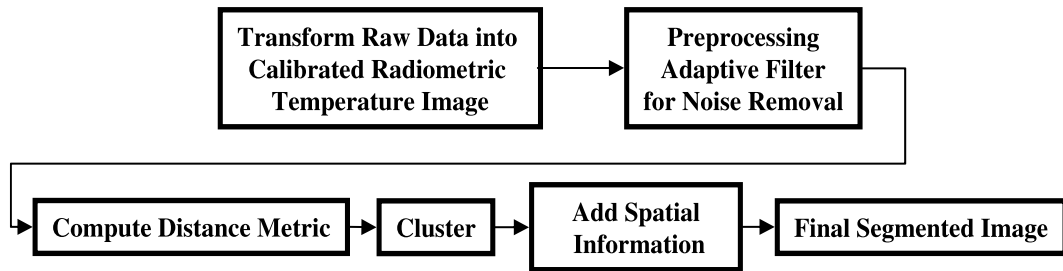
Figure 4.1: Algorithm for the segmentation of indoor passive Terahertz images for concealed weapon detection

4.2 Segmentation Algorithm

Unsupervised pattern recognition techniques offer the advantage of automatic clustering of any given dataset without the need of *a priori* class information. In unsupervised mechanisms, the clustering is performed by computing a similarity measure across the pixels in the image by a given distance metric. An illustration of pixel clustering is depicted in Fig. 4.2. In this figure, each colored function is a histogram of pixels with similar temperature values in the original calibrated image. The thresholds divide each of the groups depending on the temperature range of the pixels. The pixel similarity is only measured based on temperature. A commonly used clustering technique is

40
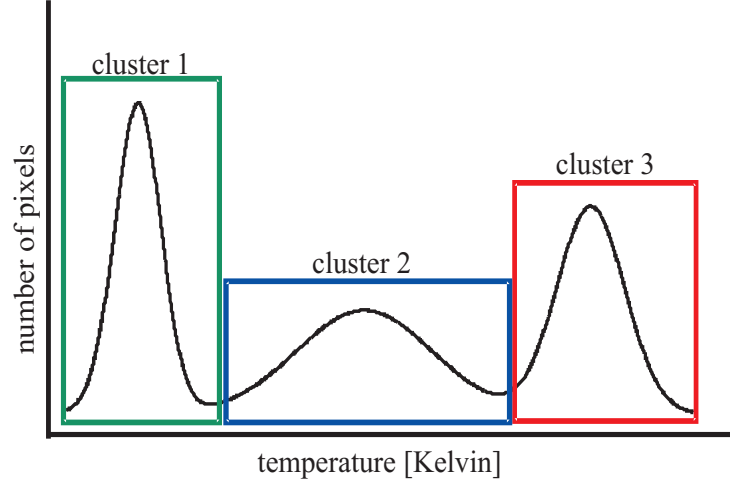
Figure 4.2: Sketch of pixel grouping defined by clustering algorithm. Each colored function is a histogram of pixels with similar temperature values in the calibrated image. The thresholds divide each of the groups depending on the temperature range of the pixels. The pixel similarity is only measured based on temperature, spatial proximity information is not considered in the clustering stage, but it is used in post-processing addition to further divide or combine the pixels in their corresponding clusters [54, 55].

the C-means clustering. This algorithm groups statistically similar data points by the information obtained from the Euclidean distance and the estimated mean for each of the classes. The Euclidean distance measures the similarity between pixel values $\boldsymbol{x_i}$ and $\boldsymbol{x_j}$ as

$$d_E^2(\boldsymbol{x_i}, \boldsymbol{x_j}) = (\boldsymbol{x_i} - \boldsymbol{x_j})^T(\boldsymbol{x_i} - \boldsymbol{x_j}) = |x_i - x_j|^2. \tag{4.1}$$

In this case, the pixels are one dimensional: $\boldsymbol{x_i}$ and $\boldsymbol{x_j}$ are single valued and are measured in degrees Kelvin. Therefore, points in the image containing similar radiometric temperatures will be considered *close* to each other, although they can be spatially separated. The iterative procedure of the traditional C-means algorithm with Euclidean distances will not be discussed in this paper and can be found in a number of references [56, 57]. In this work, the Mahalanobis distance was used as the metric. This metric is similar to the Euclidean distance, however it also takes into consideration the variability of the sample points. The Mahalanobis distance is given by

$$d_M^2(\boldsymbol{x_i}, \boldsymbol{x_j}) = (\boldsymbol{x_i} - \boldsymbol{x_j})^T \Sigma^{-1} (\boldsymbol{x_i} - \boldsymbol{x_j}) = \frac{|x_i - x_j|^2}{\sigma}, \qquad (4.2)$$

where Σ is the covariance matrix defined as the expected value of $\left[(\boldsymbol{x_i} - \mu_i)(\boldsymbol{x_j} - \mu_j)^T\right]$ and can be reduced to the standard deviation, σ, for single valued pixels. It can be observed that Eqn. (4.1) is the special case of Eqn. (4.2) when $\Sigma = I$.

The segmentation algorithm images is divided in two stages: (1) segment the temperature image data with a clustering algorithm; and (2) post-processing: addition of spatial information using k-nearest neighbors (k-NN). The k-NN algorithm [58] computes the spatial distance from a sample point to another. An unknown sample is classified to a nearest or similar sample point from the set. In this paper, the k-NN is used as the second stage of the algorithm. Sample points contained in the 2x2 nearest neighborhood is used to determine the final segmentation. The prescribed segmentation of the pixels in all images obtained with the single pixel imager is shown in Fig. 4.2 and is a result of the qualitative similarities between many images taken under similar conditions (e.g., indoors and at 0.8 m-1 m range).

4.3   Measured and Processed Image

The 30,000 pixel broadband image in Fig. 4.4 show a person with concealed weapons under clothing. The brightest region in the image represents the known hot object used for calibration which was a styrofoam cup with calibrated water temperature. The knowledge of the highest (hot object) and lowest temperature (room) in the image are used to fit the pixel values from the raw relative power data to a radiometric temperature image. Several weapons, namely a ZrO_2 knife, a metal gun, and a millimeter wave absorber, were concealed under different fabrics. The fabric were chosen to be the most common clothing fabrics: cotton, polyester, wind-blocker jacket and thermal sweater. The temperature resolution of the imager is 105 mK. The measured temperature contrasts ranged from 0.5-1 K for wrinkles in clothing to 5 K for a zipper and 8K for the concealed weapon. Figure 4.4 shows the calibrated images after noise removal with a

Wiener filter. The SNR increases from 19 dB for the measured relative power raw data shown in Fig. 4.3 to 24 dB after filtering the image in Fig. 4.4.
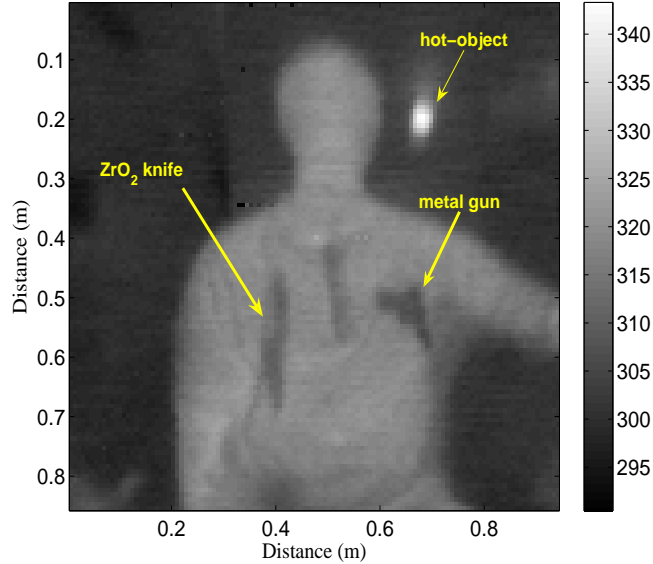
Figure 4.3: Unprocessed calibrated images. Concealed ZrO_2 knife and metal gun. Gray scale represents radiometric temperature in degrees Kelvin. A 25 pixel hot-object is used for calibration above 330 K. All images are courtesy of Dr. Erich Grossman, Optoelectronics Division-NIST, Boulder, CO.

After filtering the noise, the data is subjected to the clustering algorithm. The degree of similarity among pixels is computed by the Mahalanobis distance for all pairs of pixels. After the image is divided into the desired number of clusters, a second stage of adding spatial information is applied. Nearest neighbor information is included and a final map with cluster labels is produced. For the purposes of comparison, Fig. 4.5 shows the segmentation results using only traditional C-means with Euclidean distance and without addition of spatial pixel neighborhood information. In the following set of figures, each of the images are displayed by cluster label. The colors from the scale represent a cluster number, each pixel of the same color is assigned to the same group. This means, for example, that if a pixel is assigned to cluster 2 in Fig. 4.5(a) with the ZrO_2 knife, then all *similar* pixels based on the Euclidean distance measure are assigned to cluster 2. Note that the human body has been segmented into three different clusters
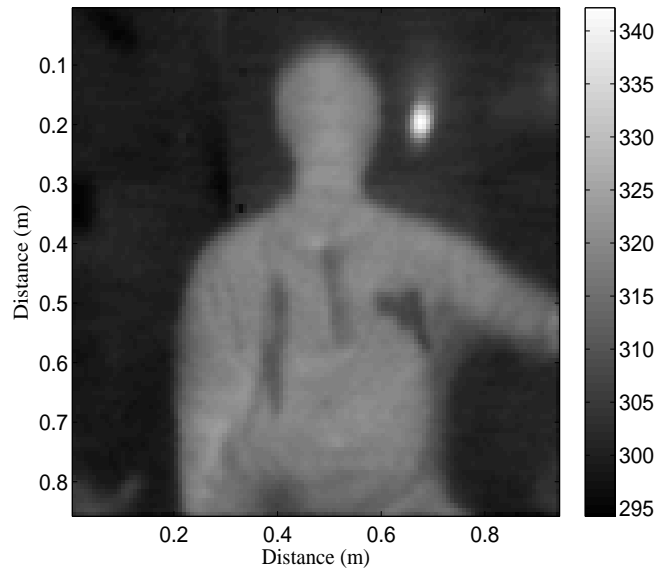
(a) Concealed ZrO$_2$ knife and metal gun
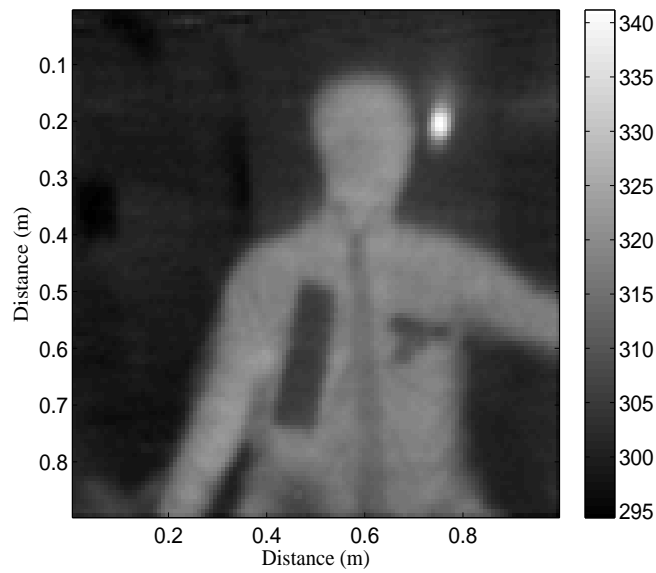
(b) Concealed millimeter wave anechoic foam and metal gun

Figure 4.4: Calibrated and filtered images. Gray scale represents radiometric tempera-
ture in degrees Kelvin. A 25 pixel hot-object is used for calibration above 330 K. The
Wiener filter removes instrumentation noise.

and that the ZrO$_2$ knife cannot be identified easily by observing the segmented image by

C-means only. However, note that in the Mahalanobis clustered image in Fig. 4.6 more

regions on the human subject are assigned to the same cluster. It can also be observed

that the shape of the ZrO_2 knife is better reconstructed and can be visually identified by the user. Another important note is that the gun has been identified in Fig. 4.6 as pertaining to a different cluster than the human subject and the edge of the body. This discrimination cannot be observed in the images clustered by C-means only. This implies that the addition of variance information from the Mahalanobis distance computation provides the algorithm with more discriminating capabilities when compared to the results of Euclidean distance alone.

4.4　C-means Clustering

Finally, the images were analyzed using an automatic pattern recognition technique known as *C-means* clustering algorithm. In statistical pattern recognition, the analysis performed on the data can be roughly separated into unsupervised classification (clustering) and supervised classification techniques. Currently, there are also a number of semi-supervised algorithms available, which combine unsupervised and supervised mechanisms that sometimes result in higher accuracy rates than unsupervised algorithms alone (e.g., [12, 56, 57]).

Unsupervised methods are those which do not require prior knowledge of the features in the data, and/or have *a priori* information of the labels and number of classes of the dataset. On the other hand, supervised classification techniques require prior knowledge of features and its dependent on a set of training samples. In a general sense, supervised algorithms tend to result in higher accuracy than unsupervised algorithms but their dependence on *a priori* information limits their performance when the data to be analyzed has unknown features. Also, supervised algorithms depend on the selection of the training set of samples; if they are chosen incorrectly, its statistics will not describe the data to be analyzed.

The idea of the C-means algorithm is to cluster data points (pixels) with respect to the nearest distance to clusters centers $\hat{\mu}_i$ where i corresponds to a class label. The

cluster centers are given by

$$\hat{\mu}_i = \frac{\sum_{k=1}^{n} \hat{P}(\omega_i|\mathbf{x}_k, \hat{\theta})\mathbf{x_k}}{\sum_{k=1}^{n} \hat{P}(\omega_i|\mathbf{x}_k, \hat{\theta})} \qquad (4.3)$$

where $\hat{\mu}_i$ is a the maximum likelihood estimate of the mean and $\hat{P}(\omega_i|\mathbf{x}_k, \hat{\theta})$ is the conditional probability density function of sample $\mathbf{x}_k$ belonging to class ω_i.

$$\hat{P}(\omega_i) = \frac{1}{n}\sum_{k=1}^{n} \hat{P}(\omega_i|\mathbf{x}_k, \hat{\theta}). \qquad (4.4)$$

Hence, the *C-means* algorithm can be described by an approximation of $\hat{P}(\omega_i|\mathbf{x}_k, \hat{\theta})$ to

$$\hat{P}(\omega_i|\mathbf{x}_k, \hat{\theta}) \simeq \begin{cases} 1, & \text{if } i = m \\ 0, & \text{otherwise} \end{cases} \qquad (4.5)$$

and calculating the Euclidean distance, $||\mathbf{x}_k - \hat{\mu}_k||$ of each point $\mathbf{x}_k$ in the image with respect to $\hat{\mu}_i$. The C-means algorithm is given by [58] as follows:

- begin initialize n,c, $\mu_1, \mu_2,...,\mu_c$
    - $\hookrightarrow$ classify n samples according to nearest μ_i
        - $\hookrightarrow$ recompute μ_i
    - $\hookrightarrow$ until no change in μ_i
- $\hookrightarrow$ return $\mu_1, \mu_2,...,\mu_c$
- end

4.4.1 Results of C-means clustering

The following figures show the result of a 5-means clustering application to calibrated millimeter wave images. Each of the colors in the image represent a class label; pixels having the same color represent pixels assigned to the same group (cluster) on the image.

For the addition of spatial information, the 2×2 neighborhoods are calculated and samples that are spatially close are assigned the same cluster number after comparing with the segmentation results using only the Mahalanobis distance. The pixels are re-clustered with the information provided by the 4-NN spatial information. The resulting images with the effects of adding spatially nearest neighborhood information is shown
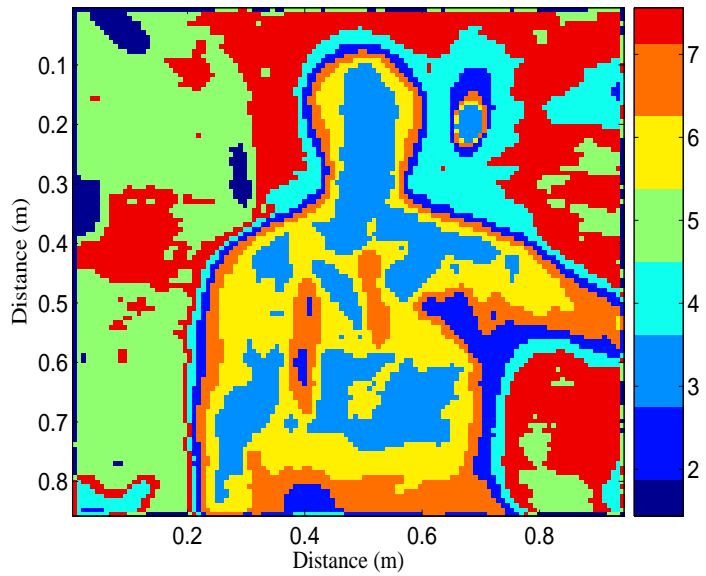
(a) Concealed ZrO_2 knife and gun
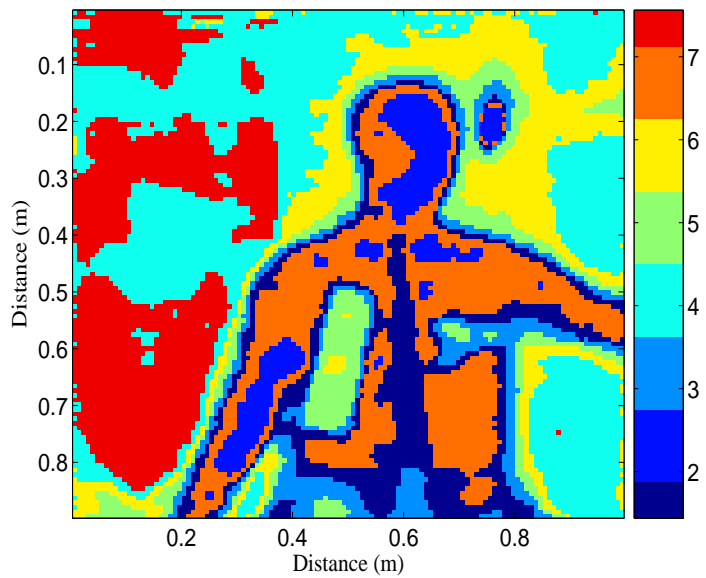
(b) Concealed millimeter wave anechoic foam and gun

Figure 4.5: C-means clustering of passive millimeter wave image from an individual at approximately 1 m standoff distance concealing a gun, a ZrO_2 knife. The water temperature is 69.4°C. Each color represents a cluster containing a set of objects with similar temperatures around a mean. The segmentation is based on the Euclidean Distance criteria.

in Fig. 4.7. The additional improvement in these images when using spatial information is minimal and probably not worth the extra computational time.
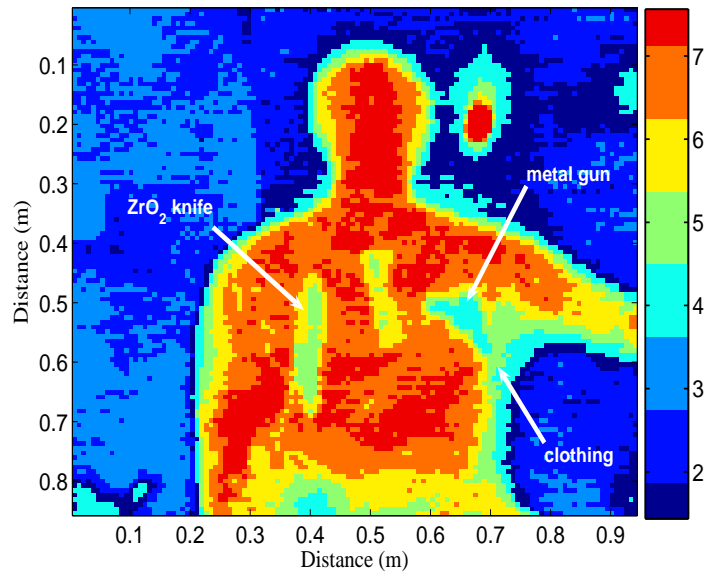
(a) Concealed ZrO_2 knife and gun
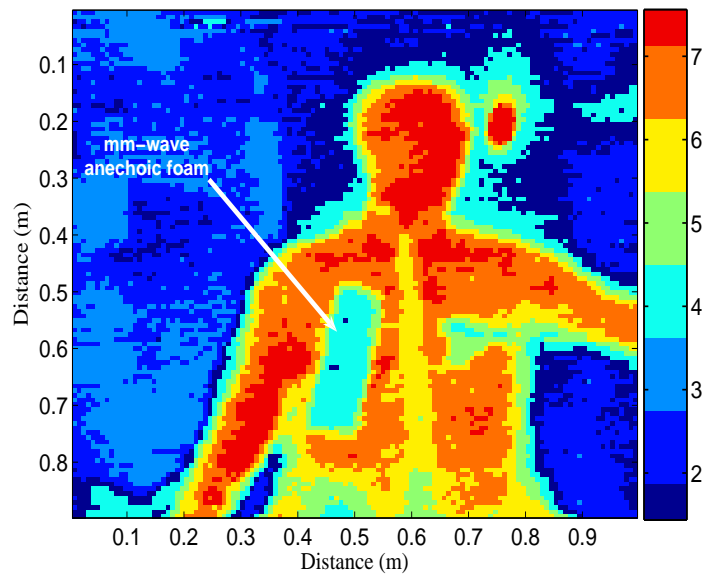
(b) Concealed millimeter wave anechoic foam and gun

Figure 4.6: Application of Mahalanobis Clustering Algorithm to a passive millimeter wave image from an individual at approximately $1\,m$ standoff distance concealing a gun, a ZrO_2 knife. Each color represents a cluster containing a set of objects with similar temperatures around a mean and variance. The segmentation is based on the Mahalanobis Distance criteria.

This section showed the results of segmentation of passive terahertz broadband images by using unsupervised classification mechanisms. The results of the clustering
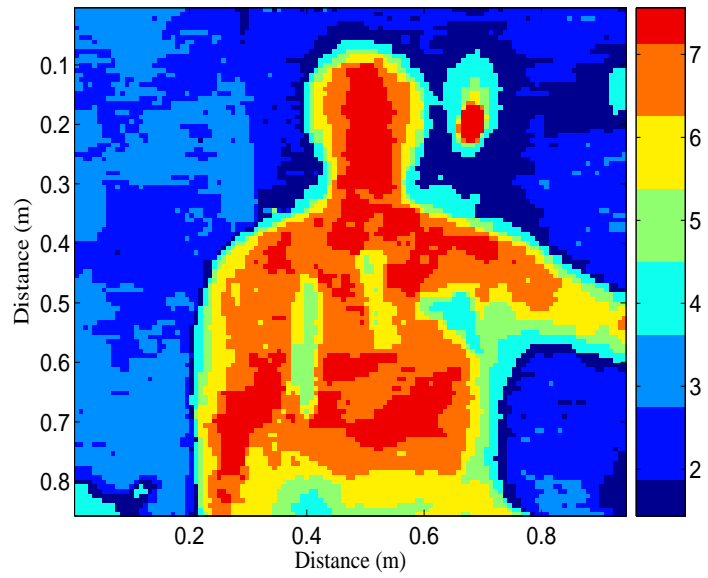
(a)
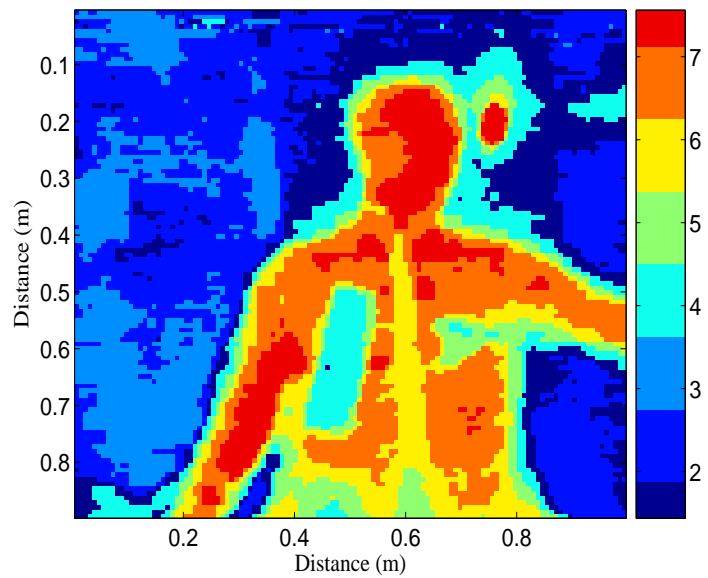
(b)

Figure 4.7: Post processing addition of spatial information using 4-nearest neighbors to segmented image results using Mahalanobis distance criteria

algorithms based on the computation of the Mahalanobis distance were compared to traditional techniques such as C-means clustering using only Euclidean distance. Once the images were clustered, spatial information was added to the results. The segmented

images show that the concealed weapons were visually identifiable for the images clustered by the Mahalanobis distance method. In figures 4.3 through 4.7, the images were pre-processed by simple noise filtering. The noise filtering was accomplished by using a two dimensional Wiener filter that removed white Gaussian noise from the data caused by instrumentation.

4.4.2   Extracting small temperature features

Commonly known techniques such as Canny edge detection, high-pass filters, and histogram equalization can also be used to improve image processing results. The algorithms presented on this section represent only a small subset of others more complex and robust algorithms that have been developed for image analysis and pattern recognition. The algorithms used here were meant to be used as exploratory techniques for the analysis of millimeter wave images.

Spatial Filters

Different types of pre-processing techniques can be used to reveal other features contained in the measured images but not visible in figures 4.3-4.7. For example, a texture filter based on the analysis of spatial standard deviation can be used [13]. Fig. 4.8 shows the result of processing the image with a 3×3 neighborhood standard deviation filter. The standard deviation of each 3×3 neighborhood was calculated and a new image was generated containing the resulting value for σ at each neighborhood. The use of this filter allows very small temperature differences across the image to become visually obvious.

Edge Detection

For edge detection in image processing, an edge is considered as a discontinuity of gray levels found amongst pixels. The edges are found by computing first and in some cases, second order derivatives of the image. Thus, for an image $I(x,y)$, with pixel index positions (x,y), an edge is found by,
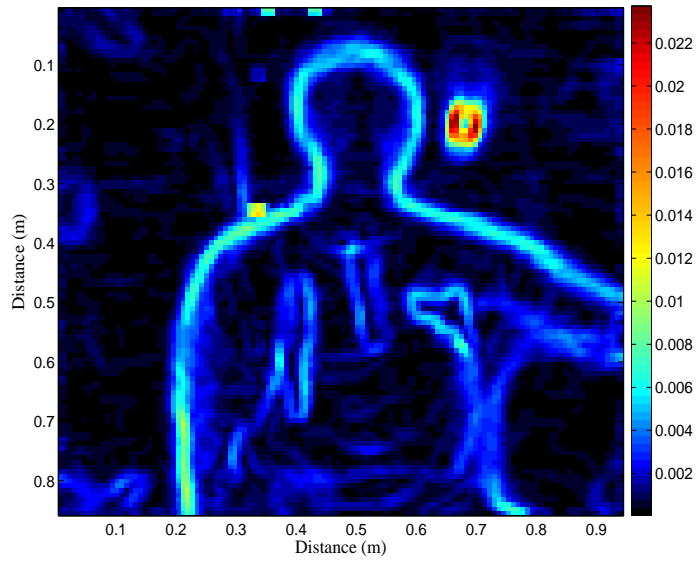
(a)
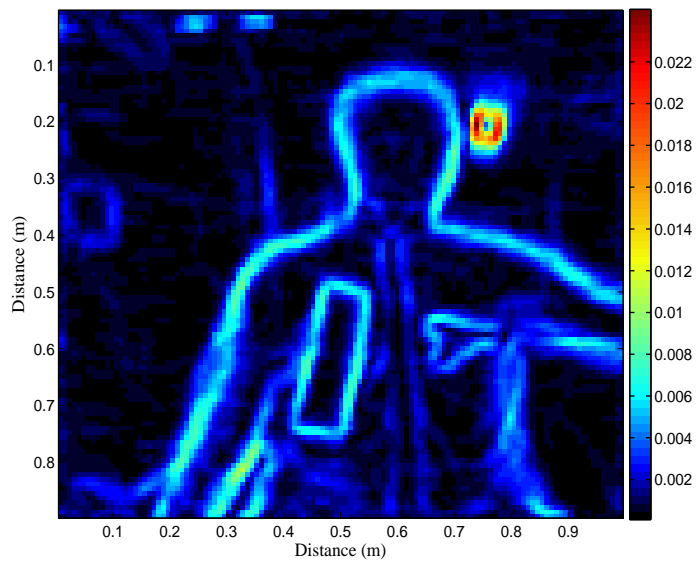
(b)

Figure 4.8: Processing of radiometrically calibrated image using a texture analysis filter. The 3x3 spatial neighborhood standard deviation is used to reveal small temperature differences across the image allowing them to become visually obvious.

$$\nabla \mathbf{I} = \left[\begin{array}{c} G_x \\ G_y \end{array} \right] = \left[\begin{array}{c} \frac{\partial I}{\partial x} \\ \frac{\partial I}{\partial y} \end{array} \right] \tag{4.6}$$

The direction of the edge is given by $\alpha(x,y) = \tan^{-1}\left(\frac{G_y}{G_x}\right)$. The edge detection results shown in Fig. 4.4.2 were obtained using a Canny edge detector. In general terms, the detector is divided into two stages: 1) smoothing of the image (Gaussian filter), 2) computation of its gradient (edges).

The gradient for the edge detection is found using Eqn.(4.6) and the smoothing filter is given by,

$$H(u,v) = \exp^{(D^2(u,v)/2\sigma^2)} \tag{4.7}$$

where $D(u,v) = \sqrt{(u - M/2)^2 + (v - N/2)^2}$ is the distance from any point (u,v) in the image $\in \mathcal{R}^{[M \times N]}$ to the center of its Fourier transform [13]. By using edge detection and smoothing, an output image is created where the white noise has been removed and edge features will indicate spatial regions with changes in temperatures from the original scene. The following figures in 4.4.2 and 4.4.2 are the results of applying Canny edge detection and smoothing to various millimeter waves images. The matrix dimensions of the images are (M=109, N=122) pixels.

Histogram Equalization

For a given digital image $I(x,y)$, its histogram can be described by the probability distribution of the gray levels in $I(x,y)$ from an interval $[0, L - 1]$, where L is the maximum gray level of a pixel (i.e. 255 for uint8 images). Its histogram can be defined with a discrete function $h(r_k) = n_k$ where r_k is the kth gray level, and n_k is the pixel number corresponding to gray level r_k [13]. The function $h(r_k)$ can be normalized to become,

$$p(r_k) = \frac{h(r_k)}{n} \tag{4.8}$$

where n is the total number of pixels in the image.

Histogram equalization attempts to create a discrete function $h(r_k)$ to distribute the gray levels of all pixels in an image across a uniform probability density function. The transformation to map the pixels from the original gray level distribution to a uniform
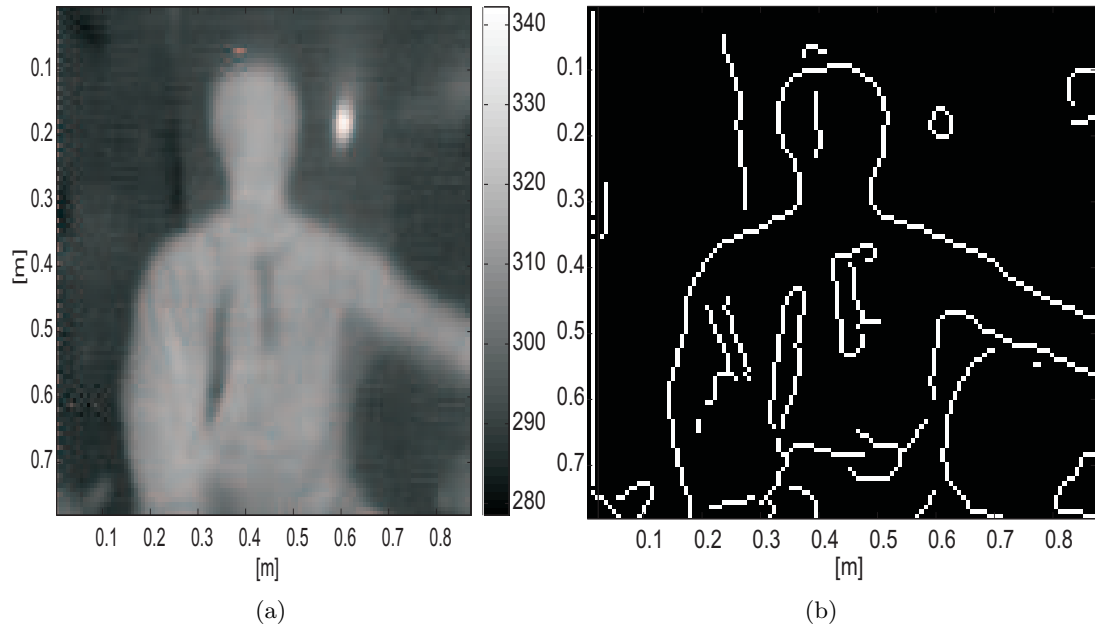
Figure 4.9: Edge detection using Canny filter of a passive millimeter wave image from an individual at approximately 1 m standoff distance concealing a gun, a ZrO_2 knife. The water temperature is 67.8°C; (a) original calibrated raw image, (b) results of processing the raw image with a Canny edge detector.
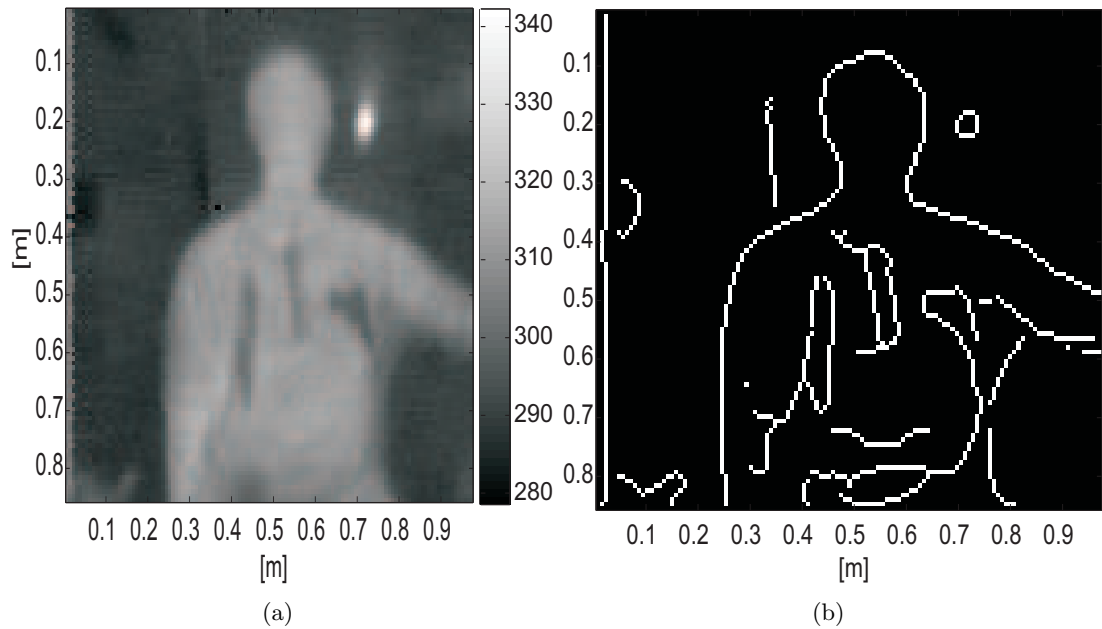
Figure 4.10: Edge detection using Canny filter of a passive millimeter wave image from an individual at approximately 1 m standoff distance concealing a gun, a ZrO_2 knife. The water temperature is 69.4°C; (a) original calibrated raw image, (b) results of processing the raw image with a Canny edge detector.

distribution is achieved by,

$$s = T(r) = \int_0^r p_r(\omega)d\omega, \tag{4.9}$$

where ω is a dummy integration variable and r is a random variable in the interval $[0, 1]$ that can also describe the gray levels in the image. Using this transformation allows for higher contrast in the image, since the pixel intensities are now distributed across all the gray levels spectrum. An example of histogram equalization and its effects on image quality is shown in Fig. 4.4.2.
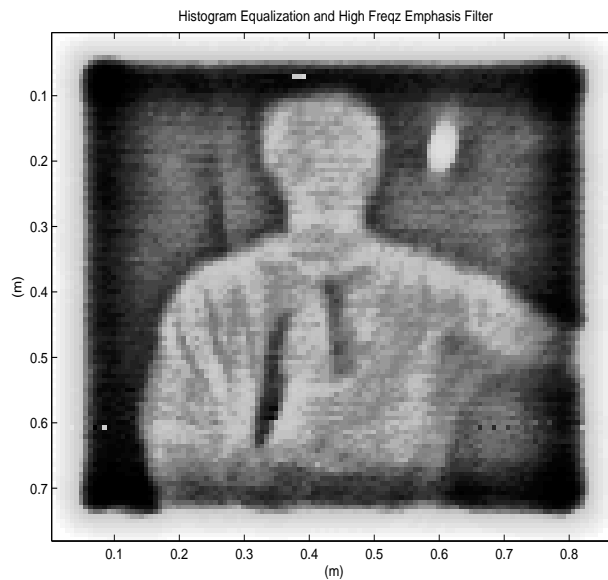
Figure 4.11: Resulting image from applying histogram equalization to calibrated image. Subject is at approximately $1\,\mathrm{m}$ a ZrO_2 knife.

In conclusion, this chapter discusses image processing algorithms applied to the images from the single pixel millimeter wave imager described in Chapter 3. Pixel blurring due to non-ideal Gaussicity, white noise caused by instrumentation, prior knowledge of the controlled indoor image scene, were some of the parameters used to develop the appropriate image processing algorithms. The system has an excellent temperature resolution of $105\,\mathrm{mK}$ but nevertheless additional processing using spatial filters revealed features not visible in the raw images. An interesting result in the processed images was that by detecting small temperature changes, small spatial features were revealed

in the images, with the best example being folds in the clothing. It was shown that simple image processing techniques are useful for fast visual concealed weapon detection and exploratory analysis for the case of broadband passive millimeter wave images with low signal-to-noise ratio and low pixel count. In the case of the C-means algorithm real-time performance was not achieved due to the nature of the distance metric calculations. However, lower order statistics and/or a lower number of clusters can be computed to improve performance speed. The algorithm can also be implemented on a DSP chip due to its relative simplicity.

Chapter 5

Image processing for a linear array passive millimeter wave imager

The previous chapter showed a set of passive millimeter wave images acquired by a single detector. Although the quality of the images allowed for visual identification of the concealed weapons, the integration time was $30\,\mathrm{ms/sample}$. At this integration rate, a scan of a subject in an area of approximately $1\,\mathrm{m}\times1\,\mathrm{m}$ will take 15-20 minutes, requiring that the subject does not move during this interval to eliminate artifacts in the image. If the subject moves slightly, it will show in the image as horizontally shifted pixels. It is obvious how this requirement can become a problem if used at an airport security portal for screening passengers. Hence, decreasing the scan and processing time is essential for this type of security application, and also moving a step closer to the goal of real-time operation.

One way to decrease scanning time is to use more than one detector. An N-element detector array allows faster scanning, since it reduces the number of detectors by a factor of N, in the case of a row-based raster scanning. However, adding more detectors can also add artifacts to the image. These can be observed as streaks, usually caused

by differences between the responses of the N detectors. These non-uniformities are due to variation in DC bias offsets, bias drifts, poor electrical connections, noise in specific channels or fabrication differences. Hence, in order to produce a visually higher quality image, these streaks need to be removed without sacrificing resolution. This chapter shows raw and processed images sampled using a row based raster scan with a 1×8 linear array. The results of removing non-uniformities using image contrast enhancement, spatial filtering and thresholding are presented.

5.1 Linear array passive millimeter wave images

This section introduces passive millimeter-wave images measured with a multiple linear column detector array, by mechanical row-based raster scanning at a standoff distance of 2 m. The setup and the receivers are similar to those shown in Chapter 4. The linear array consists of 8 spiral antennas identical to the ones described in Chapter 3. Fig. 5.1 shows the 1×8 linear detector array with center-to-center spacing of 4 mm used to acquire the images shown this chapter. Each Si lens is 2 mm in diameter. The array and millimeter wave imaging system were designed by Drs. Erich Grossman and Charles Dietlein at the Optoelectronics Group, National Institute of Standards and Technology. All images presented in this chapter are courtesy of NIST.
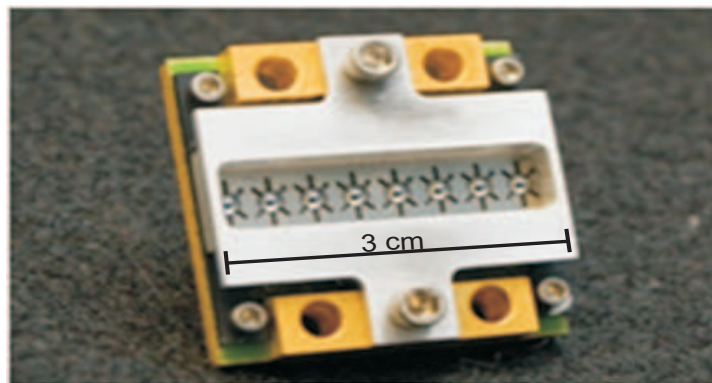
Figure 5.1: Photograph of a 1×8 linear array of detectors. Each lens is 2 mm in diameter and has a spiral antenna coupled micro bolometer on the back. (Photo courtesy of Dr. Charles Dietlein)

The image acquisition using the linear array varies from that of the single pixel; in this system each of the detectors in the linear array is scanning a *row* of the scene. The magnification of the quasi-optical system design is approximately 10, hence the spacing of the pixels on the image plane is around 35 to 40 mm. Each detector simultaneously measures a row of the scene, across the horizontal direction, and when 8 rows are completed the next 8 rows are scanned with the last row overlapping in some cases. The acquisition time for the same area is thus reduced by a factor of eight. Each detector is connected and biased independently but non-uniformities can occur due to physical variations during fabrication, poor electrical connections, bias offsets, or noise in the readout system. A block diagram in Fig. 5.2 shows a description of the image acquisition of the raster-scanned linear array system. Incoming black-body radiation is received by the antennas and coupled to the bolometer, which are noise matched to the readout FET amplifier [59]. The signal is then sent to a data acquisition card and recorded in a personal computer for processing and display.

Fig. 5.3 shows the artifacts introduced into the image caused by noise in the detectors and differences in responsivities. Notice in the figure the dark stripes caused by one of the eight channels having a degraded electrical connection. Fig. 5.3(b) is the case when noise is present in one of the eight channels. In order to remove these and similar effects which lead to differences in the received signal from the array elements, a thresholding mechanism can be applied to the scan lines (rows). The threshold will depend on the image global mean and standard deviation along scan lines. An example of streak removal for a linear array of detectors process is described in [60] where it is experimentally shown that the global intensity average of the image is not dramatically different from the mean intensity on each detector. Based on the same assumption, a threshold can be applied in the case described here by computing the average of all scan line samples and creating a global mean, $\hat{\mu}$, and standard deviation, $\hat{\sigma}$ dependent on horizontal position on the scan. For the case of noisy channels, all those exceeding the threshold given by:

$$\tau = \hat{\mu}_{rows} + 2.5\,\hat{\sigma}_{rows}, \tag{5.1}$$
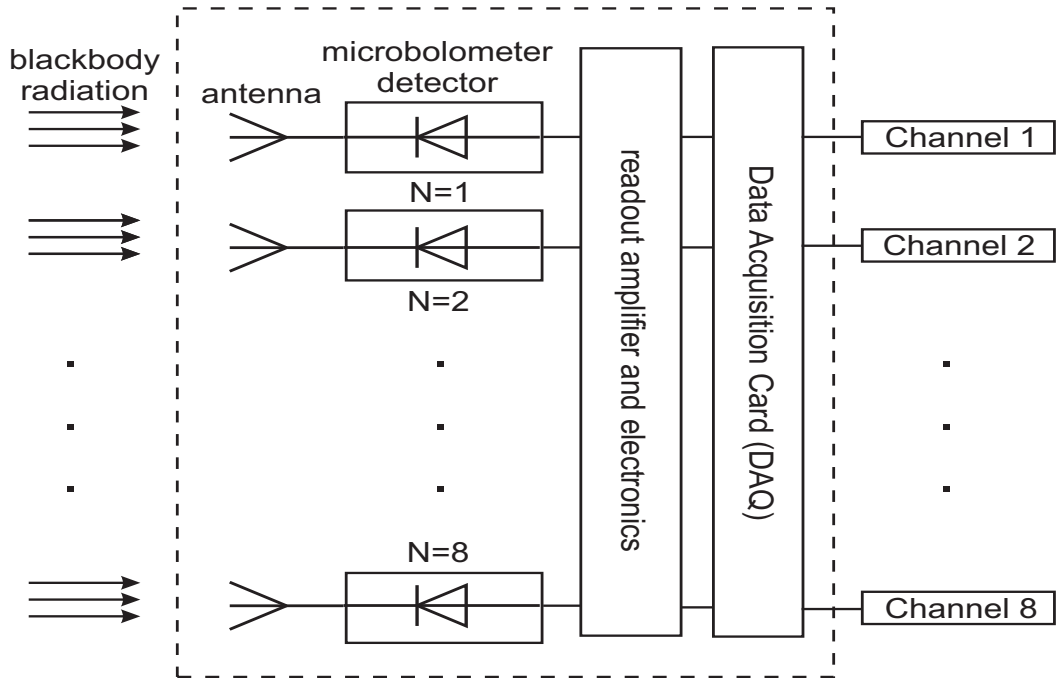
Figure 5.2: Block diagram describing the image acquisition process using an 8-element array row based scanning system. Incoming black-body radiation is received by the antenna inducing a temperature change on the bolometer, measured by a change in resistance. The bolometers are noise matched to the readout amplifiers and subsequent electronics.

will be removed or replaced by the average of the two neighboring scan lines. After computing the mean and standard deviations as a function of the sample position in the horizontal scan direction, the threshold is determined. In this case, the goal is to remove the signals coming from the abnormal detector measurement that exceed 5.1.
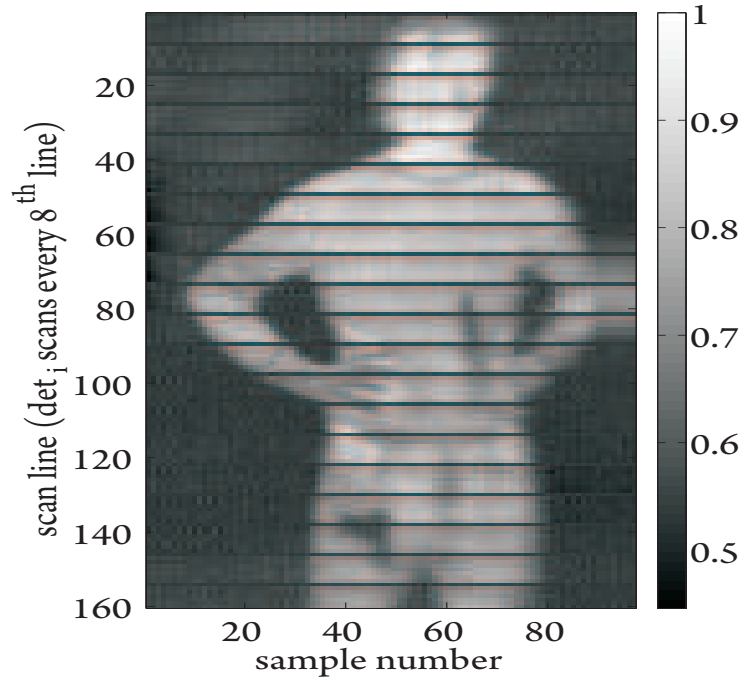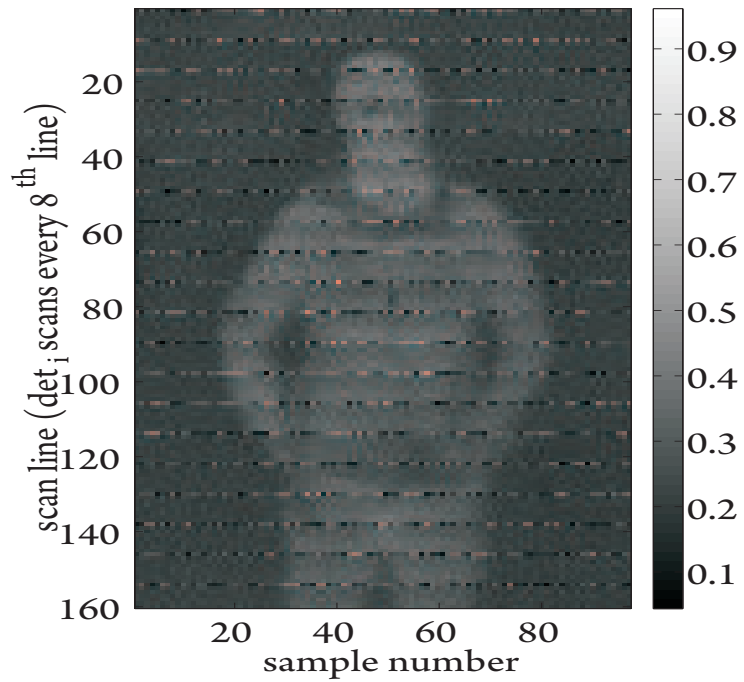
Figure 5.3: Images acquired by linear array of spiral ACMB using row-based raster scanning. Notice that the minimum values displayed on each image are different for ease in visualization. Each image is normalized to its own global maximum. Each pixel in the raw image covers an area of around $3\,\mathrm{cm}^2$. (a) Subject concealing metallic gun at standoff distance of $2\,\mathrm{m}$. The dark scan lines in the images are indicative of a non-functional detector due to bad electrical contact. (b) Subject concealing a metallic gun under a leather belt. Detector number 8 shows higher noise levels than other detectors in the array.
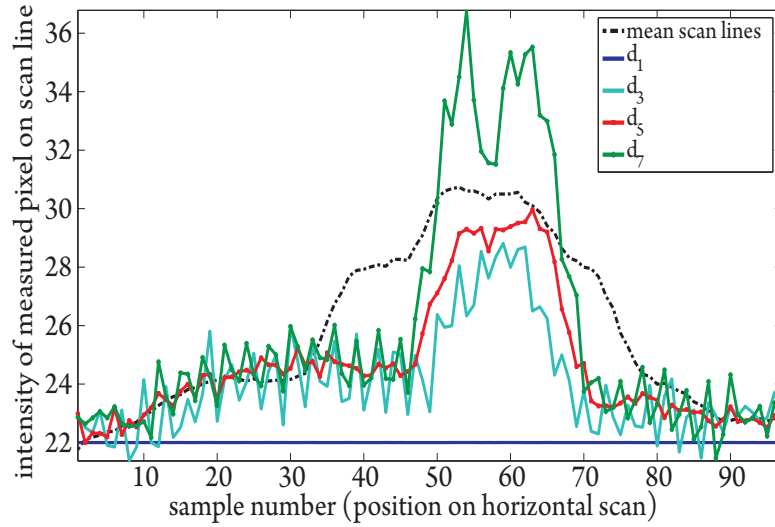
(a)
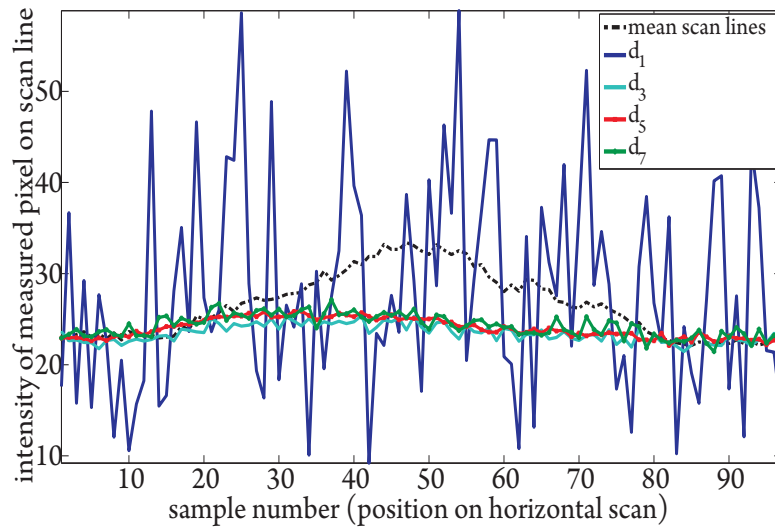
(b)

Figure 5.4: Intensity of measured pixels along each row plotted for seven rows. A row corresponds to a measurement from a detector in the 1x8 array. (a) measurement for the case when one detector (d_1) is non-functional and (b) measurement for the case when one detector (d_1) is noisy. The global average for all scan lines is plotted for comparison. The streak removal technique identifies the row with values exceeding a threshold, $\tau = \hat{\mu}_{rows} + 2.5\,\hat{\sigma}_{rows}$, and replaces the scan line values by the average of the two neighboring channels.

61

In some cases, there will be a channel that is completely non-functional. In this case, the detector will not measure a signal on a scan line, thus been expressed as a completely black row (empirically identified as regions of constant intensities) on the image. A similar thresholding method is used to remove the rows corresponding to non-functional detectors. The threshold algorithm identifies channel with a constant derivative along the horizontal scan direction in the image and removes from the measured data. Similar to the case of channels with excessive noise, the values in the image coming from non-functional channels are replaced with the average of the two neighboring scan lines. The thresholding algorithm used to remove the noisy and non-functional detector stripes is based on removing abnormal signals as those depicted for example in Fig. 5.4.

The images in Fig. 5.5 are of a subject concealing a resolution target under a sweater. A resolution target is a test pattern object used to resolve the power of an imaging systems. It usually has a group of bars with different widths. In general, the resolution limits of an imaging system can be determined by the widest bar that cannot be discriminated [61]. An optical image of the resolution target used as a concealed object is presented in Fig. 5.6. The bars of the resolution target are made of copper tape with sizes ranging from 10 mm up to 20 mm.
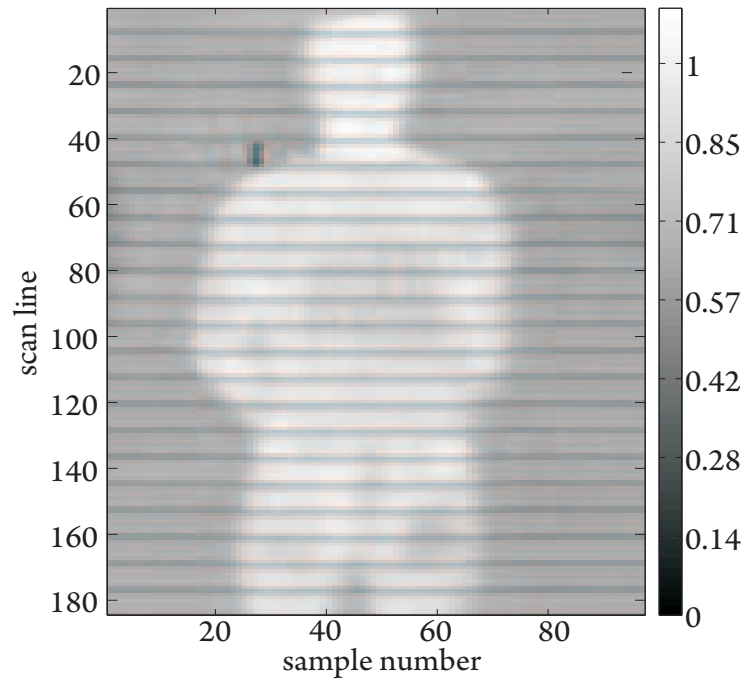
(a)
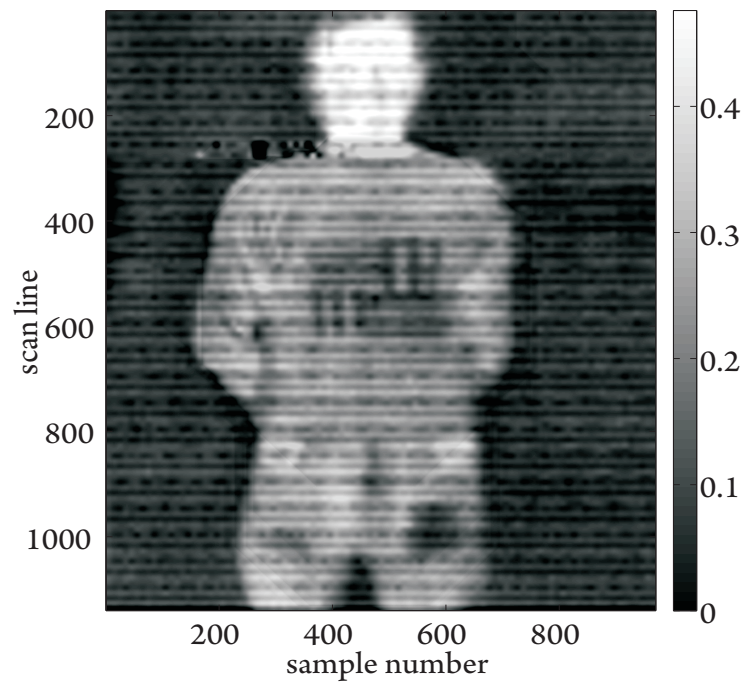
(b)

Figure 5.5: Examples of images acquired by an 8-element linear array of spiral antenna-coupled micro-bolometers using row-based raster scanning. Notice that the minimum values displayed on each image is different for ease in visualization. Each image is normalized to its own global maximum. Each pixel in the raw image(a) covers an area of around $3\,\mathrm{cm}^2$ (a) Raw and unprocessed image of subject concealing a test pattern (resolution target) under a sweater at a standoff distance of $2\,\mathrm{m}$. The dark scan lines in the images are indicative of non-functional pixels due to poor electrical contact on the eighth detector. (b) Upsampled image at 10x and using automatic streak removal with contrast enhancement.

Figure 5.6: Resolution target used as concealed object in linear array images. The bars are made of copper tape and vary in size from 10 mm up to 20 mm.

Using interpolation and up-sampling can sometimes add artifacts to the image. However, in the cases studied here, it was observed that interpolation did not change significantly the real pixel intensities and also improved the visual quality and discrimination of the concealed objects in the image. The signal-to-noise ratio was also improved. On the original raw image shown in Fig. 5.5(a) the $SNR = 5.25$ while after processing is improved to $SNR = 6.2$ in Fig. 5.5(b). This improvement on the small spatial features of the image can also be observed in Fig. 5.7. This figure shows a one-dimensional cut (profile) across the horizontal scan direction of the image (a scan line by one detector). The solid line shows the interpolated cut and the red points indicate the original values taken from the raw image. In Fig.5.5 the subject is concealing a resolution target which is visually identifiable after applying the automatic streak removal and the interpolation algorithm.

A post-processing step in the spatial domain is performed after the automatic stripe removal to enhance the image contrast using adaptive histogram equalization. A gray scale transformation, $T\left[f(x,y)\right]$, is applied to the image without the stripes. The transformation T can be chosen from several mapping functions to either stretch or compress

(a)

(b)

(c)
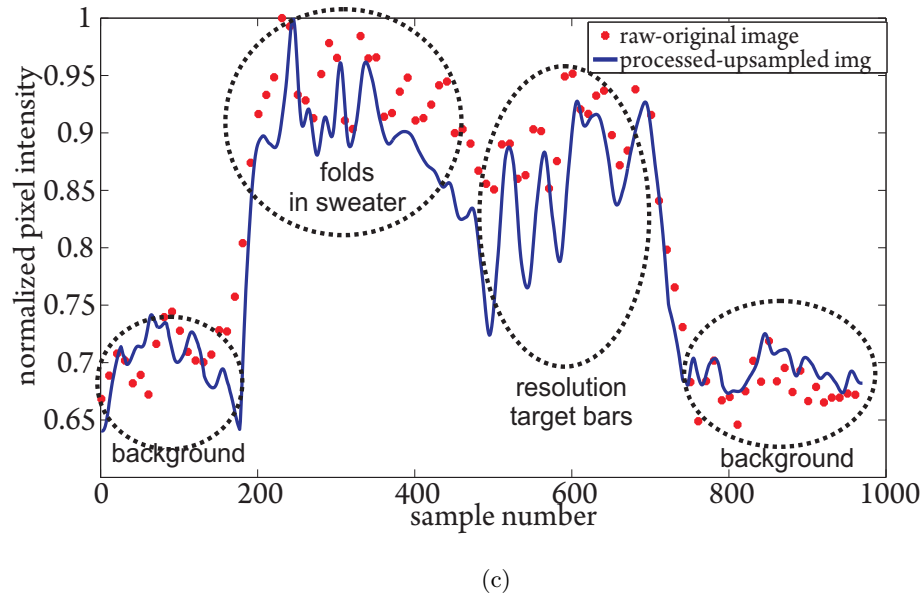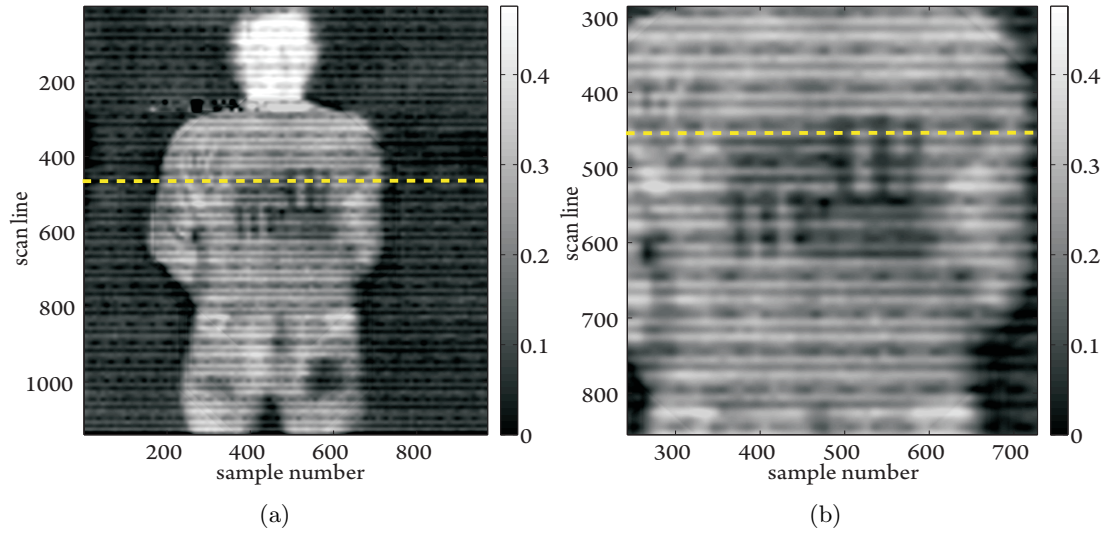
Figure 5.7: (a) One-dimensional cut across horizontal scan direction of the image, b) zoomed in region of the cut, (c) plot of the normalized pixel intensity along the cut. The solid line shows the interpolated and processed pixels, the red points indicate the original values from the raw image. The features on the clothing, such as folding, as well as the concealed resolution target are enhanced using interpolation, revealing the dips between peaks of intensity. These dips in turn bring out features that cannot be seen in the raw image.

the dynamic range of the data. The gray scale transformation weighs the input pixel values depending whether the output values are desired to enhance higher (brighter) pixels or lower (darker) samples. The weighting of the transformation is achieved by

modifying the T as shown in Fig.5.8. For values of $g < 1$ the pixels are weighted towards brighter output values, for $g > 1$ the weighting favors darker outputs, and $g = 1$ is a linear mapping from input pixels to output pixels.
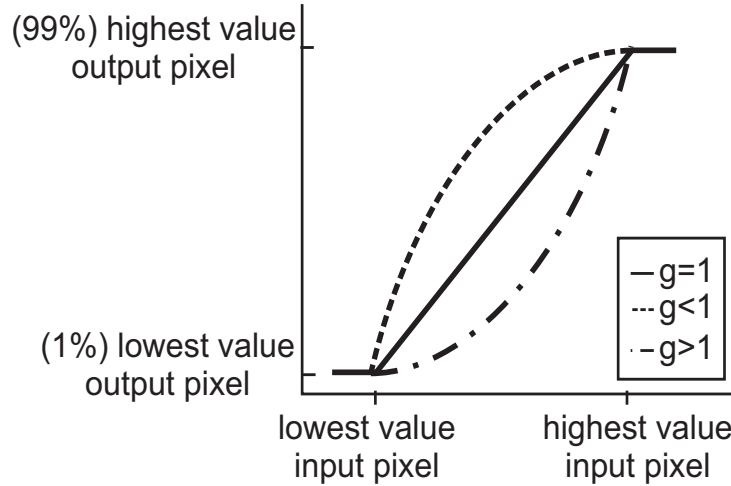
Figure 5.8: Various intensity transformation functions to map intensity values in gray scale image. The processed pixel intensities are such that 1% of the pixels are saturated at low and high intensities of the raw data. This increases the contrast of the output image. Varying the values of g changes whether the brighter or darker input values are weighted higher than others. In the case of $g < 1$ the mapping is weighted towards brighter values, for $g > 1$ the darker values are weighted, $g = 1$ is a simple linear mapping from input to output.

The histogram adjustment used as post processing for the images shown in Fig. 5.5 saturates the 1% darkest and brightest regions in the image and stretches the remaining 99% of the values to fill the dynamic range of a gray-scale image of values $(0, 255)$ [13]. In addition to the contrast enhancement, the background is further processed and removed from the scene, thus enhancing the features on the foreground of the image. Additional examples of processing the passive millimeter wave images using these techniques are shown in Figs. 5.9 and 5.10. For the case in Fig. 5.9, the SNR on the raw image (a) was 4.10. After automatically removing the stripes and thresholding the signals from the noisy detectors, interpolation and contrast enhancement were applied (b). This resulted in an improved signal-to-noise ratio of 5.14 and a higher visual quality, facilitating the visual identification of the concealed gun under the belt. For the images presented in Fig. 5.10 the processing produced an SNR of 6.01, compared to 5.9 from the raw image.
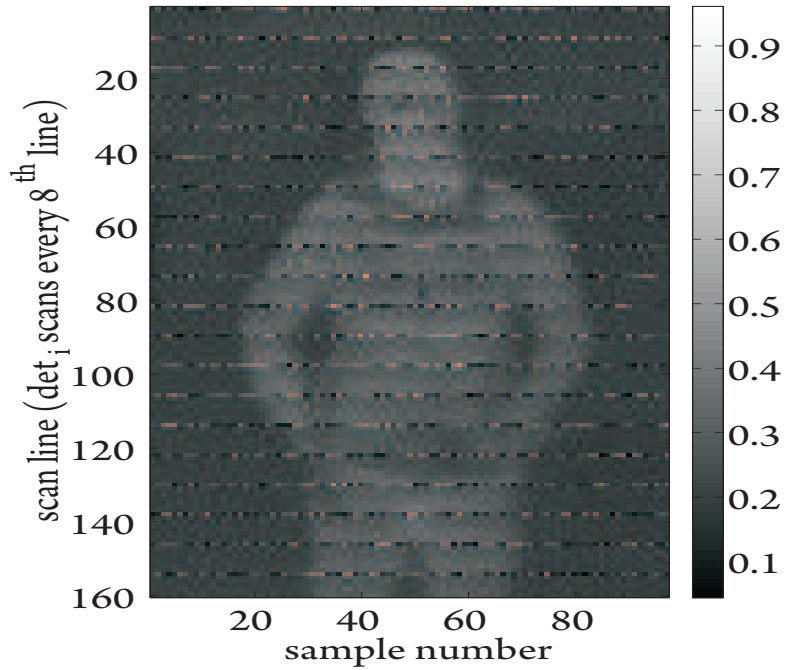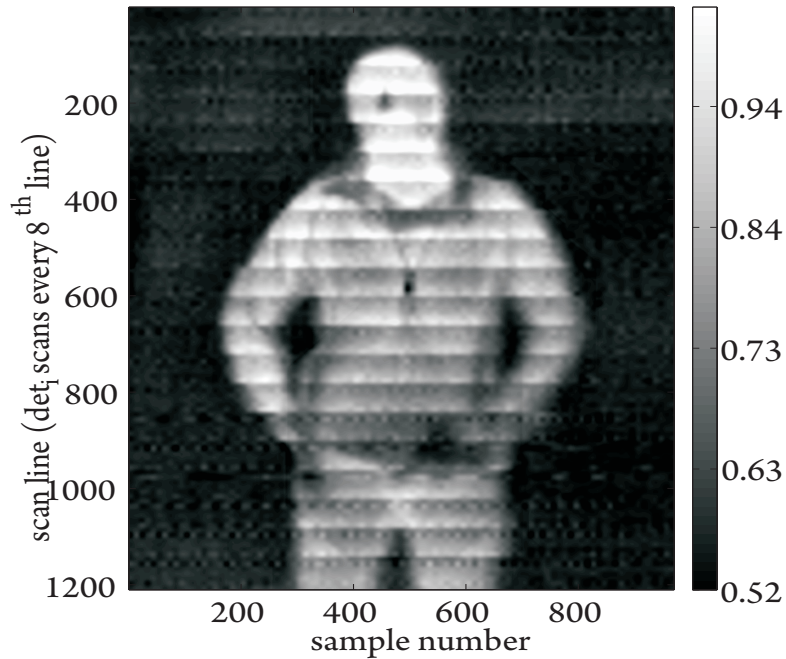
Figure 5.9: Examples of raw (a) and processed (b) images acquired by an 8-element linear array using row-based raster scanning. The noise lines in (a) are due to a single noisy channel. The subject is concealing a metallic gun at standoff distance of approximately 2 m under jeans and leather belt. After the processing the following features, visually undetectable in the raw image become obvious: zipper, collar, folds on the clothing, hand in pocket, low leather belt, and another artifact behind the belt, because of the low resolution it is not obvious that this artifact is a weapon.
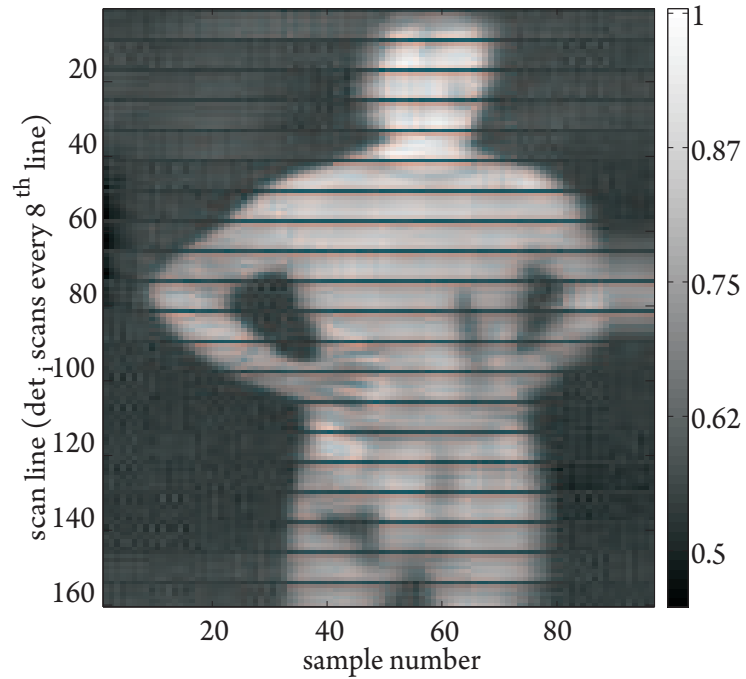
(a)
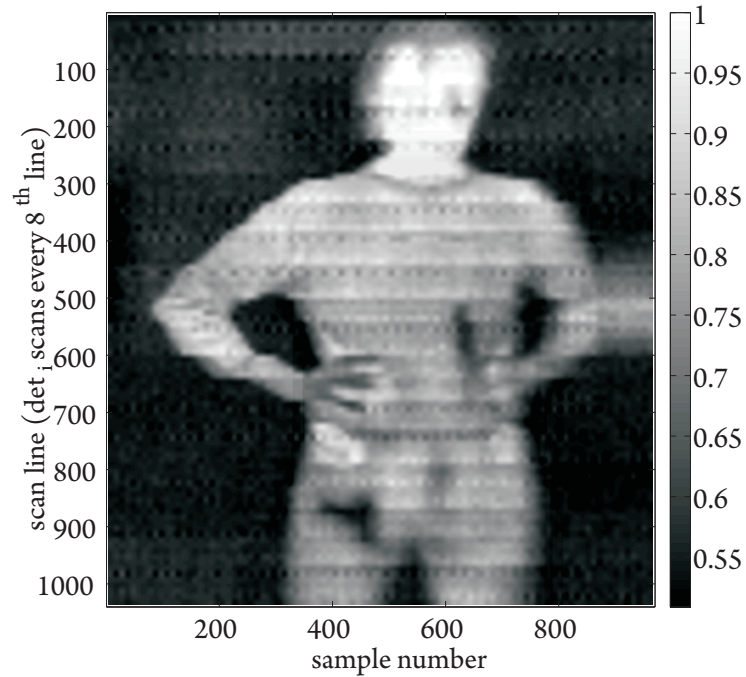
(b)

Figure 5.10: Examples of a good raw image (b) and processed images which increased the SNR. The subject was concealing metallic gun at standoff distance of approximately 2 m. The dark scan lines in the images are indicative of a non-functional pixel caused by poor electrical contact on the eight detector. The processed image using streak removal, interpolation, and contrast enhancement.

5.2 Conical Scan

The previous section showed images that were acquired by row raster scanning using an 8-element linear array of antenna coupled microbolometers. In order to cover a larger field of view (FOV) in real time (30 frames/sec), a longer linear array with a conical race-track scanning mechanism was implemented at NIST. The design of the conical scanner is based on a Schmidt telescope architecture [62]. This design covers a larger FOV area of $4\,\mathrm{m}\,\mathrm{x}\,2\,\mathrm{m}$ with optics designed to reduce aberrations. The detectors for this system are set up as a linear $1\,\mathrm{x}\,64$ array where each consists of an antenna coupled microbolometer coupled to a Si lens.

In this chapter the sampling grid, detector efficiencies, and geometrical spot size were obtained from an optical simulation software called ASAP (Brault Research Organization) and the imaging system designed by Dr. Erich Grossman at NIST-Boulder. The sampling grid (pseudo-target plane) covered by the conical scanner is shown in Fig. 5.11 were the non-uniform sampling is seen on the pseudo-target plane. Here (x',y',z') denote coordinates on the image plane. These are not the same as the (x,y,z) coordinates due to a tilt in the imaging system but the transformation to (x',y',z') is straightforward. The simulated optics and conical scanner show the predicted image characteristics of the initial version of the imaging system using 64 detectors sampling 256 positions. Each sample is taken every 1.4 degrees.

The results of the ASAP simulation give the distribution of efficiencies across the field of view. There are approximately 16,000 points sampled by 64 detectors at 256 angle positions. For each of these positions in (x,y,z) there is an estimated detector efficiency and geometric spotsize. The efficiency takes into account losses due to obstructions introduced to minimize aberration, as well as diffraction and absorption which are small. The efficiency distribution across the field of view is shown in Fig. 5.12(a). In Fig. 5.12(b), a histogram of the 16,000 simulated sample points shows that the overall average efficiency is approximately 29%. This is mainly determined by the efficiency of the conical scanner (55%) and that of the Schmidt optics (63%) [7].
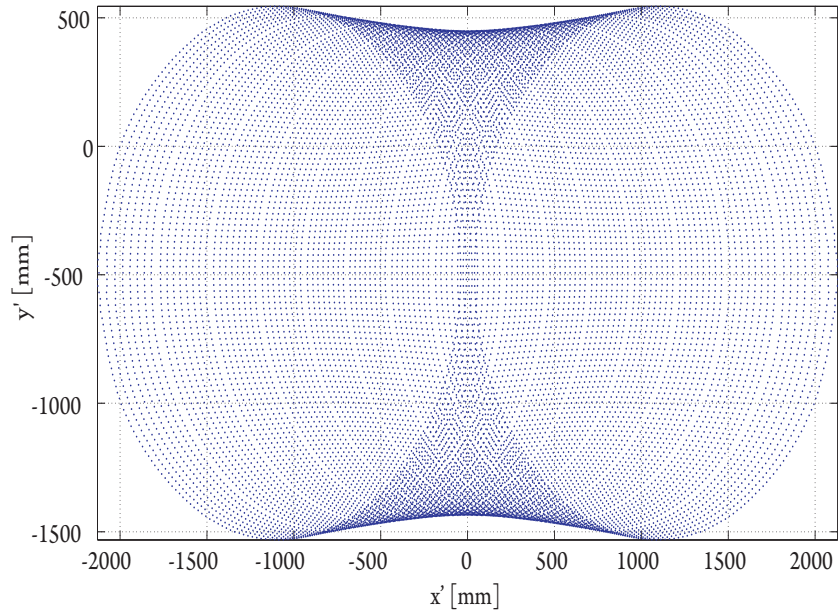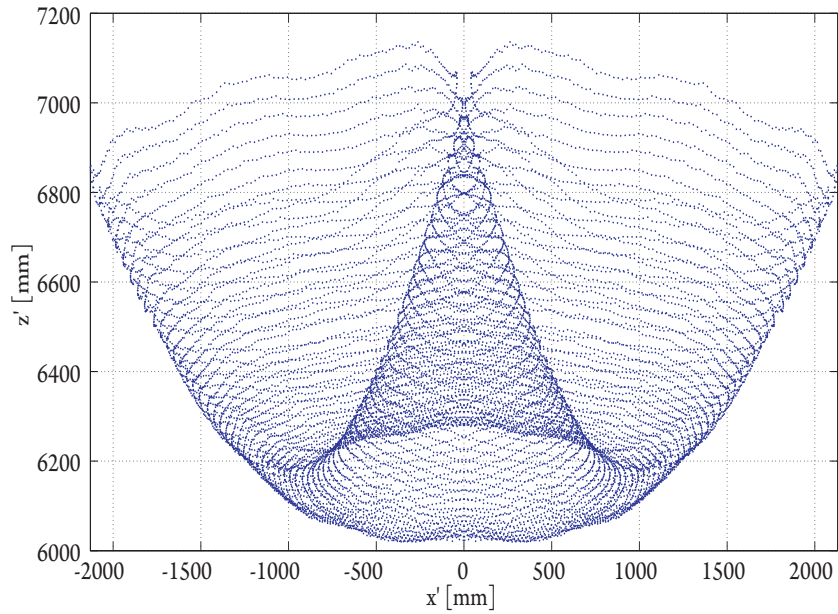
Figure 5.11: Field of view of 2 m by 4 m target plane covered by the race-track sampling mechanism. Each of the 16,000 blue dots represent a position on (x',y',z') where a signal is to be recorded (center of pixel position). The system is simulated using ASAP for a 64-element linear array in a Schmidt telescope design. (a) Top view of the target plane showing the 4 m x m FOV coverage, (b) Side view of FOV coverage showing the sampling positions at a range of 6 m to 7 m.

For the geometric spotsize, the flat reflector was used to reduce spherical aberra-
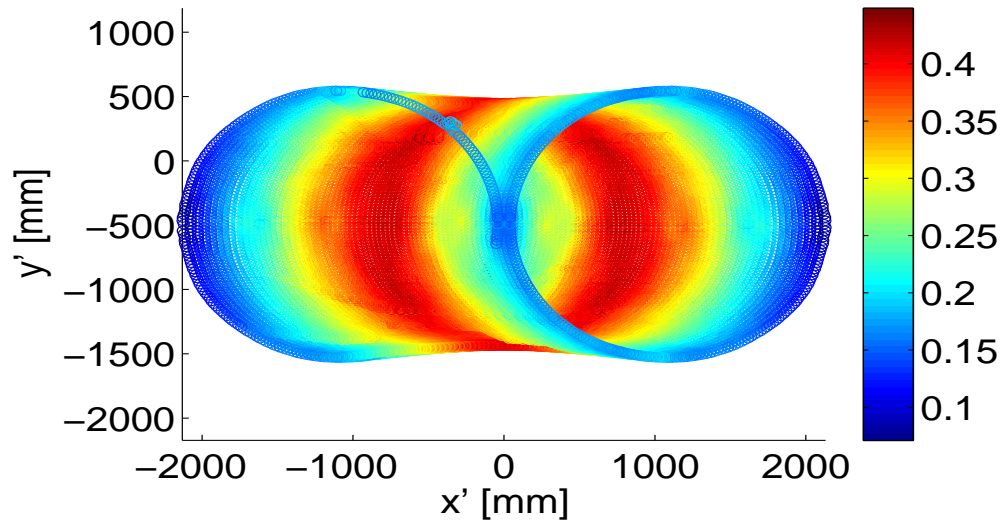
(a)
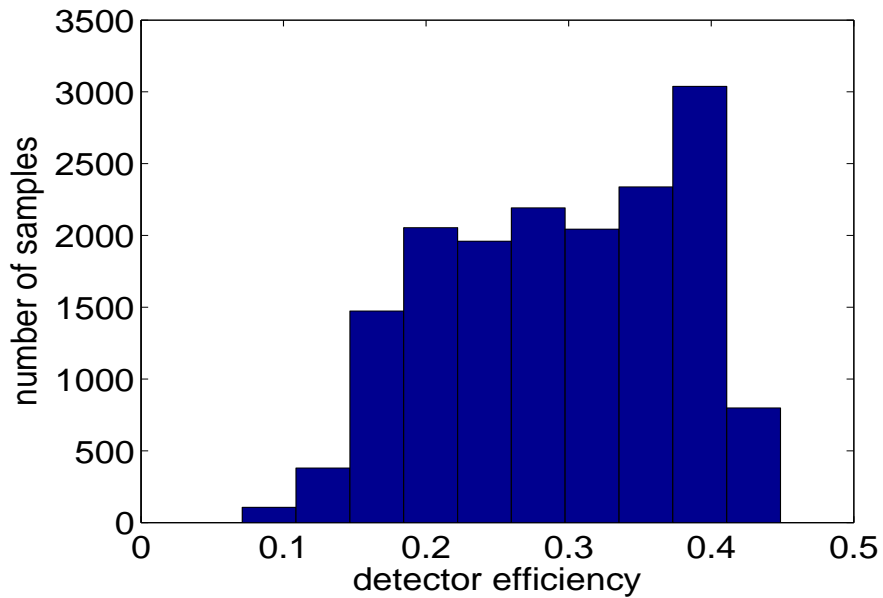
(b)

Figure 5.12: Field of view of the conical scanning imaging system using 64 detectors at 256 scan angles. (a) Distribution of efficiencies on the target plane, (b) Histogram of the overall optical efficiencies for the 16,000 samples in the image.

tions of the imaging system; and a comprehensive discussion related to the pixel size vs. frequency for the specific optics design is given in [7]. The geometric spotsize is

determined by the specific frequency between 0.2-1.4 THz. In this case, for frequencies greater than 750 GHz and a nominal 8 m range are the contributors for the estimates in Fig. 5.13 of approximately 5 mm. The average value for the spotsize in the histogram of Fig. 5.13(b) is closer to the diffraction-limited spotsize of 6 mm, when using a flat reflector.

The goal of the synthetic image experiments presented in this section is to evaluate whether the interpolation and the filtering can be used to dynamically calibrate the conical scanning system in real time once the system is functional. The algorithm should correct for the non-uniformities by compensating for the estimated variations. This is done by dynamically creating a flat field (white scene) that is used to remove the detector variations. An example of how the interpolation algorithm is used to generate a full flat-field scene where the non-uniformities are removed is shown in Figs. 5.14 and 5.15 for two cases: all equal detectors Figs. 5.14 and Fig. 5.15 detectors with a Gaussian distributed responsivities.

The real practicality and performance of the algorithm will be assessed when real conical scanned images are obtained from the imaging system currently under development at NIST. However, based on the performance of the synthetically generated checkerboard scenes, it is expected that two-dimensional spatial interpolation of the samples (i,j) and contrast enhancement will be able to reconstruct the physical sampled scene in (x,y) with high visual quality already demonstrated for the 8-element row scanned array.
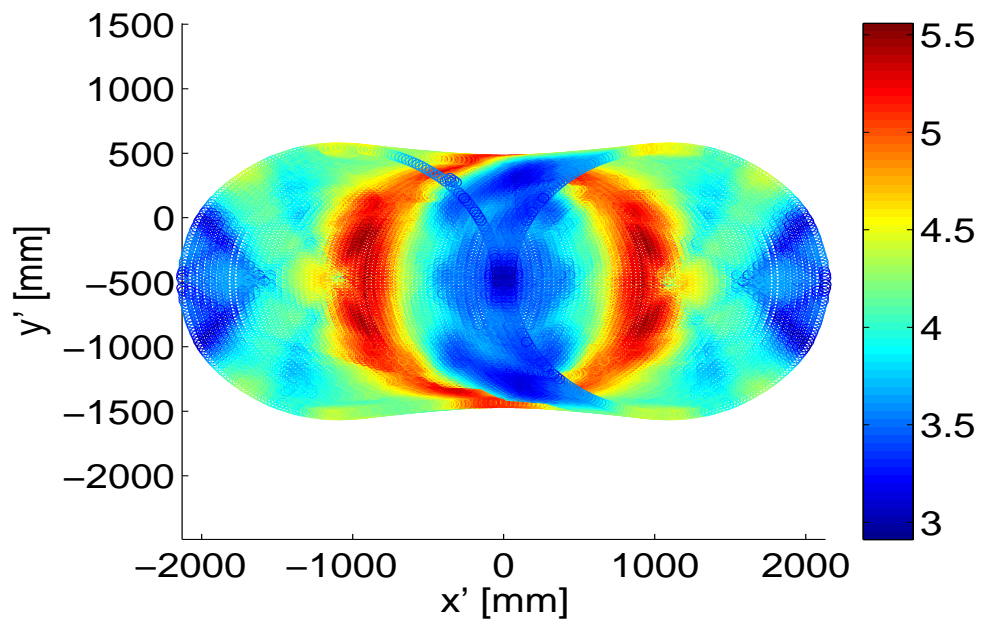
(a)
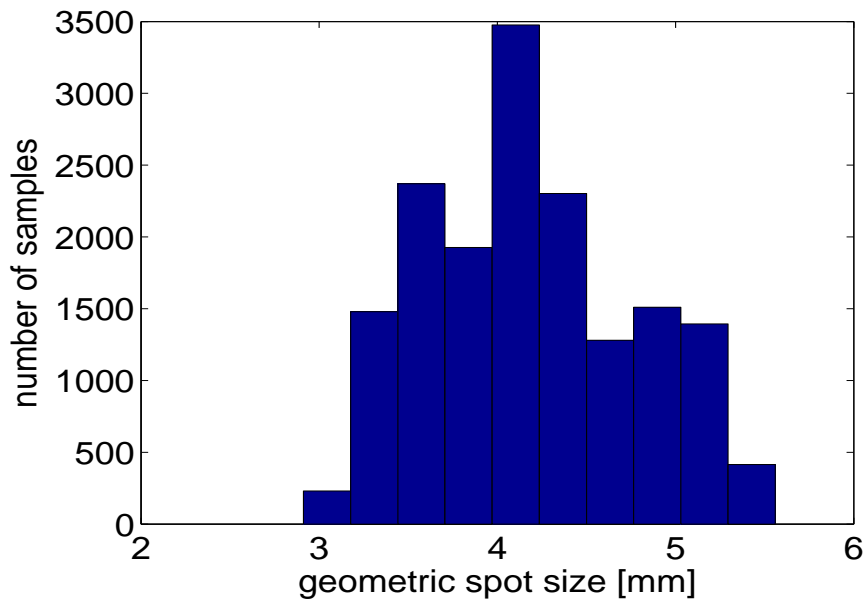
(b)

Figure 5.13: (a) Geometric spotsize distribution in the target plane the imaging system using a Schmidt telescope design using a flat reflector. (b) Histogram of the average geometric spotsize for this design, approximately 4.2 mm.
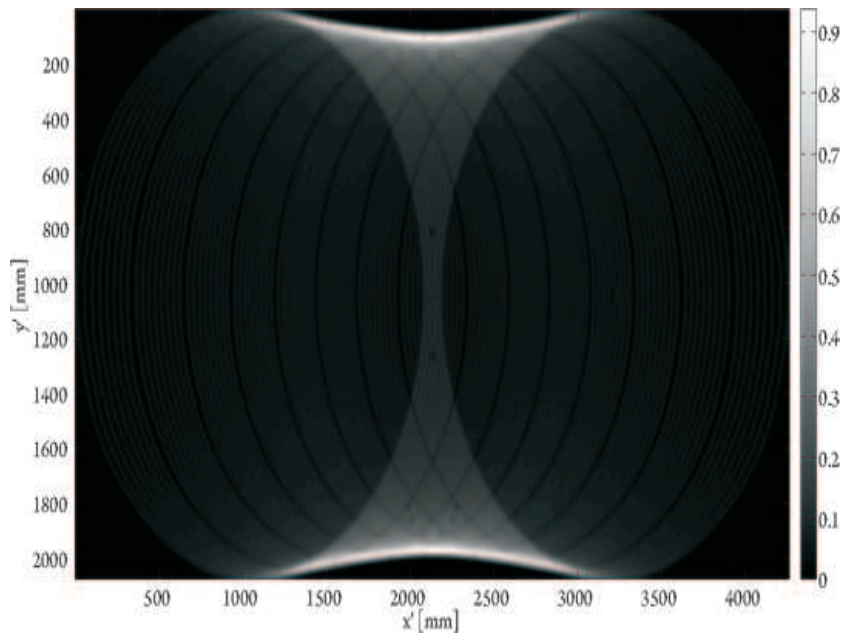
(a)
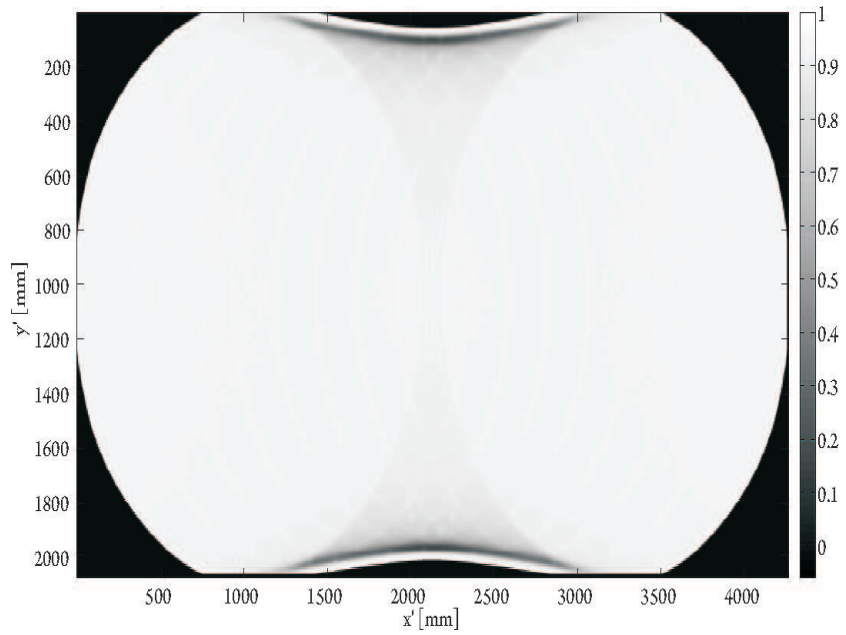
(b)

Figure 5.14: (a)Upsampled image from original scene corrupted with uniformly distributed variations in the detector array, and (b) reconstructed purely white synthetic scene. In this case, uniform detector variabilities were assumed and a Gaussian two-dimensional interpolation was used with window of length $L = 128$ and width of $\sigma = 5$.
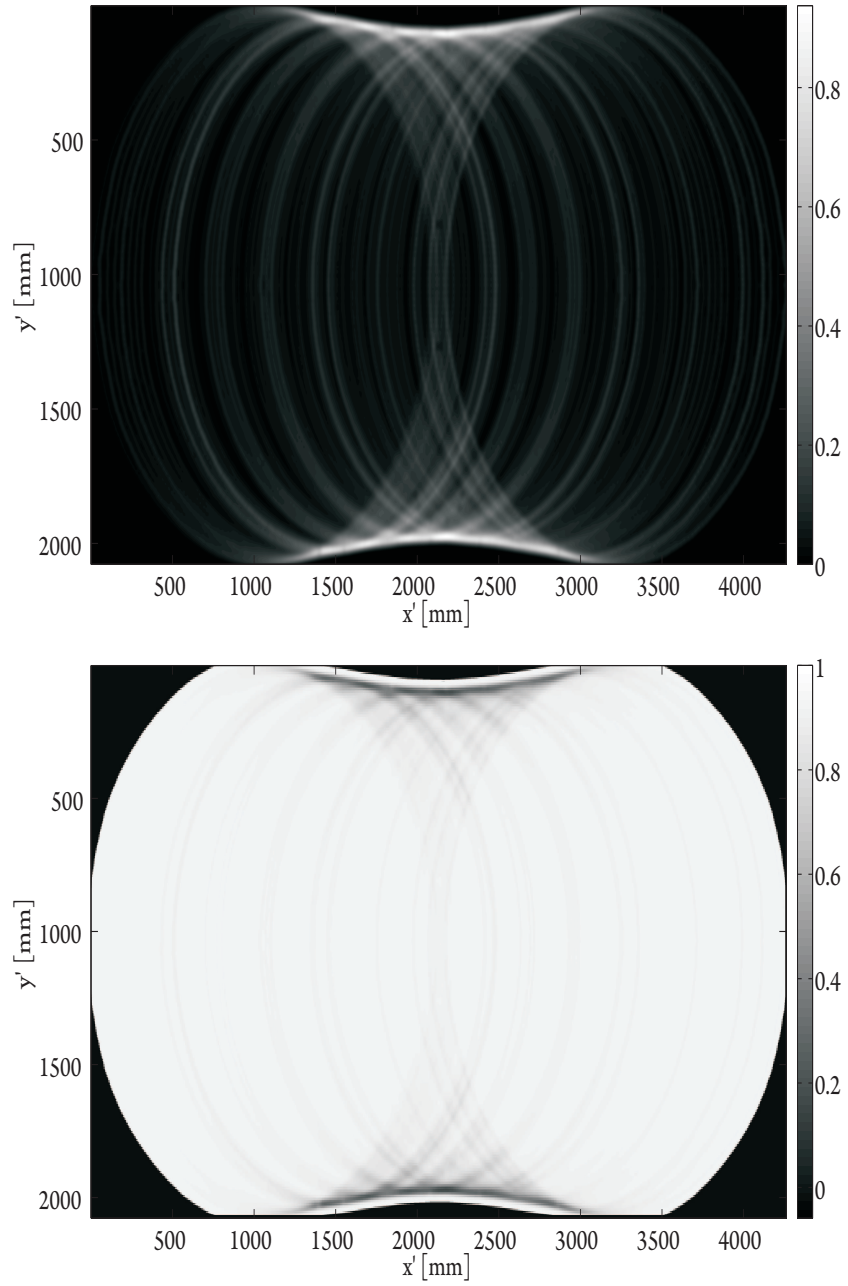
Figure 5.15: (a) Upsampled image from original scene corrupted with Gaussian non-uniformities in the detector array, and (b) reconstructed purely white synthetic scene. In this case, Gaussian distributed detector $\approx \mathcal{G}(0, 0.1)$ variabilities were assumed and a Gaussian two-dimensional interpolation was used with window of length $L = 128$ and width of $\sigma = 5$.

The next step is to test the performance of the algorithm which can be used to flat field the images on a physical scene of $4\,\text{m}\,\text{x}\,2\,\text{m}$. The flat fielding of the image consists on equalizing the detector gains. If two detectors pass through the same scene point (x,y), the received signal should be equal on both detectors. If the measurements are different, an optimization algorithm based on minimizing the difference between the measured values at detector i and detector j. The (x,y,z) positions determined by the simulation are used as coordinates in a new space (x',y',z'). The 3-D space of the optical simulation is projected into a 2-D space by using a perspective projection mapping onto an image plane. In the image plane a point in (x',y',z') becomes an index position (i,j) in a synthetic optical image covering a physical space of $4\,\text{m}\,\text{x}\,2\,\text{m}$. A standard checkerboard algorithm calibration image is used for the purpose of evaluating the sampling of the conical scanning system on the FOV. Fig. 5.16 show the checkerboard pattern image of dimensions 4000×2000 pixels, where each pixel represents a millimeter on the grid shown in Fig.5.11. The squares are either completely black or completely white.
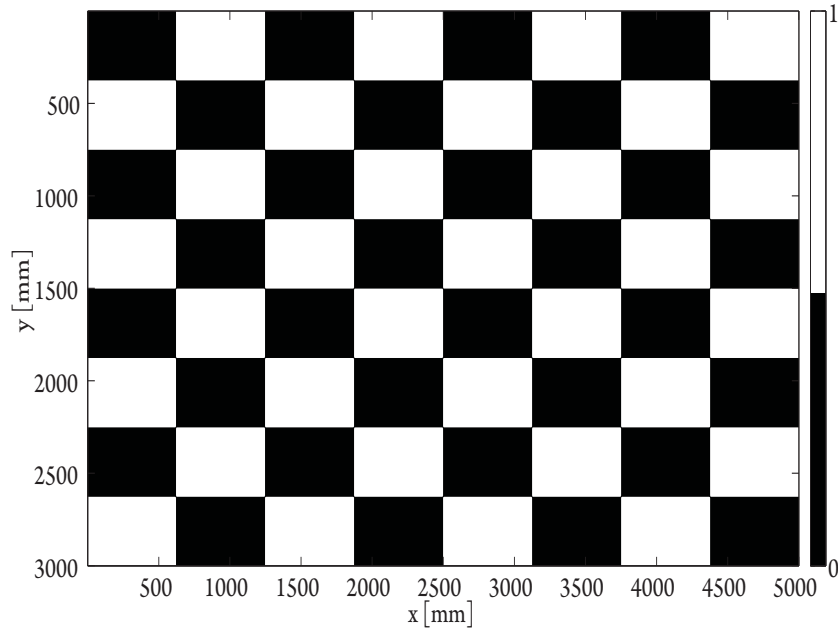
Figure 5.16: Standard checkerboard calibration image used for the purpose of evaluating the sampling of the conical scanning system on the FOV. The pattern image has dimensions 4000×2000 pixels.

Once the synthetic image is sampled, the goal is to now reconstruct the original full scene given that only 16,000 pixels were obtained. The pixels sampled at index positions (i,j) along projected image (x',y') are shown in Fig. 5.17. By using several image and signal processing techniques such as two-dimensional interpolation and filtering, the synthetic checkerboard pattern can be reconstructed. The interpolation is based on several variations of Gaussian and Chebyshev windows, changing length of the windows measured in pixels and standard deviation (Gaussian). These parameters are chosen accordingly for optimal visual quality and reconstruction of the scene. In this case the Gaussian window given by $h_g(x', y') = \exp^{-}(x' - y')^2/2\sigma^2$. The x' and y' are variables for the pixel dimensions and σ is the standard deviation of the Gaussian window. For the specific example shown in Fig. 5.18 the length of the window is $L = 128$. The window is a high order (> 10) Chebyshev polynomial window with sidelobe attenuation of $60\,$dB. Note how the squares are visually reconstructed, the image contrast is improved and the streaking is eliminated. The contrast enhancement used is the same used for the row-based linear array images. Notice that bright regions seen at the top and bottom edges between (1500,3000) millimeters are completely white and are an artifact of the sampling. Fig. 5.18 are now completely white. This is achieved by using histogram equalization and stretching, as described in Sec. 5.1. By varying the window type, length, and width parameter, the sampled image can be reconstructed accordingly.
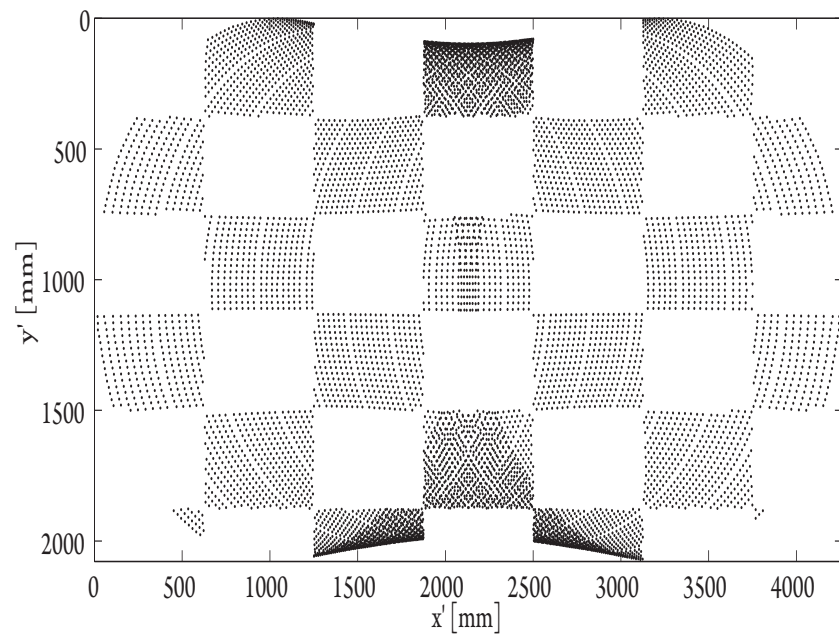
Figure 5.17: The pixels sampled at index position (i,j) are shown
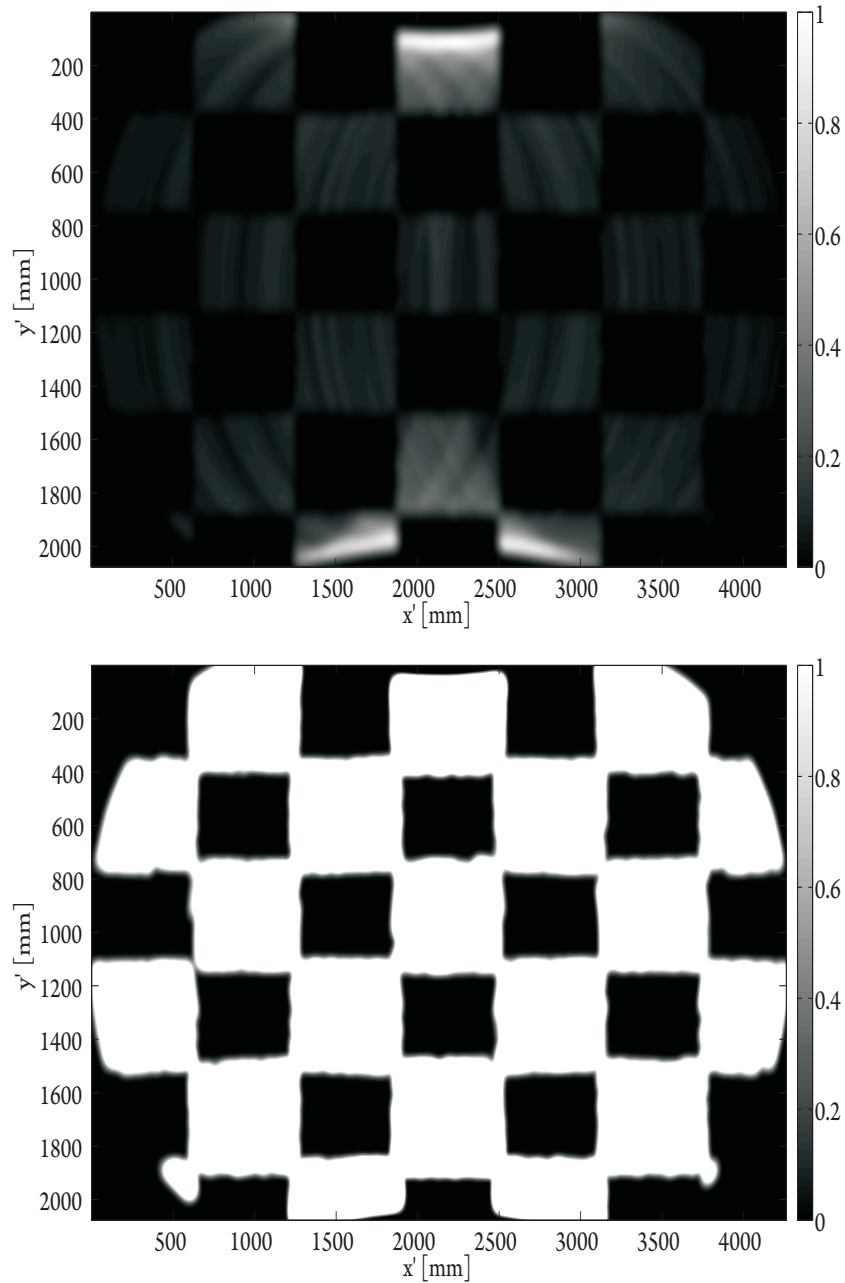
Figure 5.18: Image reconstructed from the 4000 mm x 2000 mm scene using two-dimensional 10th order Chebyshev window of length $L = 128$ with sidelobe attenuation of 60dB. Only 16,000 pixels were sampled from the original image. The black corners are areas where the conical scanner did not sample. Additional post processing was performed using contrast enhancement. The darker regions on the top and bottom of the image are removed in this case when compared to the Gaussian window reconstruction.

In each of the previous images, the detector non-uniformities have not been mentioned. This is based on the assumption that each of the detectors will have an uniform

response and that each will have the exact same behavior across the FOV. Based on the knowledge of the row-based linear array system, it is safe to say that this assumption is not realistic. Hence, an experiment assuming non-uniform behavior on the detectors was performed. In this case, the detectors are assumed to have an extreme binomial distribution behavior. This implies that some detectors will be completely non-functional while others will detect 100% of the received signal. Fig.5.19 depicts the scenario where 50% of the detectors are non-functional. On Fig.5.20 it is seen how the reconstruction algorithm is able to recover parts of the checkerboard pattern but some of the streaks remain on the scene. However, the areas that were originally sampled by the functional detectors are able to be reconstructed removing the induced conical streaks by filtering and spatial interpolation.
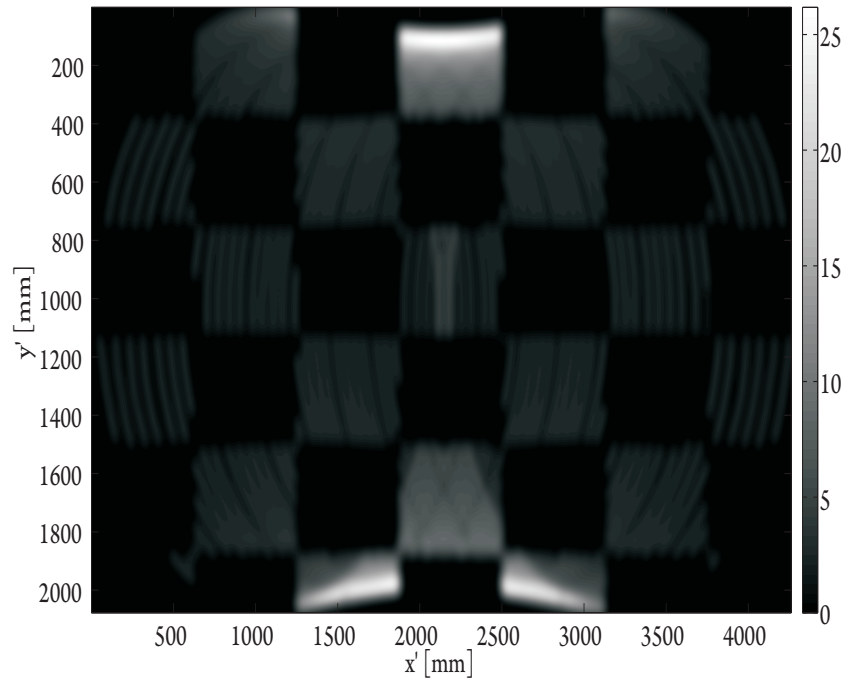
Figure 5.19: A sampled scene with detector response given as a binomial distribution. Every other detector is non-functional, implying that some detectors will not detect a signal while others will detect 100% of the received signal.

In summary, this chapter presented results of image processing applied to images from a linear array of millimeter wave antenna coupled detectors. It was demonstrated for row-scanning that the SNR improved as much 18% when images where processing
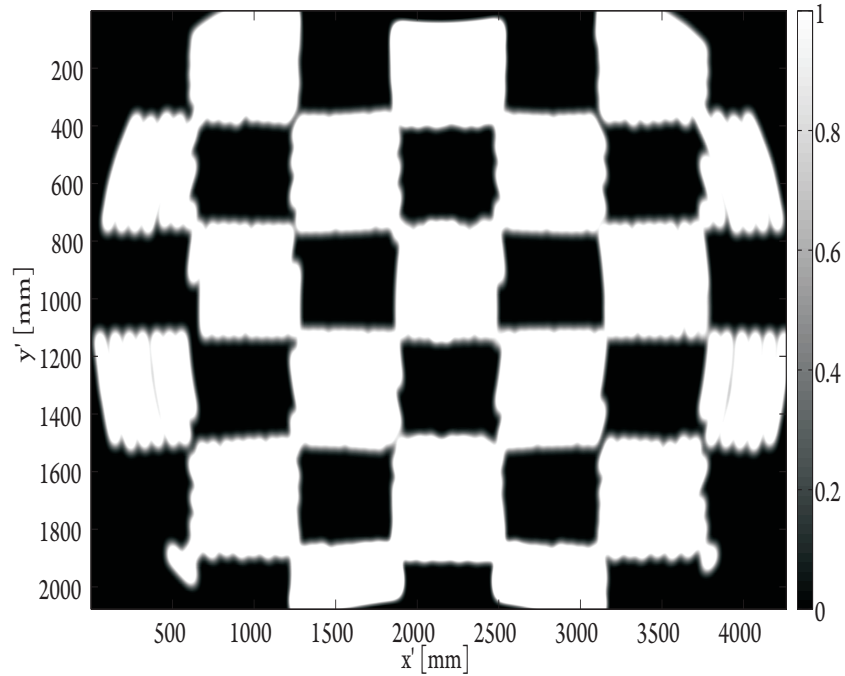
Figure 5.20: Reconstructed image using the extreme case of detectors following a binomial distribution, having 50% of the array completely non-functional

using streak removal, 2-dimensional interpolation, filtering and contrast enhancement. A major non-ideality in the imaging system is the extreme non-uniformity of the individual elements of the array, and this was taken care in the processing by thresholding resulting higher visual quality images. It was also shown that the processing allows for feature extraction and identification not possible in the raw images. The thresholding algorithm speed is sub-second, while the interpolation takes up to a minute and can be improved with specialized DSP. An extension to these algorithms was applied to synthetic images for a 64-element conically scanned array, taking into account efficiency of the quasi-optical system, non-uniform sampling, and geometric spotsize.

Chapter 6

Non-destructive Si chip inspection using a scanned microwave probe

Non-destructive inspection of material properties and material characterization is of particular interest to complex materials measurements and integrated circuit inspection [2, 63]. Near-field probing has been used in the past few decades for material property measurements [3, 64, 65]. In this technique, a small probe is a part of a microwave resonant circuit and by capacitively loading the probe with an unknown material in the near-field, the change in resonant frequency and Q-factor can be measured. The local properties of the unknown material can be de-embedded from the measured resonance change. This type of a system can be applied to sub-surface detection of Si CMOS chip metallization by virtue of the fact that the skin-effect at lower microwave frequencies is large compared to the top layers of a CMOS chip [66].

A prototype system was implemented at the University of Colorado by Jonathan D. Chisum, and this chapter presents the image processing applied to 2-dimensional measurements of portions of two CMOS chips by this non-destructive inspection probing system. In the near-field system discussed here, the tip-size varies from $1\,\mu$m-$15\,\mu$m with

comparable distance to the sample. The central frequency of the resonance is several hundreds megahertz to $2\,\mathrm{GHz}$. In the scans presented here, the $900\,\mathrm{MHz}$ circuit was operated at its second resonance at $1.8\,\mathrm{GHz}$, while the pixel size is on the order of $10\,\mu\mathrm{m}$ giving a spatial resolution around $\lambda/10,000$. Fig.6.1 shows a block diagram of the instrumentation with a photograph of a $15\,\mu\mathrm{m}$ tungsten tip above a sample. The probe circuit with the sharp field concentrating tip is mounted above the sample, which sits horizontally on a stack of Physik Instrumente (PI) M-11X series micro-translation stages. The micro-translation stages provide coarse xyz motion control while a PI P-611.ZS piezoelectric stage provides fine-z control. The two ports of the probe circuit are connected through low-loss, phase-stable cables to an Agilent E8364B Precision Network Analyzer (PNA). The coarse xyz motion stages are controlled through a PI C-843 motor driver controller card. The fine-z piezoelectric motion stage is controlled via a bias voltage from a function generator and a low noise amplifier. A computer triggers and records the four complex S-parameters measured by the PNA. The Agilent N9445A passive acoustic vibration isolation chamber acts as a mechanical low-pass filter with a cutoff of approximately $2\,\mathrm{Hz}$. This system records an S-parameter matrix which is used to extract the resonant frequency and Q-factor of the measurements using standard methods [67].

The PNA provides complex S-parameter data for many frequency points around the resonance. Since the Q-factor of the near scanning resonant circuit is on the order of 1000 and the capacitive loading of the probe is very small, for good measurements the probe has to be placed as close to the sample as possible and the phase noise of the system needs to be minimized. For example, for a $10\,\mu\mathrm{m}$ probe the tip needs to be maintained at $10\,\mu\mathrm{m}$ above the substrate for a scan over a millimeter to centimeter. This height control to about 1% of the probe size as well maintaining the zero of the (x,y) coordinate system is a challenge as it introduces errors in the image. Additional hardware limitations include probe tip size and its shape which determine signal strength as well as shape of the pixel and spatial resolution. The quality of the stepper motors determines the step size resolution and non-uniformity of spatial sampling. For the
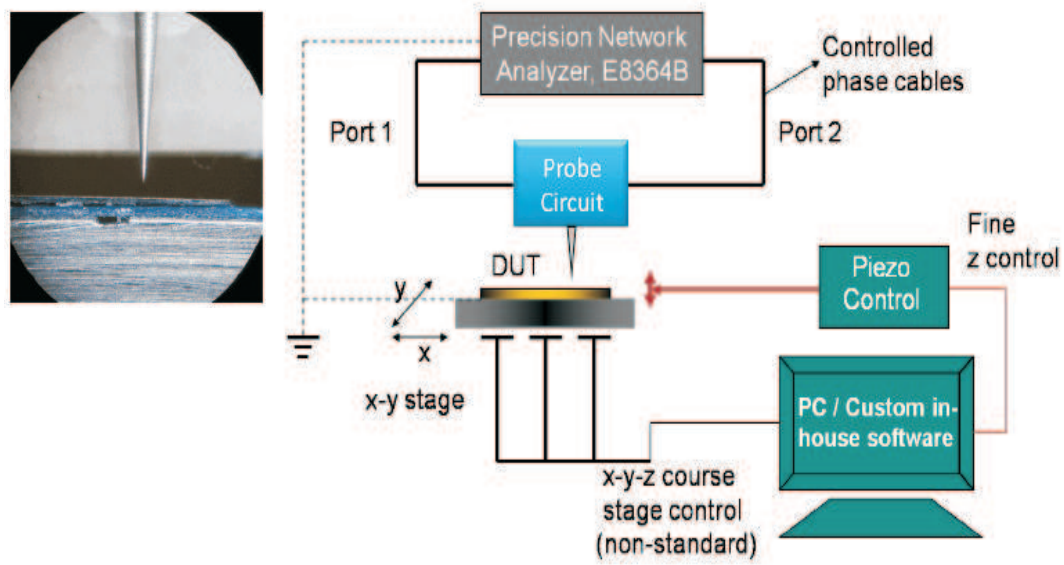
Figure 6.1: Block diagram of the motion stages, sample platform, and probing circuit for near-field microwave probing. The system is fixed in an acoustic vibration-isolation chamber and the PNA is connected to the probing circuit through phase stable, low-loss cables [66]. The photograph on the left shows a $15\,\mu$m Tungsten tip above a sample. Photo courtesy of Jonathan D. Chisum.

current instrument, the processing algorithm is as follows:

(1) The scans are upsampled according to the scan step size to make a single pixel equivalent to $1\,\mu$m. The up-sampling enables higher position accuracy for the image registration process.

(2) The two-dimensional data is registered using a cross-correlation method by selecting points from the upsampled image in known positions to correct for alignment imperfections.

(3) The upsampled and registered images are interpolated using two dimensional filters and spatial operations such as weighted average of neighboring 4x4 pixel regions. Sub-pixel features become visually identifiable after the interpolation is performed.

6.1 Processing for defect detection

Two test structures were scanned using this system and image processing was applied to enhance sub-resolution features. The first test structure is a large CMOS chips fabricated in a standard IBM process, consisting of four $400\,\mu$m squares of dense circuitry with eight metal layers. A backside image of the chip with scan area marked by the squares is captured using a broadband infrared camera and shown in Fig.6.2. The two square regions scanned are not identical on the inner metal layers. In addition, the top two metal layers contain periodic metal polygons roughly 1μm and 6μm square, used for planarization. These metal squares provide an extra shielding layer for the demonstration of metallic depth penetration. Fig. 6.2 shows the difference between the two circuits in Metal layer 4 clearly. The normalized Q-factor for the 2D scans obtained with a $15\,\mu$m diameter tip, $5\,\mu$m above the sample surface.
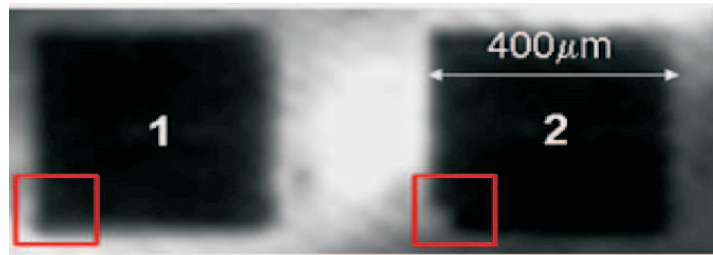
(a)
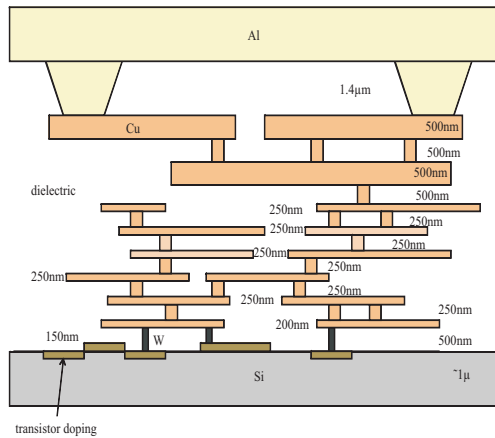
(b)

Figure 6.2: (a) A broadband incandescent IR source was used to illuminate the chip from the back-side, and a broadband IR camera was used, with a lens, to record the image of two $400\,\mu$m square circuit regions of a large CMOS chip fabricated in a standard IBM process. The square indicates the scan area and the difference between the two circuits in Metal layer 4 are clearly visible (IR image courtesy of Prof. Dana Anderson, JILA), (b) cross-section and dimensions of dense circuitry with eight metal layers in CMOS chip.

The two test structures shown in Fig. 6.2(a) were processed to characterize the repeatability of the measurements and the ability of discriminating between different CMOS chips. The repeatability of the system was examined by calculating global statistics resulting from the two 2D scans and samples at each point taken 5 times.

For the case of discrimination between chips, the same sampling followed by the repeatability study was used , and the global statistics of the 2D scans were estimated. The resulting global standard deviation of two scans taken from the same chip is presented in Fig. 6.3.

In addition, the values from the two 2D scans were compared by using image substraction on a pixel-by-pixel basis. For simplicity, each test structure will be referred to as $C_{k,n}$, where $k = 1, 2$ is the circuit number, and $n = 1, 2$ is the scan number. The Q-factor 2D scans at $1.8\,\mathrm{GHz}$ obtained with a $15\,\mu\mathrm{m}$ diameter tip at $5\,\mu\mathrm{m}$ above the sample surface are shown in Fig. 6.4.

For processing and feature enhancement, each scan was normalized using its respective spatial-global maximum. The normalization factors are shown in Tables 6.1 and 6.2. The images are upsampled, registered and interpolated, following the processing algorithm described in Sec. 6.
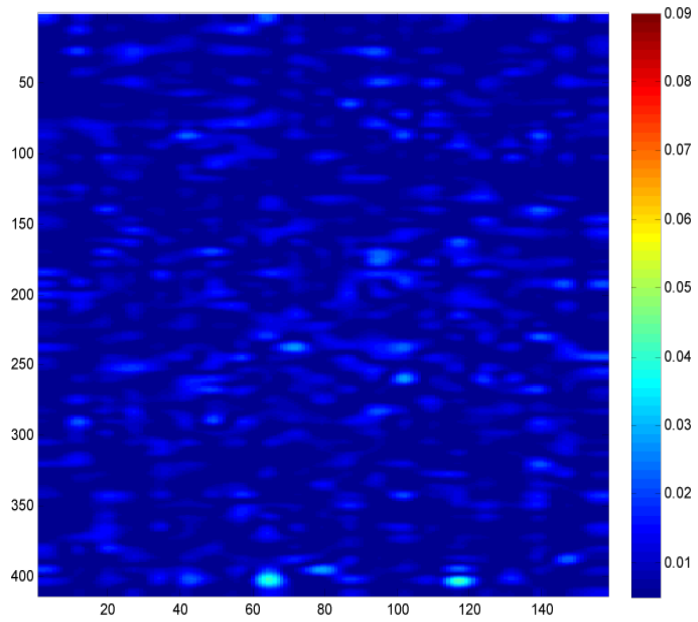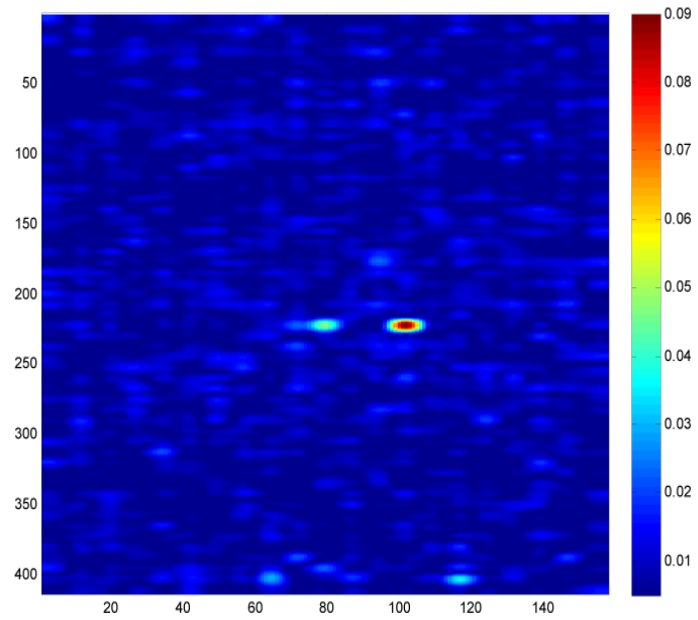
Figure 6.3: Standard deviations estimates of two scans of same CMOS chip taking each point at position (i,j) 5 times. The measurements used a 15μm diameter probe tip and 5μm above the sample surface. The probe footprint and pixel size is approximately equal to $15\,\mu$m.
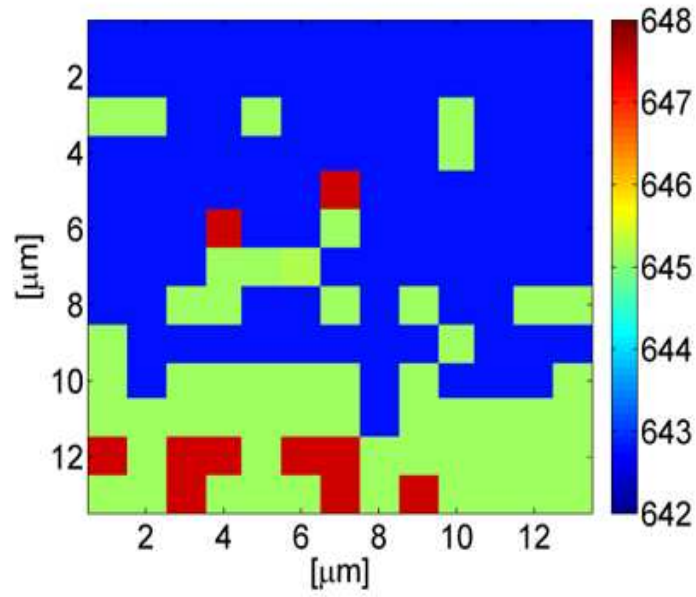
(a)
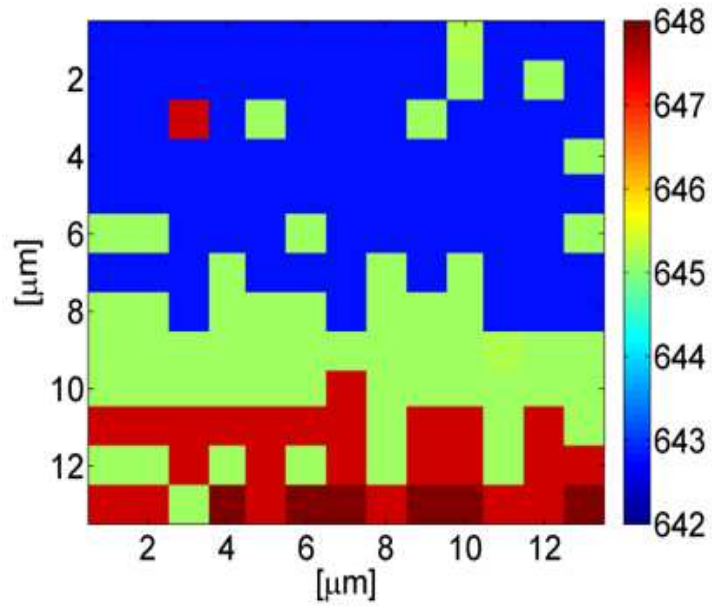
(b)

Figure 6.4: Q-factor from raw two-dimensional scans of CMOS circuits using a 15μm diameter probe tip and 5μm above the sample surface. The probe footprint and pixel size is approximately equal to $15\,\mu$m.
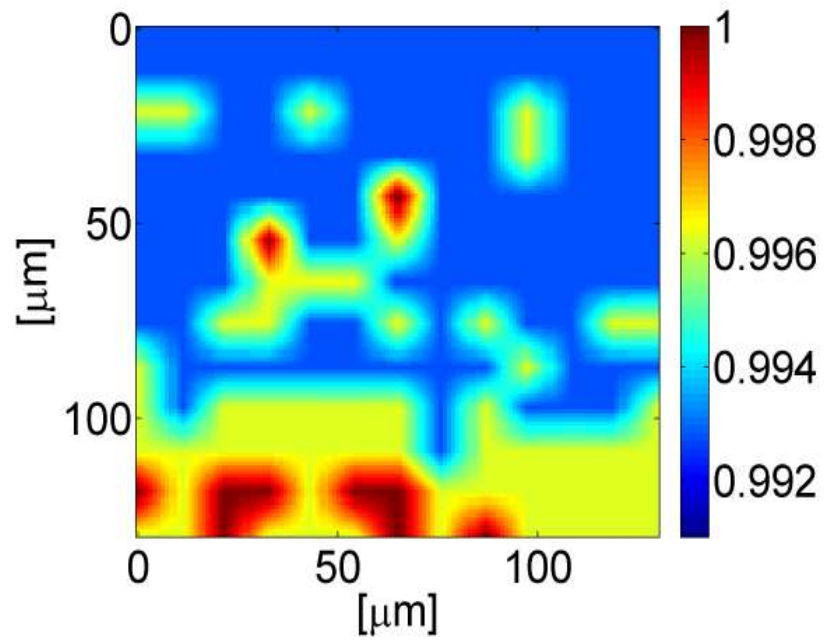
(a)
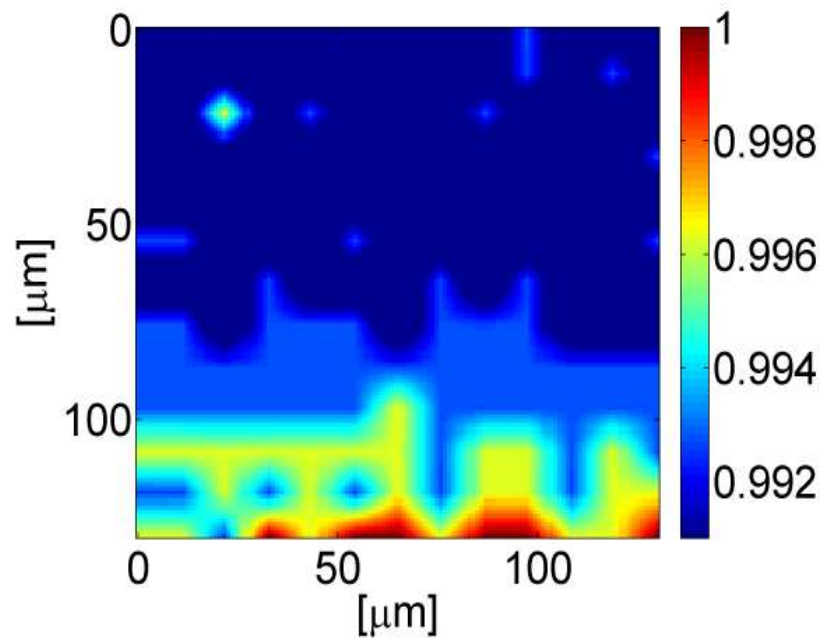
(b)

Figure 6.5: Upsampled and interpolated images of measured Q-factor two-dimensional scans using a 15μm diameter probe tip and 5μm above the sample surface. The probe footprint and pixel size is approximately equal to $15\,\mu$m.

Repeatability

The repeatability of the system was studied by performing a pixel-based image sub-straction on pairs of 2D scans and identify local differences. A description of the pixel-by-pixel image substraction algorithm is shown in Fig. 6.6. Notice that this technique, assumes a perfect registration between the two samples being subtracted, making image registration and alignment precision in the system an additional source of errors. In the ideal case, for perfect registration, perfect alignment of chips on mount will have a value equal to 0, a black pixel which represents both values are identical. A resulting value of 1, a white pixel, indicates complete difference between the two points.

Figure 6.6: Absolute difference in images (2D data) can be obtained by subtracting the data from each scan on a pixel by pixel basis. $X_{i,j}$ and $Y_{i,j}$ are matrices of pixels in positions (i,j) containing the measurements obtained from the probing system. In the ideal case, for perfect registration, perfect alignment of chips on mount will have value of 0, a black pixel, representing both values are identical. A value of 1, a white pixel, representing complete difference between two points.

The results of the image substraction between $C_{2,1}$ and $C_{2,2}$ are presented in Fig. 6.7. The abundance of dark values in the difference image indicates that the two scans are similar and the measurements correspond to the same test structure. This observation is validated by calculating the global statistics of the two scans of circuit 2. Table 6.1 shows that the varibiality of the measurements from one scan to the next is around 1%.
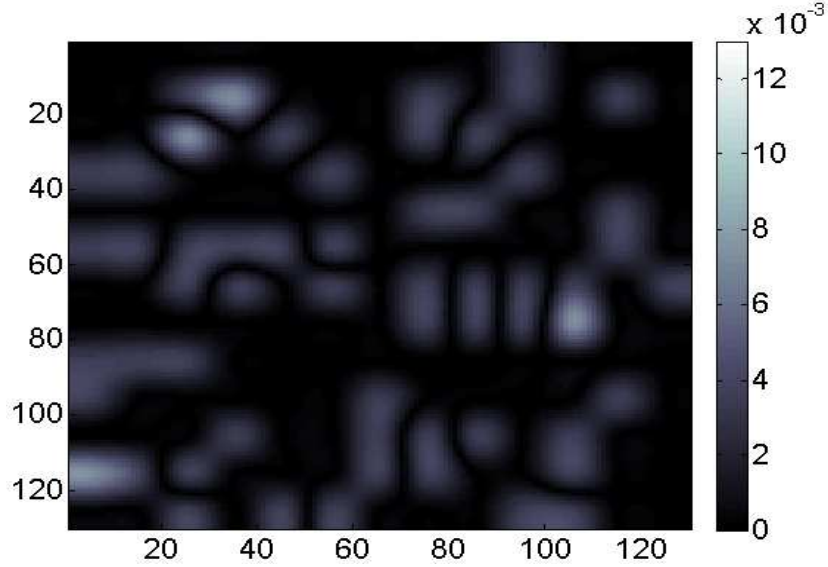
Figure 6.7: An example of image substraction between scans from $C_{2,1}$ and $C_{2,1}$. After the 2D data was registered using cross-correlation, to account for alignment imperfections, a pixel-based image substraction was performed on pairs of 2D scans to identify local differences. Pixel-based image substraction between $C_{2,1}$ and $C_{2,2}$ to detect differences on chips under several metallization layers.

Table 6.1: Global statistics of CMOS chips scanned using a $15\,\mu$m tip. Two scans were taken for each circuit. Shown here are the results of comparing Circuit 2, Scan 1 and 2 to study repeatability of the scanning system.

	$C_{2,1}$	$C_{2,2}$
Normalization factor	650.48	650.50
Global average	644.72	644.53
Global standard deviation	1.91	1.87
Global minimum	650.48	650.50
Global maximum	642.18	642.44

Discrimination

To analyze the ability of the system to measure differences in chips, the same registration and upsampling techniques were used. In this case, the image substraction indicates areas of local change where $C_{1,1}$ and $C_{2,2}$ are different. The global statistics for the scans of circuit 1 and 2 are shown in Table 6.2.

In summary, the probing system is able to measure consistently between same samples and discriminate different ones. However, it is with the help of image processing that spatial information, and sub-feature enhnacement is achieved.

Table 6.2: Global statistics of CMOS chips scanned using a $15\,\mu$m tip. Two scans were taken for each circuit. Shown here are the results of comparing Circuit 1 and 2 to discriminate between them.

	$C_{1,1}$	$C_{2,2}$
Normalization factor	648.05	650.48
Global average	643.81	644.72
Global standard deviation	1.22	1.91
Global minimum	648.05	650.48
Global maximum	642.34	642.18

Ideally, for applications where automatic defect detection is needed, the image substraction algorithm in combination with thresholding can be applied. An example of a threshold that will allow for automatic identification of defects between groups of chips is shown in Fig. 6.10. In this figure, the blue and red lines correspond to the global mean along rows of the two test structure scans, resulting in a cut along the columns. The separation between these two lines are indicative of the difference on the chip that was detected by the system.
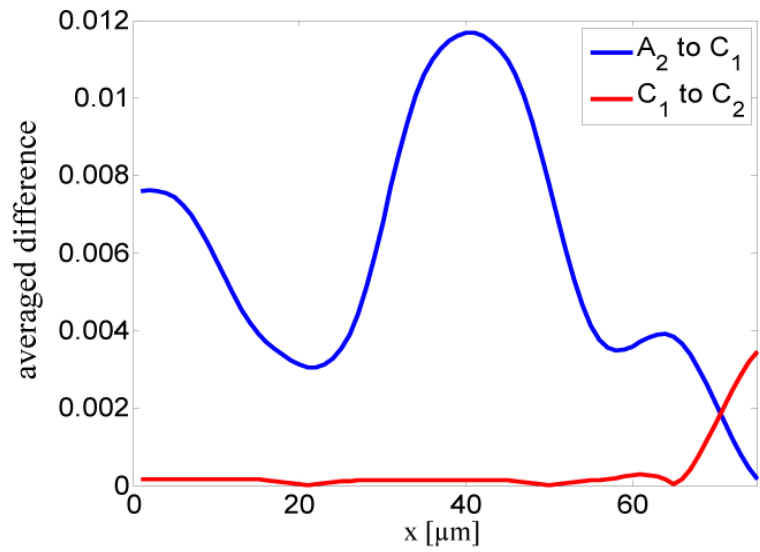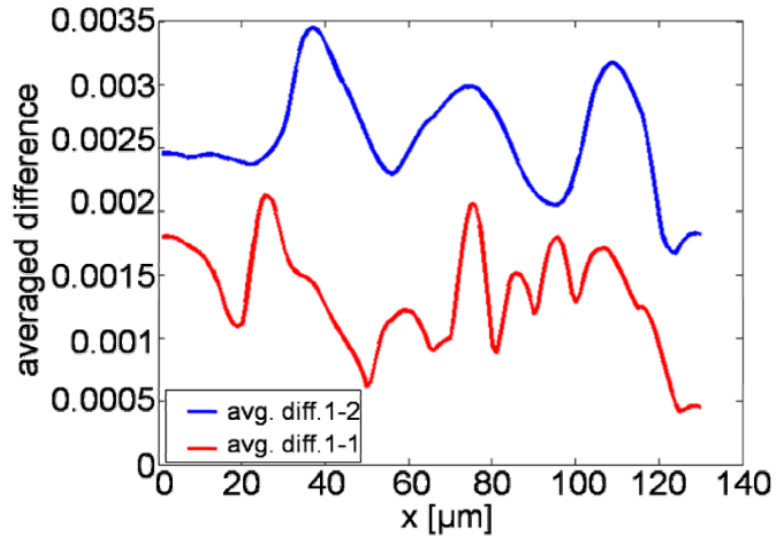
Figure 6.8: Average difference in normalized Q-factor plotted as a function of x, averaged over all pixels in the y-direction. The dashed blue line indicates the difference of normalized data between circuit 1 and 2. The solid red line shows the difference of normalized data in two scans of circuit 1.

A different CMOS chip with busses on the top metal layers was used as a third test structure with the same probe circuit, but scanned at $20\,\mu$m height. The bus lines can be seen in the optical image shown in Fig. 6.9. The processed images from the measured Q-factor and changes in resonant frequencies of the third test structures allows for discrimination of features of approximately $10\,\mu$m wide. Because of this scan height, the effective probe footprint, and thus the resolution, is approximately $20\,\mu$m. The bus feature of approximately $10\,\mu$m is visually identifiable in Fig. 6.9. The results suggest that extraction of features below the typically accepted theoretical resolution of $20\,\mu$m is possible. We are limited to the scan step size ($7.5\,\mu$m) as a possible resolution.

195μm
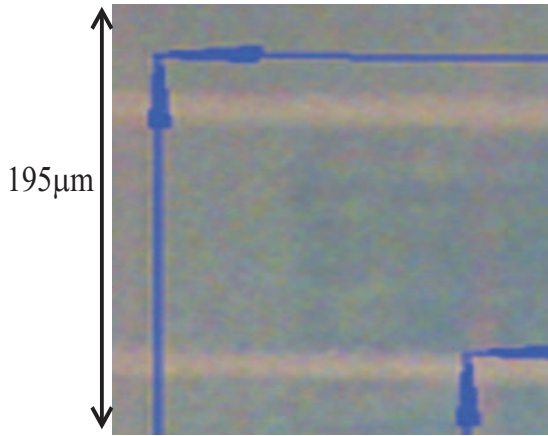
(a)

Figure 6.9: Optical image of CMOS chip with busses on the top metal layers. The bus lines can be seen in the optical image

In conclusion, image processing using upsampling, registration by cross-correlation and two dimensional spatial interpolation allowed for enhancement of the visual quality of the scans and also sub-surface detection of small features in the data. The repeatability and discrimination capabilities of the measurements by the systems were also studied, and local spatial differences between chips were identified by using pixel-by-pixel image subtraction.
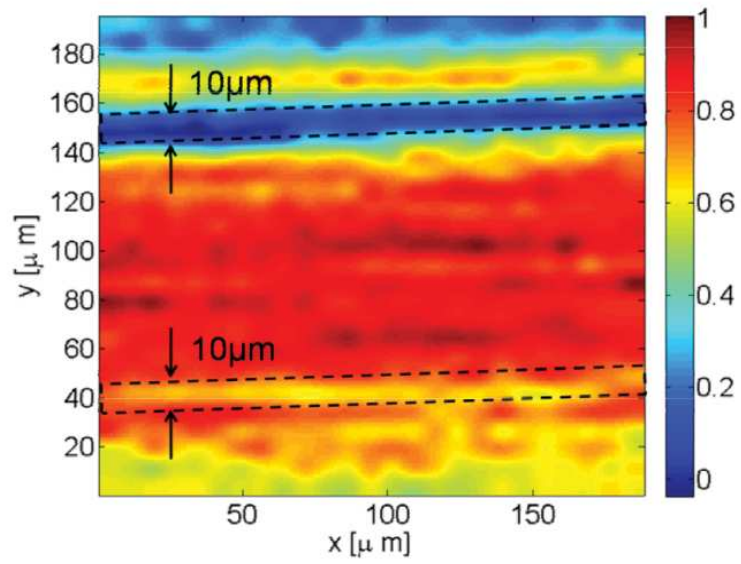
(a)
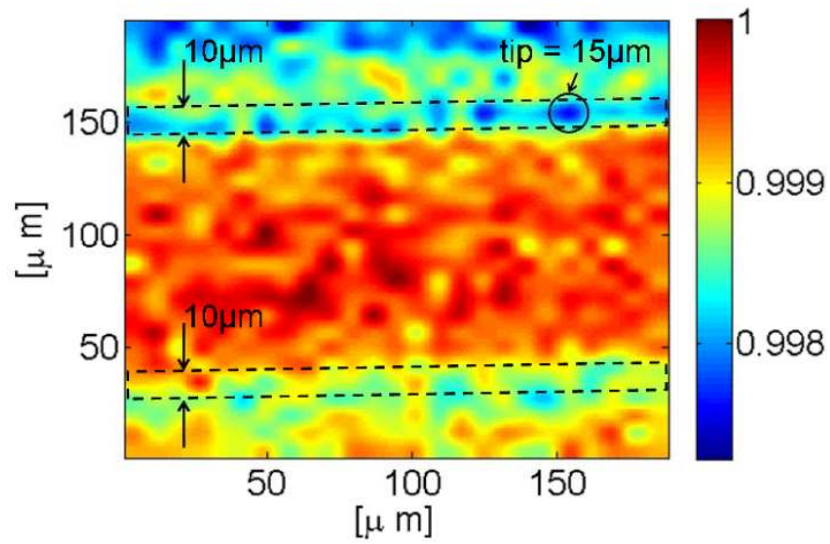
(b)

Figure 6.10: Average difference in normalized Q-factor plotted as a function of x, averaged over all pixels in the y-direction. The dashed blue line indicates the difference of normalized data between circuit 1 and 2. The solid red line shows the difference of normalized data in two scans of circuit 1.

Appendix A

Nonlinear Classification and Epileptic Seizure Detection on Acute Rat Model

A.1 Introduction

The scalp electroencephalogram (EEG) is a powerful tool for neurophysiology in 1929, when Hans Berger first published his study on the electrical activity of the human brain. Berger observed the presence of different frequency rhythms during wakefulness and alertness, comparing them in normal and injured brains [68]. Since then, the EEG has been commonly applied to the study epilepsy. Modern EEG systems can use up to 128 electrodes to sample and record the time domain electrical activity of the brain [1]. The signals from the electrodes are mixtures of neural signals of interest and thus, some signal processing needs to be applied in order to separate them. Usually, the EEG recordings are assumed to be a linear combination of the real signals implying that linear separation methods such as Principal Component Analysis (PCA) can be applied. One of the goals of this thesis is to explore whether nonlinear methods are better suited for this type of analysis. Additional processing is needed to remove artifacts such as those caused by muscle movements.

Historically, the detection of epileptic seizures by clinicians has been based on the visual inspection of the EEG recordings. Studies have shown that epileptic seizures give rise to changes in certain frequencies bands of the Fourier Transform from the measured signals [1]. For example [69, 70] focused on the analysis of the $\theta\,(3.5\text{-}7.5\,\text{Hz})$ and the $\alpha\,(7.5\text{-}12.5\,\text{Hz})$ rhythms, and their relationship to epilepsy. Time-frequency methods, such as the Gabor and wavelet transforms are used to detect the onset of seizures. Subsequently, nonlinear dynamic techniques showed that a reduction in the dimensionality of the data might indicate an epileptic seizure (ictal state) [71, 72]. This decrease in dimensionality may be due to synchronization between the neurons during a seizure.

Currently, there are various techniques for reducing the dimensionality of data, such as the widely known Principal Component Analysis (PCA) [56]. The linear subspace created by this technique is obtained by finding the first eigen-components on the data where the variance is maximized. Being a linear technique it is not able to separate optimally signals from nonlinear combinations. Further higher order statistical techniques such as the Independent Component Analysis (ICA) assumes statistical independence of each of the signal mixture components. The dimensionality reduction method presented here is nonlinear and attempts to reconstruct the underlying structure of the dataset without *a priori* statistical assumptions of the signal mixtures.

Several nonlinear techniques have been recently developed to deal with these limitations and have focused on building lower dimensional representation of datasets by taking into account the nonlinearities of the data under study. These techniques assume that the samples can be described by a smooth manifold with an existing underlying structure. The lower dimensional manifolds reconstructed by these techniques include information on neighboring points. Examples of nonlinear approaches are Laplacian Eigenmaps [10, 73], and Local Linear Embedding [74, 75].

In this work, the underlying structure of the EEG recordings to detect epileptic seizures is examined. Consider a D dimensional vector $X[n]$ consisting of the measured output of the D electrodes as a function of time as shown in Fig. A.1. Since the number
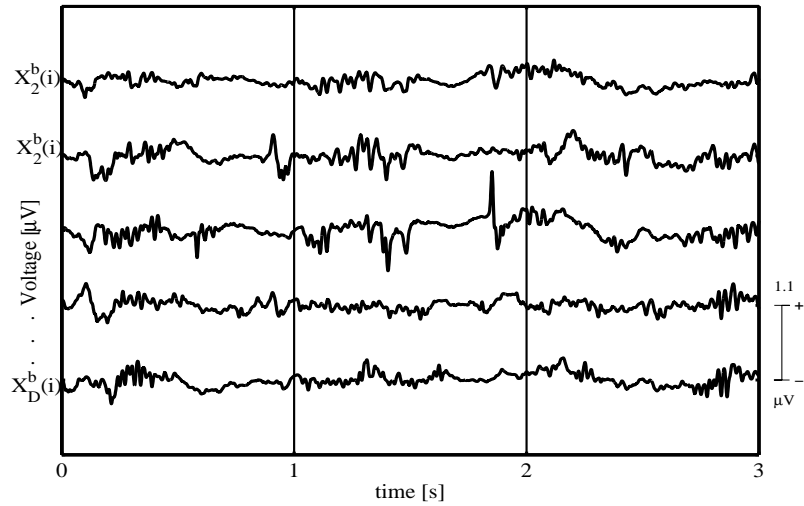
(a)
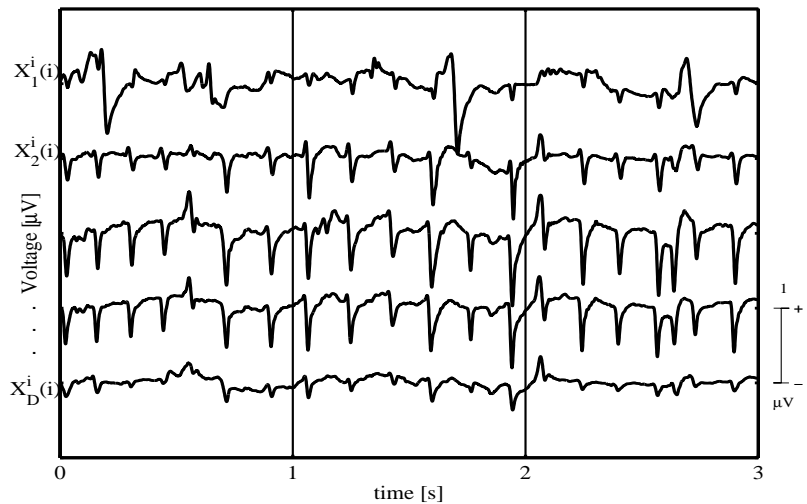
(b)

Figure A.1: Set of normal and epileptic EEG recordings. Each recorded signal corresponds to the sampled measurements from one scalp electrode as a function of time, (a) A set of EEG sampled measurements from a normal brain EEG as a function of time. This figure shows an example of a brain on a baseline (normal) state, (b) A set of EEG sampled measurements from an epileptic brain as a function of time. Each of the measured signals correspond to an electrode placed on the scalp. This figure shows an example of a brain on an ictal (seizure) state.

of electrodes is on the order of 64 to 128, classification in such a high dimensional space requires a very large number of training samples [76]. Due to the physical processes

in the brain, the D signals are not orthogonal and the intrinsic dimensionality of the EEG recording is probably lower than D. In this work, it is assumed that the sampled measurements $X[n], n = 1, 2, ..., N$ lie on a smooth manifold of dimensionality $d \ll D$. Each point on this manifold represents a measurement of the D-dimensional vector $X[n]$. Reasonably, EEG recordings associated with seizure (ictal) and normal states (baseline) are expected to lie in different regions of the manifold. The experiments presented here validate this hypothesis. The goal of this work is to reconstruct the underlying manifold and use it to train an algorithm using a kernel ridge classifier in order to detect epileptic seizures with high probability of classification.

The following sections describe the approach, methodology and results of this work. Section A.2 contains a general overview of the mechanisms used to perform the EEG analysis and classification. Section A.2.1 describes the methodology for reconstructing the EEG manifold and the classifier is discussed in the appendix. Some related techniques are mentioned in A.3. The experiments and conclusions are presented in A.4 and A.5, respectively.

A.2   General overview

The main problem addressed in this work is the classification of a EEG recording $X[n]$ at a given sample n into one of the two classes: (1) ictal or (2) baseline. The goal is to train a classifier using time samples extracted from ictal, $\mathbf{X}^i = [X^i(1)|...|X^i(N)]$, and baseline states $\mathbf{X}^b = [X^b(1)|...|X^b(N)]$. In this work, the Laplacian eigenmap method is used [10] to reconstruct the underlying manifold from the training samples $\mathbf{X}^b$ and $\mathbf{X}^i$. Following the reconstruction of the manifold, the samples are projected into a lower dimensional subspace, with dimensionality $d \ll D$. Therefore, better classification performance with the same number of training samples is expected if classification is performed directly on the reconstructed manifold [77].

A.2.1 Reconstruction of the EEG manifold

Since we do not have access to a representation of the EEG manifold, we can use the samples to approximate it. A good initial approximation to the unknown geometry of the manifold can be achieved by building a graph. An example of an adjacency graph is shown in Fig. A.2. In this figure, each of the nodes represent a D-dimensional vector containing the sampled EEG at an instant in time. Each point is either connected or not; depending on a computed adjacency matrix, $A_{n,m}$ with weights $W_{n,m}$. Common
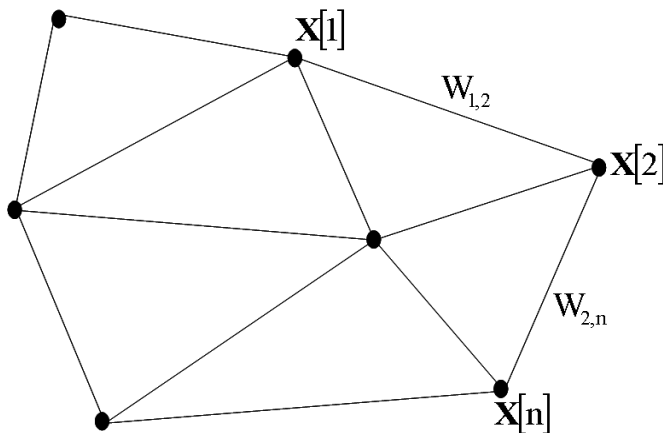
Figure A.2: Example of graph, $G = (V, E)$. Each of the nodes, V, represent a D-dimensional vector containing the sampled EEG at an instant in time. Therefore, each node represent a set of samples at different times, n. Each point is either or not connected by an edge, E, on a computed adjacency matrix, $A_{n,m}$ with weights $W_{n,m}$. For this case, $W_{n,m}$ is obtained by computing the k-nearest neighbors. Once, these weight values are computed, the graph, G is formed.

ways to compute these weight values and construct the graph is by selecting k-nearest neighbors or by defining an ε-neighborhood [10]. The former was chosen for this work. In this case, the vertices of the graph are sample points, $X[n]$ formed by the columns of $\mathbf{X}$. The edges define the proximity of samples on the underlying manifold. We connect vertices using the k-nearest neighbors approach: the nodes $X[n]$ and $X[m]$ are connected by an edge if $X[n]$ is among the k-nearest neighbors of $X[m]$. The edges on the graph can also have assigned weights, $W_{n,m}$ for neighboring points, creating a weighted adjacency graph. These weights are given by

$$W_{n,m} = \exp(-\|X[n] - X[m]\|/(2\sigma^2)). \tag{A.1}$$

The classification algorithm is shown in Fig. A.3 and the steps are as follows:

(1) Consider baseline and ictal time series $\mathbf{X}^b, \mathbf{X}^i$ of size $(D \times N)$, and construct the concatenated matrix $\mathbf{X} = [\mathbf{X}^b | \mathbf{X}^i]$ matrix;

(2) Construct adjacency matrix, A, from $\mathbf{X}$;

(3) $A_{n,m} = \begin{cases} \sum_l W_{l,m} & \text{if } l = m \\ 0 & \text{otherwise} \end{cases}$;

(4) Weights

$W_{n,m} = \exp\left(-\|X[n] - X[m]\|/2\sigma^2\right)$ where $X[n]$ and $X[m]$ are columns n,m of $\mathbf{X}$;

(5) Vertices of the graph are columns $\mathbf{X}$

(6) Edges are defined by k-nearest neighbors;

(7) Find the Laplacian matrix, L,

$L_{n,m} = A_{n,m} - W_{n,m}$

(8) Find the eigenvectors $\{\phi_1, ..., \phi_d\}$ of

$L\phi_l = \kappa_l A\phi_l$;

(9) Project the training data on the manifold using (B.5), finally;

(10) Train the kernel ridge classifier on the manifold

Once the connected graph is constructed, we compute the Laplacian, L, on the graph defined as $L = A - W$, where the adjacency matrix,

$$A_{n,m} = \begin{cases} \sum_l W_{l,m} & \text{if } n = m \\ 0 & \text{otherwise} \end{cases}.$$

The eigenvectors $\in [\phi_1, ..., \phi_D]$ are solutions to the following eigenvalue problem

$$L\phi_l = \kappa_l A\phi_l, \tag{A.2}$$
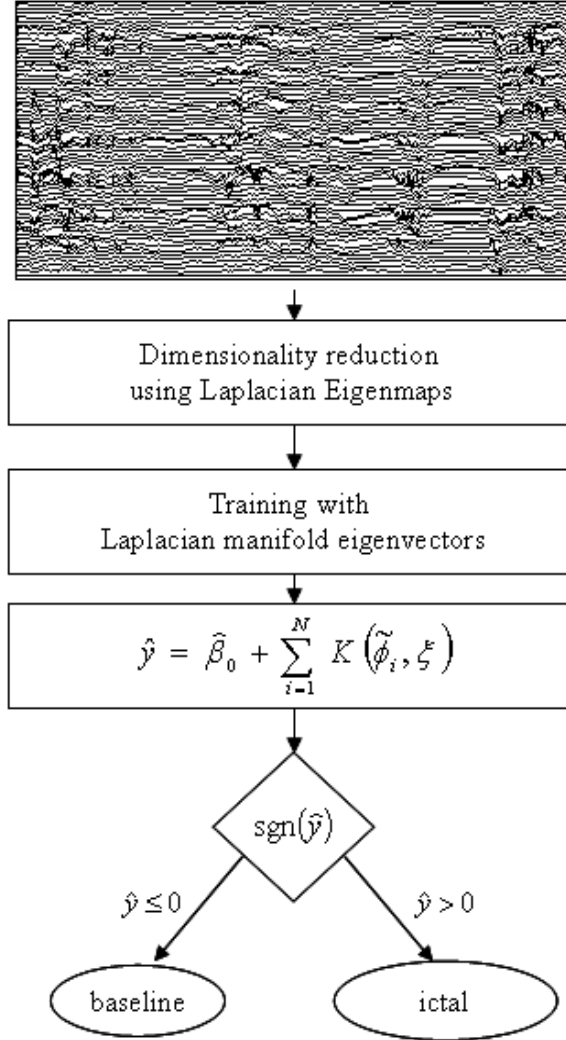
Figure A.3: Block diagram of classification algorithm. The full set of measured EEG signals are recorded from up to 128 electrodes as a function of time. The dimensionality of these sampled measurements is reduced by method of Laplacian Eigenmaps. A lower dimensional set of measurements, $d \ll D$ is used to train the algorithm. The distinction between normal or epileptic EEG measurements is performed by using a kernel ridge classifier as a discriminant function. Computing the kernel matrix is the most computationally demanding part of the algorithm.

where κ_l is the corresponding eigenvalue. As is explained in [10, 73], the eigenvectors, $\phi_1, ..., \phi_D$, provide the optimal embedding of the manifold. The mapping defined by

$$X \rightarrow \Phi(X) = [\phi_1|...|\phi_D]^T(X)$$

preserves the Euclidean distance locally by minimizing

$$\sum_{n,m} ||\phi_n - \phi_m||^2 \mathrm{W}_{n,m} = tr(\Phi^T \mathbf{L} \Phi). \tag{A.3}$$

The vector ϕ that minimizes (B.4) is provided by the lowest non-trivial eigenvalue solution of the generalized eigen-problem in (B.3). The reduction of dimensionality is achieved by defining the mapping from $\mathbb{R}^D \to \mathbb{R}^d$, where $\mathbb{R}$ is the set of real numbers, as follows

$$X(l) \to \tilde{X}(l) = \text{column } l \text{ of } \tilde{\Phi}(X) \tag{A.4}$$

$$= [\phi_1|...|\phi_d]^T(X). \tag{A.5}$$

The classification of the training data is performed by projecting $\mathbf{X}^b$ and $\mathbf{X}^i$ using the mapping defined by (B.5). The projections $\tilde{\mathbf{X}}^b$ and $\tilde{\mathbf{X}}^i$ are used to train a kernel ridge classifier. A new EEG recording $X[n]$ can be classified by first projecting it on the manifold and using the classifier to determine the status, ictal vs. baseline. Note that the mapping in (B.5) is only defined for the training samples, we can extend it by interpolating around the nearest neighbors of $X[n]$ in the training data.

To find an optimal decision boundary that will separate class ictal from class baseline on the manifold, we need to minimize a cost function estimated from the training samples. To obtain a minimum cost we perform M-fold cross validation on the set of available training data. This method randomly partitions the dataset into M disjoint sets [56]. The classifier is trained with $90\,\%$ of the data from the M sets and the remaining randomly chosen $10\,\%$ is used for testing or validation. The optimality of the learning parameters for the ridge model will be determined by those values resulting in minimum classification error of the training set. The error is obtain from the mean square error computed as shown in (13).

A.3   Related techniques

The purpose of this section is to briefly present related techniques for dimensionality reduction and clarify the choice of method in this thesis.

A.3.1 Principal Component Analysis

One of the most commonly used methods for dimensionality reduction and feature extraction in machine learning is the Principal Component Analysis. PCA performs a linear transformation on the data and the result is an orthogonal basis set [56]. This technique also offers an estimate of the intrinsic dimensionality of the data by identifying the first projection axis in which the largest variance is accumulated. The mathematical background of Principal Component Analysis is overviewed in e.g., [56,78] and is beyond the scope of this thesis. Although PCA is used commonly for EEG analysis, it assumes a linear combinations of neural signals. Since it is not clear that neural signals are mixed linearly, we have chosen to apply a nonlinear technique and compare it with PCA.

A.3.2 Independent Component Analysis

An extension to PCA is Independent Component Analysis (ICA) which uses higher order correlations, i.e nonlinear processing to not only orthogonalize the signals but also separate the original signals. Further details on ICA can be found in [79, 80]. The goal of this work is to discriminate for arbitrarily probability density functions and nonlinear mixture of signals.

A.3.3 Correlation dimension

A nonlinear method which does not assume a linear mixture is the correlation dimension estimation method. Although this method provides an indication of a seizure through nonlinear dynamics [71, 81], it does not find a lower dimensional representation of the signals. The decrease on the correlation dimension estimate may suggest that there exists an intrinsic change in the brain at the ictal state as time evolves where is causing the complexity of the data to be reduced. During ictal periods the neurons begins to act synchronously. Neurons are firing in agreement to each other in the region of the brain where the seizure is occurring.

A.4 Experiments

This section presents two sets of experimental results; 1) classification of measured data on an acute rat model of epilepsy and 2) classification of *in vivo* measured of human EEG data. The motivation for initially using the acute rat model because it is believed to be similar to a non-induced set of signals from a human EEG.

A.4.1 Acute rat model of epilepsy

The data used for this work were collected from 64 silver electrodes with 2 kHz sampling placed on a rat's scalp in a 8×8 grid, as sketched in Fig. A.4. The baseline data were collected on a normally functional rat's brain and the ictal state was induced chemically. For the purposes of training and *a priori* information, the EEG recordings were labeled in baseline and ictal states by a neuroscientist. Two out of the 64 channels contained large amplitude muscular artifacts and the data from these two channels is discarded, making $D = 62$. As a pre-processing step the time series is filtered using a 15th order Chebyshev filter with cutoff frequency of 100 Hz. The selection of this cutoff frequency was based on the maximum bound of frequency rhythms discussed in [69].
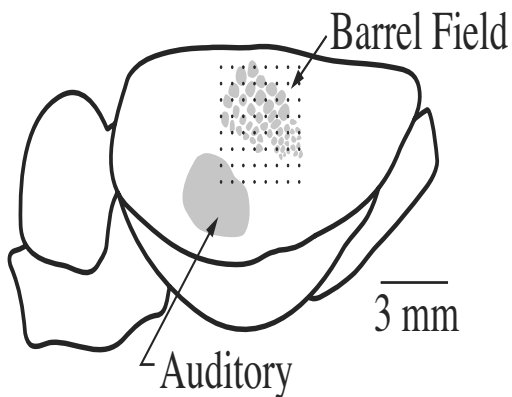
Figure A.4: Map of 8×8 grid of electrodes for scalp EEG measurements on rat acute model of epilepsy. The barrel field describes points where electrodes are placed and the auditory center is shown for reference.

The set of training data consists of the concatenation of $\mathbf{X}^b$ and $\mathbf{X}^i$ with $M = 1430$, $N = 2\,M$, and $D = 62$. A portion of this dataset is used to determine the most appro-
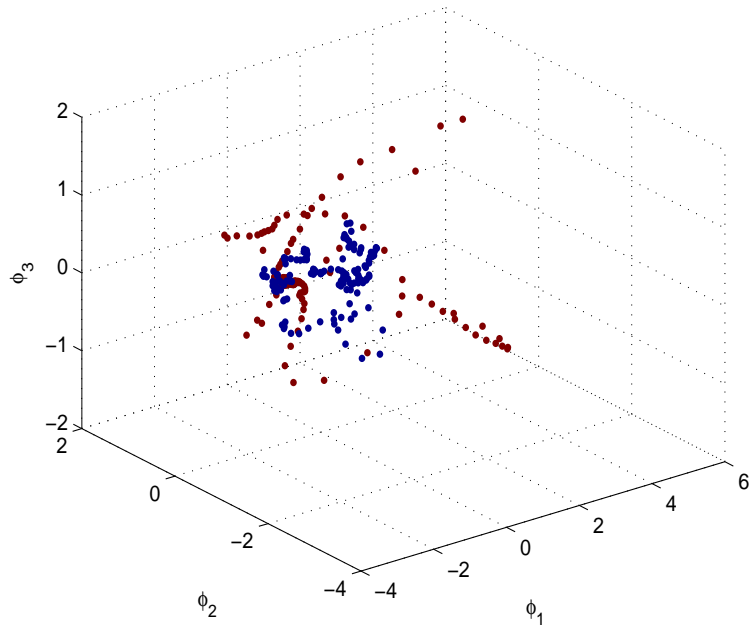
Figure A.5: Reconstructed manifold using first three principal components from PCA. This means that the 3 electrodes that best represented the dataset were chosen as principal components. Each point belongs to an instant in time. The color points are true labels representing the class (red = ictal and blue = baseline)

priate classifier parameters for the given signals. In this case, we use 10% of baseline and ictal data, i.e. a 10-fold cross validation was used on the set of available training data to estimate the optimal learning parameters for the kernel ridge regression. From these, 90 % of $\mathbf{X}^b$ and $\mathbf{X}^i$ was used to train the classifier and the remaining 10 % for validation. For the purposes of comparison, the lower dimensional representations were constructed with PCA and Laplacian Eigenmaps. The resulting maps are shown in Fig. A.5 and Fig. A.6. In these figures, each of the points represent an EEG recording with dimensionality d, at a given time. In these figures the red points represent ictal states and the blue represent baseline states which were known *a priori* from the labeling. The colors in the graph represent the state in which each of the points belong to. The color labels shown here are the true labels for the classes ictal (red) and baseline (blue). The only difference between Figs.A.5 and A.6 is that the lower dimensional representation was constructed by using PCA or Laplacian, but the structure of the plots
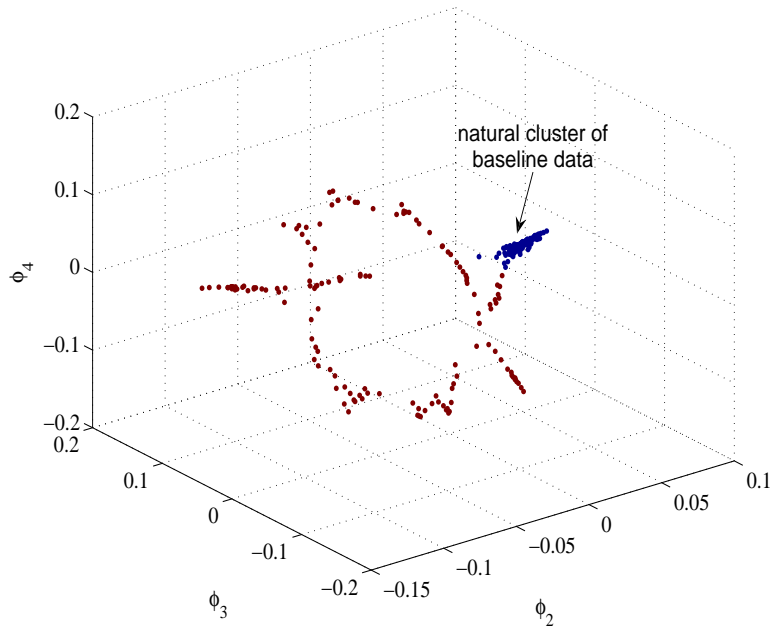
Figure A.6: Reconstructed manifold using first three non-trivial eigenvectors from the Laplacian eigenmap. Each point belongs to an instant in time. The color points are true labels representing the class (red = ictal and blue = baseline)

is very different. The practical meaning of these plots in this case is that the Laplacian Eigenmap approach shows a more organized structure and a natural clustering of the ictal states. Hence ictal and baseline states become easily separable. This implies that a threshold can be defined on the manifold that can go back to the time domain data and provide a marker to the physician indicating the onset of the seizure. The sample points shown in Fig. A.5 and Fig. A.6 belong to the training set that were pre-labeled by an expert. The ultimate goal is to identify seizures automatically and therefore the same approach was applied to non *a priori* labeled data which is shown in Figures A.7(a) and A.7(b). The results of this classification and comparison are quantified in Tables A.1 and A.2.

Note that PCA is unable to partition the data into ictal state and baseline state, whereas the Laplacian eigenmaps reveals the organization of the dataset into ictal and baseline. It is therefore expected, that the classification on the manifold reconstructed by the Laplacian eigenmaps will outperform the classification based on the projection

of the subspace discovered by PCA.

For this dataset the minimum error on cross-validation was obtained by keeping $d = 10$ eigenvectors, and choosing the ridge parameter $\lambda = 0.1$. The width of the Gaussian kernel for the weighted adjacency graph was $\sigma_A = 0.6$, and the width of the Gaussian kernel for the regression was $\sigma_R = 0.05$. A detailed description of the Gaussian kernel ridge classifier is presented in the appendix. We used $k = 5$ nearest neighbors to construct the adjacency graph. The performance of these algorithms was measured by calculating the mean square error.

Table A.1: Percentage of Classification Accuracy using Gaussian Kernel Ridge Regression

	Baseline Class	Ictal Class	Total
Raw Data	78.32	68.53	73.43
PCA	91.04	64.18	77.61
Graph Laplacian	98.51	97.01	97.76

Table A.2: Percentage of Classification Accuracy using Linear Ridge Regression

	Baseline Class	Ictal Class	Total
Raw Data	83.22	98.60	90.91
PCA Projection	90.21	73.43	81.82
Laplacian Manifold	100	88.81	94.91

Figures A.7(a) and A.7(b) show the outcome of the classification for the validation set (10 % of the $N = 2860$ samples) using PCA and the Laplacian eigenmaps for reducing dimensionality. After using the graph Laplacian method to reduce the dimensionality of the set, most of the points are properly labeled as seen in Fig. A.7(b). This is not the case when PCA is used to reduce dimensionality; a large number of points are misclassified as shown in Table A.1. For reference purposes we have also included the classification accuracy when the classification is performed directly on the raw data. The reduction of dimensionality provided by the Laplacian eigenmaps resulted in the highest classification accuracy.

A.4.2 Human in vivo electroencephalogram recordings

An extension to this work has been performed using human EEG data. This set comes from scalp electroencephalograms with 55 electrode channels recording at 256 Hz. As in the acute rat model of epilepsy dataset, the human data was analyzed using dimensionality reduction methods such as the Graph Laplacian and PCA. A classification was performed in a reconstructed subspace with lower dimensionality than the original ambient space. For this set, $D = 55$ and $d = 10$. Figure A.8 shows the reconstruction of the lower dimensional manifold using the Graph Laplacian. The blue crosses correspond to a baseline brain state and red dots to ictal. It is interesting to observe how the dimensionality of the ictal state seems to be of a lower degree than the baseline state. This observation is in accord with the observations of [71] and [72] where it was discussed the noticeable decrease in dimensionality on the neuronal signals before and during a seizure onset.

In addition to the noticeable decrease in dimensionality for the ictal versus the baseline states, the behavior of the data as it evolves through time should be observed carefully. In Fig. A.9 each of the samples in the graph represent an instant in time from the EEG recordings with dimension d. Notice how the post-ictal and baseline states represented by "∘" and "x" reside in the same area of the manifold. Both of these states are related to a normal EEG. However, as the seizure onsets (pre-ictal), the recording begins to move towards the manifold region that is predominantly resided by the ictal time samples. These observations can be related back to previous ones made by using nonlinear dynamics techniques. The time progression from pre-ictal to ictal states validate the hypothesis of expecting a less chaotic behavior during a seizure (lower dimensionality). As the seizure progresses the signal is propagated into a clustered region of the manifold and once it returns to normal state (post-ictal) it moves towards the more chaotic region of the reconstructed manifold.

The classification on the manifold and the lower dimensional reconstruction obtained from PCA was done by using the kernel ridge method as in Section A.4.1. This experiments show that the Graph Laplacian combined with the Kernel Ridge Model

outperforms PCA and Kernel Ridge. The quantitative comparison of these results are presented on Table A.3. The classification using PCA resulted in 82.20 % while the Laplacian method provided 91.40 % classification accuracy.

Table A.3: Human Data: Percentage of Classification Accuracy using Kernel Ridge Model

	Baseline Class	Ictal Class	Total
Raw Data	93.20	70.40	81.80
PCA Projection	81.60	78.80	82.20
Laplacian Manifold	100	82.80	91.40

A.5 Conclusion

This thesis presented a new approach to classify EEG time series from a rat acute model of epilepsy and *in vivo* human EEG using manifold learning techniques. It was shown that the eigenvectors of the Graph Laplacian provide a natural low dimensional representation for the dataset. The projection of the ictal and baseline states on the manifold are well separated. A kernel ridge classifier was used to find the optimal boundary between and ictal and baseline states on the manifold. A quantitative evaluation of this approach using an acute rat model of epilepsy was performed and shown in Tables A.1-A.3. The experiments showed that the approach presented here outperforms traditional PCA. This fact can be seen in the significant increase on the detection accuracy from 77.61 % with PCA to 97.76 % using the graph Laplacian and the kernel ridge classifier.

In traditional Ridge Regression models the set of input data is given as a series composed of $(\mathbf{x}_1, y_1), ..., (\mathbf{x}_N, y_N)$ where N is the sample length, y are the sample's labels, and $\mathbf{x} \in \Re^D$. However, the interest of this work is to perform the classification of the samples on the lower dimensional space containing the eigenvectors of the Graph Laplacian instead of the raw data time samples. Hence, the samples used on the ridge model will be defined as $(\phi_1^T, y_1), ...(\phi_d^T, y_d)$ where each ϕ_i^T is an N dimensional row vector corresponding to the number of samples and $\Phi \in \Re^{N \times d}$. The kernel ridge model consists of the ridge coefficients $\hat{\beta}_{ridge}$ given by,

$$\hat{\beta}_{ridge} = \arg\min_{\beta}\{\sum_{i=1}^{N}\left(y_i - \hat{\beta}_0 - \sum_{j=1}^{d}\beta_j\phi_{ij}\right)^2 \tag{6}$$

$$+ \lambda\sum_{j=1}^{d}\beta_j^2\}. \tag{7}$$

as defined in [57, 76, 78]. The learning parameter λ should be carefully chosen to not introduce higher bias to the output estimate $\hat{y}$. Therefore, the choice for an optimum value of λ should be based on the region where this scalar reaches a stable value for $\hat{\beta}_{ridge}$ [82]. Based on the experiments, the optimum λ should be selected between the range of 0.2 and 0.3. The Kernel Ridge coefficients need also to be optimized as

$$\hat{\beta}_{ridge} = \arg\min_{\beta}\left\{\sum_{i=1}^{N}\left(y_i - \hat{\beta}_0 - \sum_{j=1}^{d}\beta_j\phi_{ij}\right)^2\right\}, \tag{9}$$

$$\text{subject to: }\sum_{j=1}^{d}\beta_j^2 \leq s,\ s > 0.$$

The problem simplifies into computing the $\hat{\beta}_i^{ridge}$ where $i = 1,...,d$ with the following

$$\hat{\beta}_{ridge} = (X^TX + \lambda I)^{-1}X^Ty \tag{8}$$

with offset coefficient $\hat{\beta}_0$ as

$$\hat{\beta}_0^{ridge} = \left[\frac{1}{N}\sum_{i=1}^{N}y_i\right] - \left[\sum_{j=1}^{d}\bar{\phi}_j\hat{\beta}_j^{ridge}\right]. \tag{9}$$

The Kernel Ridge regression built from $\hat{\beta}_{ridge}$ maps the input data into a Kernel space in which the discrimination of nonlinear data is simplified. This mapping is obtained from

$$\psi_i(x) = K(\phi_i^T, \xi), \tag{10}$$

where ϕ_i^T is the ith eigenvector of the graph Laplacian from the training samples and ξ is an eigenvector from the test set graph Laplacian. The kernel used in this work was the Gaussian Kernel, defined by:

$$K(\phi_i^T, \xi) = \exp\left(-||\phi_i^T - \xi||^2/(2\sigma^2)\right). \tag{11}$$

The estimated outputs labels, $\hat{y}$, resulting from the decision boundary model now become

$$\hat{y} = \hat{\beta}_0 + \sum_{i=1}^{N} K(\phi_i^T, \xi) \tag{12}$$

and the classification error is given by

$$e(x) = \frac{1}{N} \sum_{i=1}^{N} \left(y_i - \hat{y}_i\right)^2, \tag{13}$$

where N is the number of samples, $\hat{y}$ is the estimated output label and y is the true known class label.
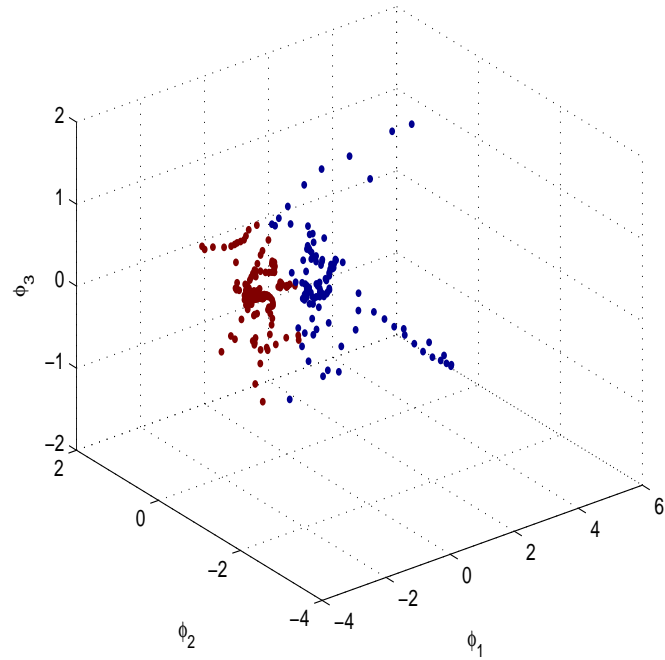
(a)
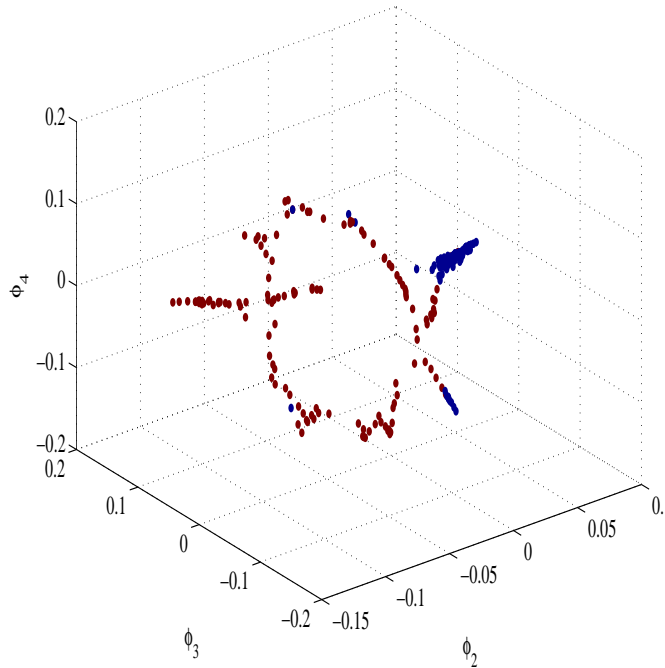
(b)

Figure A.7: Classification results using reconstructed manifolds from PCA and Laplacian Eigenmaps. The labels in the figure are the result of the classification algorithm. The corresponding quantitative results are shown in Table A.2; (a) same reconstructed manifold using PCA shown in Fig. A.5. Various points from the ictal state were misclassified as belonging to baseline, (b) reconstructed manifold using Laplacian eigenmaps from Fig. A.6

115
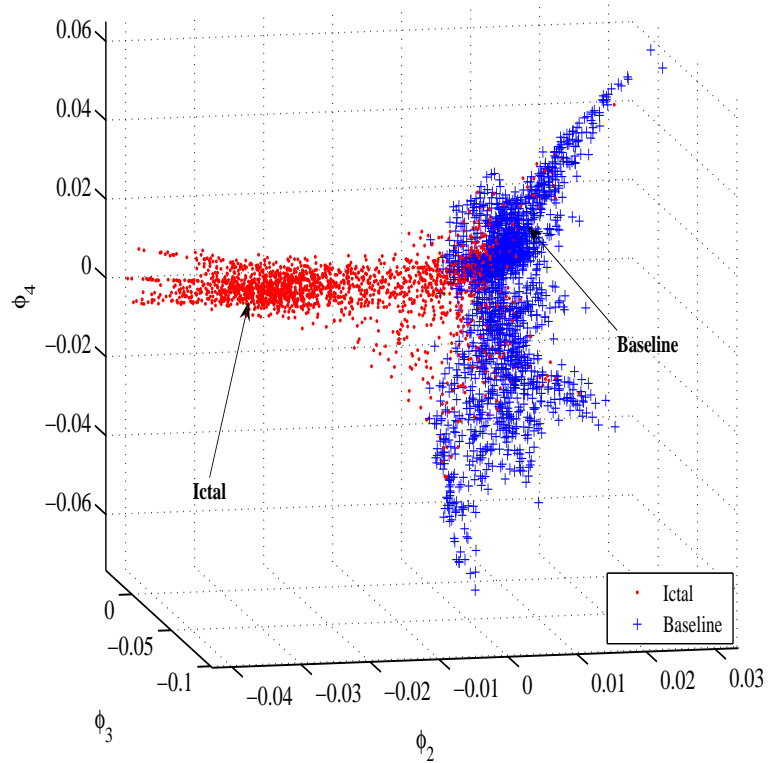
Figure A.8: Reconstructed manifold for *in vivo* human recordings using the Graph Laplacian. The first three non-trivial eigenvectors are shown. Each point is an instant in time. Notice that ictal and baseline states lie on different regions of the reconstructed manifold, validating the initial hypothesis of this work.
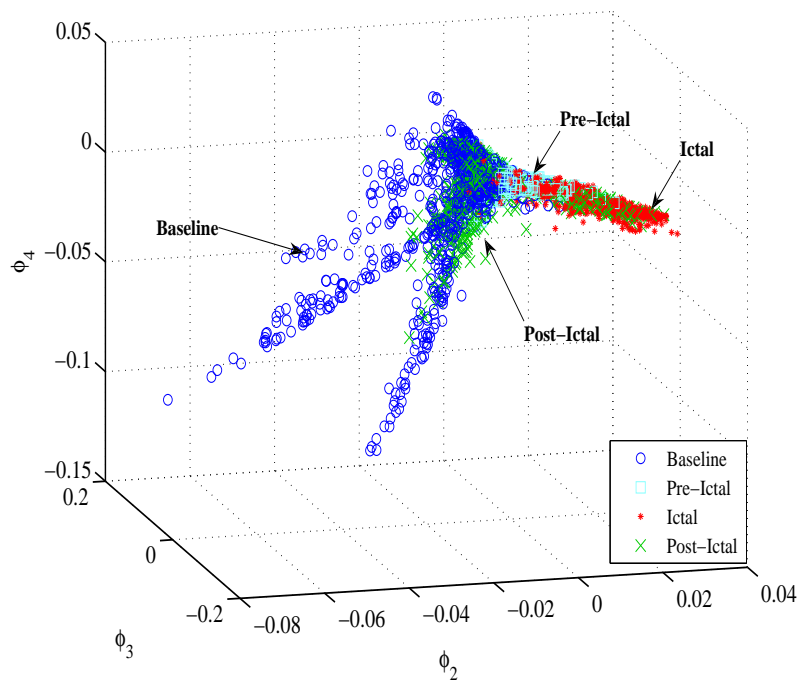
Figure A.9: Reconstructed manifold showing the time progression of an EEG as the brain goes from normal state to an epileptic seizure (pre-ictal, ictal, and post-ictal states). The manifold shown was reconstructed by the graph Laplacian and shows how the ictal state is more compacted, implying a lower dimensionality. As time progresses the measurements move from a more chaotic structure (pre-ictal and baseline) to an organized cluster (ictal) marked by red asterisks.

Appendix B

Embedded Target Detection in Multispectral Images using Laplacian Manifolds

B.1   Introduction

The field of Remote Sensing deals with the detection and collection of certain characteristics of an object measured from a distance. Each object possesses a unique response to sunlight that is characteristic of its own reflectance. Currently, there are sensors capable of measuring the reflectance from different objects at different wavelengths. Some currently available sensors are the multispectral and hyperspectral sensors. Several of the existing airborne and spaceborne, multispectral and hyperspectral, sensors acquire greater amount of spectral information by collecting data on narrow band channels on the electromagnetic spectrum. By acquiring this information, a spectral signature that is particular to an object is obtained, thus obtaining the object's spectral information and reflectance. The amount of spectral information is correlated to how narrow are the bands in each sensor. For example the hyperspectral, Airborne Visible/Infrared Imaging Spectrometer, (AVIRIS), obtains data between $0.4\,\mu\mathrm{m}$ to $2.45\,\mu\mathrm{m}$ at $10\,\mathrm{nm}$ intervals in 224 channels.

Even though the aforementioned sensors provide much information about the scene, the detection of particular objects of interest becomes cumbersome due to several factors. For example, in subsurface sensing the fundamental goal is the detection of objects embedded in a diffusive and dispersive medium such as the atmosphere, the ocean waters, and organic tissue. Therefore, it is essential to develop a pattern recognition set of tools that retrieves the information necessary to identify the objects of interest.

In the field of remote sensing and pattern recognition, one of the main goals is to detect, classify and identify different objects based on their features. The term detection is referred to the identification of a target of interest based on prior statistical information of the target given that no other feature on the data is of interest and other prior information of other features are known. Classification, on the other hand, deals with the assignment of groups or classes to features of similar characteristics, in this case, statistical characteristics. Classification can be viewed as a data discrimination process. Detection and classification depend highly on the estimation of parameters in order to be able to identify and discriminate targets and classes. Estimation can be described as a statistical inference based on a set of samples given that the statistics of the population cannot be calculated. Estimation is used to provide the classifiers with the estimated statistical information, i.e. mean and covariance matrices, that is necessary to these classifiers to work.

The goal in classification theory is to obtain a decision boundary between a group of objects or classes from the data being analyzed and to be able to discriminate the data amongst them. For example Figure 3 shows, as an example, an ideal linear decision boundary able to discriminate the features of class w_i from the ones in class w_j, classifying and identifying feature X as belonging to class w_j.

There are other decision rules in classification that use additional statistical parameters of the data. For example in quadratic classifiers both the first and second order statistics are used. Figure 4, shows an example of the classification of feature X by means of a quadratic decision boundary. The selection of a specific decision rule depends on the statistical characteristics of the data. In cases where the data is well separated, a

linear classifier could provide high accurate results. For the situation when the data cannot be discriminated by using only first order statistics, then quadratic classifiers could improve the results of the classification [8]. These decision boundary rules are used in two common classification mechanisms: unsupervised mechanisms and supervised machine learning algorithms. Also, there is a class of algorithms that does not depend on the estimation of the data statistical parameters. These group of algorithms are usually refereed to as non-Bayesian classifiers.

This chapter will make use of a non-Bayesian classifier based on Gaussian kernel non-linear classification. It includes various synthetic experiments performed on a set of sample hyperspectral imagery acquired by HYPERION, HYDICE, and AVIRIS sensors. This set of sensors collect information in more than 200 spectral bands over the visible through short-wave infrared wavelengths including 0.4μm to $2.5\,\mu$m. In this range, a large portion of the solar radiation is recorded as well as a contribution from the thermal band [83]. Several of the currently available sensors are able to supply spectral resolutions of about $10\,$nm. This accounts for very detailed and useful information regarding specific targets in the image that could be exploited in the implementation of classification and detection algorithms.

Several experiments were conducted varying distinct parameters such as : number of bands, number of frames, with the addition of noise, coarsening and normally distributed random jitter. Section B.2 presents the methodology followed to generate the set of data that was used to validate the performance of the proposed algorithms. Section B.3 describes the unsupervised techniques applied for manifold learning and target detection. Some of the results will be shown in Section B.4.

B.2   Generation of Data Set

B.2.1   Sensor: HYPERION

The simulated data in this work was acquired by HYPERION. It is shown in Fig. B.1. HYPERION offers up to 220+ contiguous spectral bands measuring from 0.4μm to

2.5μm. It acquires visible/near-infrared (400 nm to 1000nm) and shortwave infrared (900 nm to 2500 nm) spectral data. The spatial resolution of HYPERION is 30 meters and each image covers a 7.5 km by 100 km area.

Figure B.1: Sample of image acquired by Hyperion sensor. This sensor offers up to 220+ contiguous spectral bands measuring from 0.4μm to 2.5μm. It acquires visible/near-infrared (400 nm to 1000nm) and shortwave infrared (900 nm to 2500 nm) spectral data. The spatial resolution is 30 meters and each image covers a 7.5 km x 100 km area

In this stage of the work, an algorithm was developed to mimic a set of data of hyperspectral imagery. This algorithm simulates several disturbances and noise conditions. The steps describing the data generation algorithm developed is presented in Figure B.2.

The generation method is as follows. First, select the multispectral/hyperspectral image of interest. In order to simulate the suggested target profile, several black-body curves were computed at various temperatures. The obtained curves are shown in Fig. B.3. Since the target of interest follows a given temperature profile

Since the target of interest follows a given temperature profile, the approximation of temperature versus phase in time can be approximated as shown in B.4.
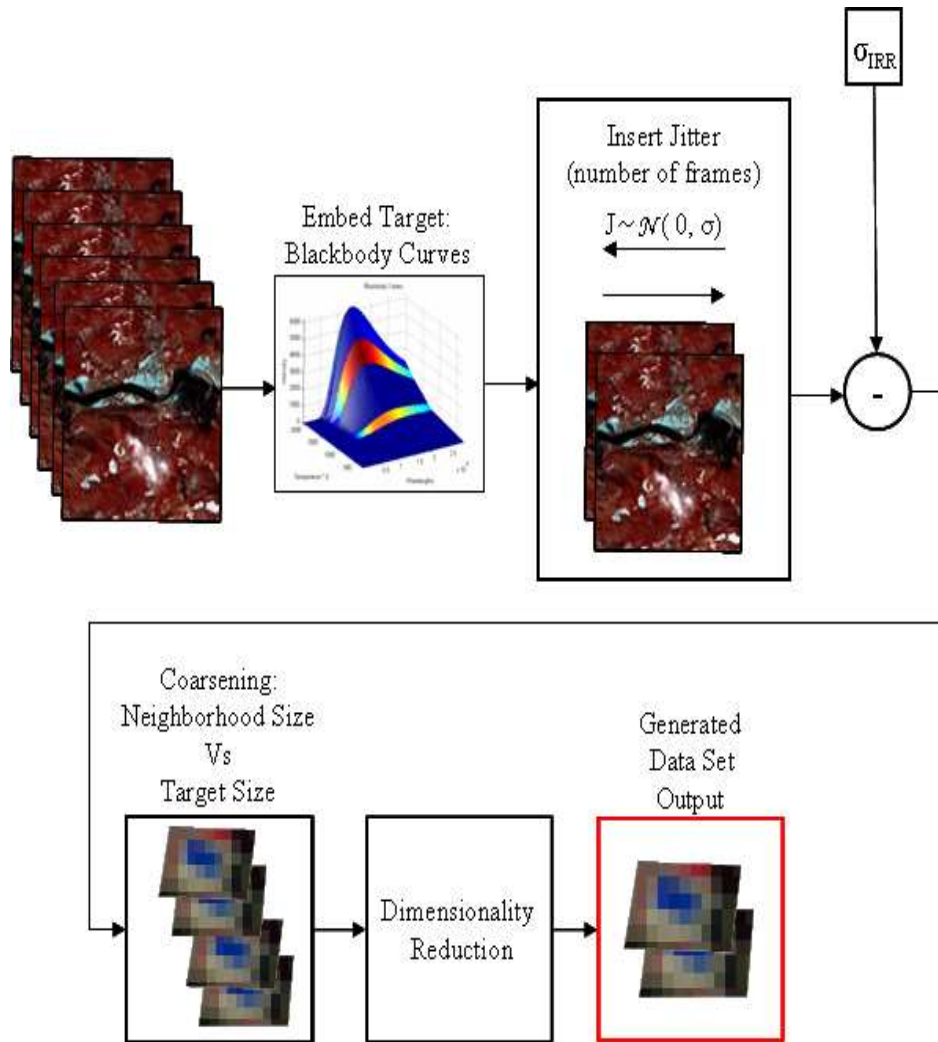
Figure B.2: Flowgraph of synthetic data generation process to embed target in hyperspectral image

B.3 Clustering on Manifold

This work proposes an approach based on manifold learning similar to the one used in Appendix A. This method assumes that there exists a well sampled underlying lower dimensional manifold in which the classes in the data are naturally discovered. In addition to finding the manifold, a clustering algorithm based on C-means is applied to the data to label the classes as corresponding to background or target. Both of this two methods do not require any training or a priori knowledge of the classes in the data. However, a cross validation step is included in order to select the parameters in which
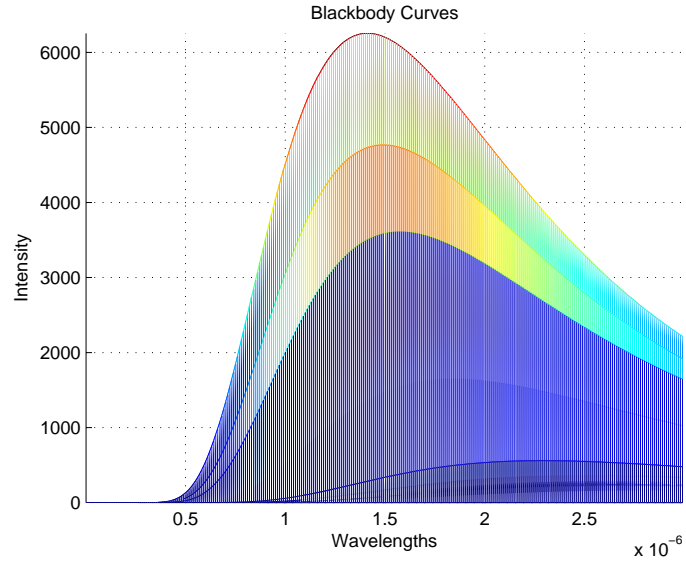
Figure B.3: Blackbody curves for different embedded target profiles to be embedded in hyperspectral data
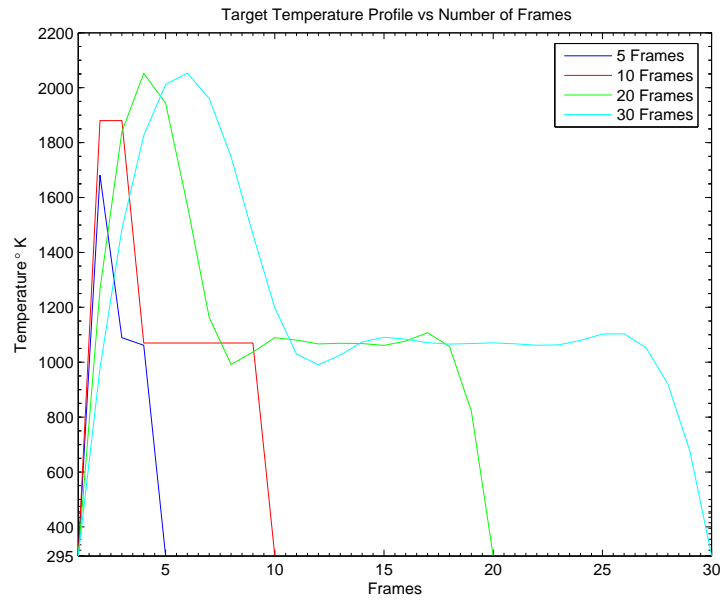
Figure B.4: Profile of target temperature vs number of frames used in the synthetic set of temporal and hyperspectral data

the error achieves a minimum.

B.3.1 Laplacian Eigenmaps

The samples obtained from the synthetic data can be used to approximate the true underlying manifold of the hyperspectral image. We build a graph that should provide a good approximation to the geometry of the manifold. A graph that should provide a good approximation to the geometry of the manifold is built. The vertices of the graph are pixels at a given instant in time with spectral information. Let $X((p_i, \lambda_j), t) \ \forall t = 1, ..., N$, where t is time, N is the number of frames, p_i is pixel i and λ_j a spectral band, be a column of $\mathbf{X}$. The edges define the proximity on the underlying manifold. The vertices are connected using the k-nearest neighbors approach: the nodes i and j are connected by an edge if i is among the k-nearest neighbors of j. A weight is assigned, $W_{i,j}$, to the edge between the nodes i and j and given by

$$W_{i,j} = \exp(-\|X((p_i, \lambda_i), t) - X((p_j, \lambda_j), t)\|/(2\sigma^2)). \tag{B.1}$$

Once the connected graph is constructed, its Laplacian matrix is computed, L, on the graph as defined by $L_{i,j} = A_{i,j} - W_{i,j}$, where the adjacency matrix, A, is defined as

$$A_{i,j} = \begin{cases} \sum_k W_{k,i} & \text{if } i = j \\ 0 & \text{otherwise.} \end{cases} \tag{B.2}$$

The the eigenvectors, $[\phi_1, ..., \phi_D]$ are computed as the solution to the following eigenvalue problem

$$L\phi_k = \kappa_k A\phi_k, \tag{B.3}$$

where κ_k is the corresponding eigenvalue. As is explained in [10], [73], the eigenvectors, $\phi_1, ..., \phi_D$, provide the optimal embedding of the manifold. The mapping defined by

$$X \rightarrow \Phi(X) = [\phi_1|...|\phi_D]^T(X)$$

preserves the Euclidean distance locally by minimizing the following distortion

$$\sum_{ij} \|\phi_i - \phi_j\|^2 W_{ij} = tr(\Phi^T L \Phi). \tag{B.4}$$

The vector ϕ that minimizes (B.4) is provided by the lowest non-trivial eigenvalue solution of the generalized eigen-problem in (B.3). The reduction of dimensionality is achieved by defining the mapping from $\mathbb{R}^D \to \mathbb{R}^d$ as follows

$$X((p_i, \lambda_j), k) \to \tilde{X}((p_i, \lambda_j), k) = \text{column } k \text{ of } \tilde{\Phi}(X) = [\phi_1|...|\phi_d]^T(X). \qquad \text{(B.5)}$$

B.3.2 C-means Clustering

Once the eigenvectors from the Laplacian are obtained then a classic C-means clustering algorithm is applied to this set. The goal of this algorithm is to find the C mean vectors $\mu_1, \mu_2, ..., \mu_C$ or centroids of the data that minimize the distance between the points and the centroids. In this work , the distance used is given by the Euclidean metric.

$$d = ||\tilde{X}((p_i, \lambda_j), t) - \tilde{X}((p_i, \lambda_j), t)||^2 \; \forall t = 1, ..., N \qquad \text{(B.6)}$$

The description of the C-means clustering algorithms as delineated in [56] follows.

Classification Algorithm

begin initialize n,c,$\mu_1\mu_2, , ..., \mu_c$

    do classify n samples according to nearest μ_i

        recompute μ_i

    until no change in μ_i

    return $\mu_1\mu_2, , ..., \mu_c$

end

B.4 Experiments and Results

Several experiments were conducted using an excerpt of an original image acquired by HYPERION. Variations of irradiance noise, σ_{IRR}, between the values of 0.05 and 0.1 are presented. Also, the range for the number of frames varied from 5,10,20 for some of the experiments. The number of bands ranged from 1, 5, 10. The target size with respect to the pixel size changed from 0.20 %, 0.25 %, and 0.5 %. The methodology followed the algorithm described previously and also explained in Fig. B.2.
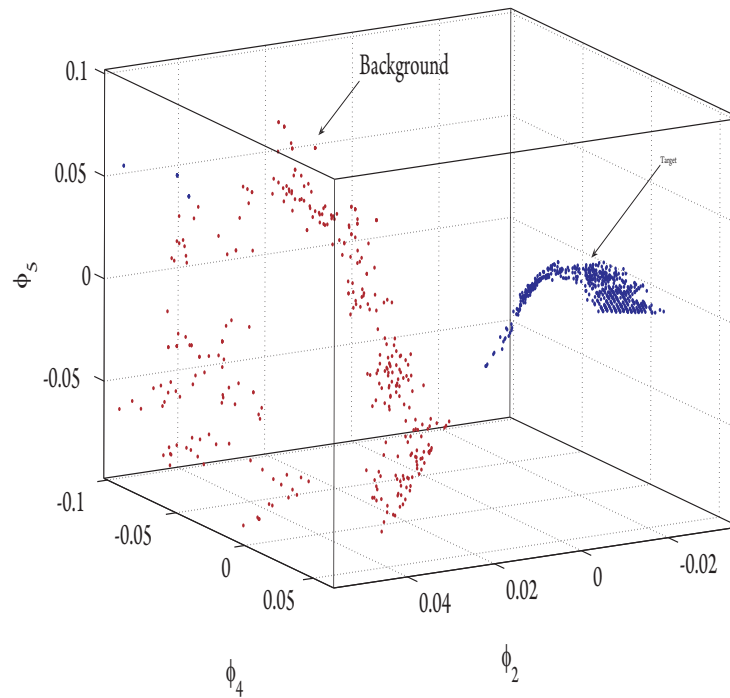
Figure B.5: Samples from the eigenvectors of the Laplacian. The blue dots represents the samples in time and space belonging to the background. The red dots correspond to the embedded target for Set #3

Data Generation Algorithm

1) Select a region of interest from an original hyperspectral image

2) Select number of bands to reduce

3) Select number of frames

4) Introduce percentage of irradiance noise

5) Select target size in pixels

6) Find the underlying manifold using Laplacian Eigenmaps

   a)Choose kernel width

   a)Choose k-nearest neighbors

7) Perform C-means clustering on the eigenvectors of the Laplacian matrix

Table B.1: Parameter description of synthetic data sets used to test Laplacian eigenmaps algorithms and embedded target detection

	NN-size	Target size (pixels)	Noise std	Frames	Band Subset
Set 1	10	10	0	5	5
Set 2	10	5	0.05	5	5
Set 3	10	10	0	10	1
Set 4	10	5	0.05	10	10
Set 5	20	5	0.1	20	5

Table B.2: Results of clustering using Laplacian eigenmaps and C-means. Accuracy results for background, target, and total are displayed in percentages

	textAccuracy Background	Accuracy Target	Total Accuracy
Set 1	100	76.1	97.8
Set 2	70.95	100	77.40
Set 3	100	0 (undetected)	90
Set 4	89.92	95.31	91.5
Set 5	83.16	100	86.4

Bibliography

[1] E. Niedermeyer and F. L. da Silva, *Electroencephalography: basic principles, clinical applications, and related fields.* Williams and Wilkins, 1999.

[2] B. T. Rosner and D. W. van der Weide, "High-frequency near-field microscopy," *Review of Scientific Instruments*, vol. 73, no. 7, pp. 2505–2525, 2002.

[3] A. Imtiaz, T. Baldwin, H. T. Nembach, T. M. Wallis, and P. Kabos, "Near-field microwave microscope measurements to characterize bulk material properties," *Applied Physics Letters*, vol. 90, no. 24, p. 243105, 2007.

[4] M. Tabib-Azar, N. S. Shoemaker, and S. Harris, "Non-destructive characterization of materials by evanescent microwaves," *Measurement Science and Technology*, vol. 4, pp. 583–590, May 1993.

[5] C. Jakowatz, Jr and D. Wahl, "Eigenvector method for maximum likelihood estimation of phase errors in synthetic aperture radar imagery," *Journal of Optical Society of America*, vol. 10, 1993.

[6] E. N. Grossman, A. K. Bhupathiraju, A. J. Miller, and C. D. Reintsema, "Concealed weapons detection using an uncooled millimeter-wave microbolometer system," pp. 364–369, July 2002.

[7] E. N. Grossman, C. R. Dietlein, J. E. Bjarnason, M. Ramírez, M. Leivo, J. A. Penttila, P. Helisto, and A. Luukanen, "Imaging with modular linear arrays of cryogenic Nb microbolometers," *Society of Photo-Optical Instrumentation Engineers (SPIE) Conference Series*, vol. 6948, May 2008.

[8] C. Dietlein, Z. Popović, and E. N. Grossman, "Aqueous blackbody calibration source for millimeter-wave/terahertz metrology," *Appl. Opt.*, vol. 47, no. 30, pp. 5604–5615, 2008.

[9] T. Frank, "Body scanners replace metal detectors in tryout at tulsa airport," USA Today, February 17 2009.

[10] M. Belkin and P. Niyogi, "Laplacian eigenmaps for dimensionality reduction and data representation," *Neural Computation*, vol. 15 6, pp. 1373–1396, 2003.

[11] T. Hastie, R. Tibshirani, and J. H. Friedman, *The Elements of Statistical Learning.* Springer, August 2001.

[12] M. Belkin and P. Niyogi, "Laplacian eigenmaps and spectral techniques for embedding and clustering," *Advances in Neural Information Processing Systems*, vol. 14, 2002.

[13] R. Gonzalez and R. Woods, *Digital Image Processing*, 2nd ed. Prentice-Hall, 2002.

[14] A. H. Lettington, S. Tzimopoulou, and M. P. Rollason, "Nonuniformity correction and restoration of passive millimeter-wave images," *Optical Engineering*, vol. 40, no. 2, pp. 268–274, 2001.

[15] C. Jakowatz Jr, D. Wahl, P. Eichel, D. Ghiglia, and P. Thompson, *Spotlight-mode synthetic aperture radar: A signal processing approach.* Kluwer Acadamic, 1996.

[16] D. Wahl, P. Eichel, D. Ghiglia, and C. Jakowatz, Jr., "Phase gradient autofocus: A robust tool for high resolution sar phase correction," *IEEE Transactions on Aerospace Electronic Systems*, vol. 30, pp. 827–835, July 1994.

[17] P. H. Eichel, D. C. Ghiglia, and C. V. Jakowatz, Jr., "Speckle processing method for synthetic-aperture-radar phase correction," *Optics Letters*, vol. 14, pp. 1–3, Jan. 1989.

[18] W. D. Brown and D. C. Ghiglia, "Some methods for reducing propagation-induced phase errors in coherent imaging systems. i. formalism," *J. Opt. Soc. Am. A*, vol. 5, no. 6, pp. 924–941, 1988.

[19] D. C. Ghiglia and W. D. Brown, "Some methods for reducing propagation-induced phase errors in coherent imaging systems. ii. numerical results," *J. Opt. Soc. Am. A*, vol. 5, no. 6, pp. 942–957, 1988.

[20] C. E. Mancill and S. J. M., "A map drift autofocus technique for correcting higher order sar phase errors," *Proc. 27th Annu. Tri-Service Radar Symp. Record*, pp. 391–400, June 1981.

[21] P. Tsakalides and C. Nikias, "High-resolution autofocus techniques for sar imaging based on fractional lower-order statistics," *Radar, Sonar and Navigation, IEE Proceedings -*, vol. 148, no. 5, pp. 267–276, Oct 2001.

[22] J. Fienup, "Phase error correction by shear averaging," *Technical Digest Series, Signal Recovery and Synthesis*, vol. 15, pp. 134–137, June 1987.

[23] F. Berizzi and G. Corsini, "Autofocusing of inverse synthetic aperture radar images using contrast optimization," *Aerospace and Electronic Systems, IEEE Transactions on*, vol. 32, no. 3, pp. 1185–1191, Jul 1996.

[24] J. Morrison, R.L., J. Munson, D.C., and M. Do, "Avoiding local minima in entropy-based sar autofocus," *Statistical Signal Processing, 2003 IEEE Workshop on*, pp. 454–457, Oct. 2003.

[25] R. L. Morrison and D. C. Munson, "An experimental study of a new entropy-based sar autofocus technique," *Proc. of the Int. Conf. on Image Processing 2*, pp. 441–444, 2002.

[26] T. Calloway and G. Donohoe, "Subaperture autofocus for synthetic aperture radar," *Aerospace and Electronic Systems, IEEE Transactions on*, vol. 30, no. 2, pp. 617–621, Apr 1994.

[27] D. Donoho and I. Johnstone, "Adapting to unknown smoothness via wavelet shrinkage," *Journal of the American Statistical Association*, vol. 90, Dec. 1995.

[28] C. Stein, "Estimation of the mean of a multivariate normal distribution," *The Annals of Statistics*, vol. 9, Nov. 1981.

[29] P. Eichel, D. Ghiglia, and C. Jakowatz, Jr, "Speckle processing method for synthetic aperture radar phase correction," *Optics Letters*, vol. 14, Nov. 1989.

[30] R. Coifman and M. Wickerhauser, "Entropy based algorithm for best basis selection," *IEEE Transactions on Information Theory*, vol. 38, 1992.

[31] J. E. Bjarnason, T. L. J. Chan, A. W. M. Lee, M. A. Celis, and E. R. Brown, "Millimeter-wave, terahertz, and mid-infrared transmission through common clothing," *Applied Physics Letters*, vol. 85, no. 4, pp. 519–521, 2004.

[32] R. Appleby, D. G. Gleed, R. N. Anderton, and A. H. Lettington, "Advances in passive millimeter wave imaging," M. N. Afsar, Ed., vol. 2211, no. 1. SPIE, 1994, pp. 312–317.

[33] R. Appleby, R. N. Anderton, S. Price, N. A. Salmon, G. N. Sinclair, J. R. Borrill, P. R. Coward, V. P. Papakosta, A. H. Lettington, and D. A. Robertson, "Compact real-time (video rate) passive millimeter-wave imager," R. M. Smith, Ed., vol. 3703, no. 1. SPIE, 1999, pp. 13–19.

[34] G. N. Sinclair, R. Appleby, P. R. Coward, and S. Price, "Passive millimeter-wave imaging in security scanning," R. M. Smith and R. Appleby, Eds., vol. 4032, no. 1. SPIE, 2000, pp. 40–45.

[35] D. Sheen, D. McMakin, and T. Hall, "Three-dimensional millimeter-wave imaging for concealed weapon detection," *Microwave Theory and Techniques, IEEE Transactions on*, vol. 49, no. 9, pp. 1581–1592, Sep 2001.

[36] S. Nolen, J. A. Koch, N. G. Paulter, C. D. Reintsema, and E. N. Grossman, "Antenna-coupled niobium bolometers for millimeter-wave imaging arrays," R. J. Hwu and K. Wu, Eds., vol. 3795, no. 1. SPIE, 1999, pp. 279–286.

[37] A. Luukanen, E. Grossman, A. Miller, P. Helistö, J. Penttilä, H. Sipola, and H. Seppä, "An ultra-low noise superconducting antenna-coupled microbolometer with a room-temperature read-out," *IEEE Microwave and Wireless Components Letters*, vol. 16, no. 8, pp. 464–466, August 2006.

[38] T.-L. Hwang, D. B. Rutledge, and S. E. Schwarz, "Planar sandwich antennas for submillimeter applications," *Applied Physics Letters*, vol. 34, pp. 9–11, Jan. 1979.

[39] B. Contreras and O. Gaddy, "Heterodyne detection at 10.6 m with thin-film bolometers," *Applied Physics Letters*, vol. 18, no. 7, pp. 277–278, April 1971.

[40] F. Gonzalez, B. Ilic, J. Alda, and G. Boreman, "Antenna-Coupled Infrared Detectors for Imaging Applications," *IEEE Journal of Selected Topics in Quantum Electronics*, vol. 11, no. 1, 2005.

[41] M. MacDonald and E. Grossman, "Niobium microbolometers for far-infrared detection," *IEEE Transactions on Microwave Theory and Techniques*, vol. 43, no. 4, pp. 893–895, April 1995.

[42] F. Ulaby, R. Moore, and A.Fung, *Microwave Remote Sensing: Active and Passive*, ser. Microwave Remote Sensing: Fundamentals and Radiometry. Artech-House, 1981, vol. 1.

[43] M. D. Ramírez, C. R. Dietlein, E. Grossman, and Z. Popović, "Unsupervised image segmentation for passive thz broadband images for concealed weapon detection," J. O. Jensen and H.-L. Cui, Eds., vol. 6549, no. 1. SPIE, 2007, p. 65490J.

[44] J. Dyson, "The Equiangular Spiral Antenna," *IEEE Transactions on Antennas and Propagation*, vol. 7, no. 4, pp. 329– 334, October 1959.

[45] C. Balanis, *Antenna Theory: Analysis and Design*, 3rd ed. Wiley-Interscience, 2005.

[46] D. B. Rutledge, D. P. Neikirk, and D. Kasilingam, "Integrated-circuit antennas," *Millimeter Components and Techniques*, vol. 11, no. Part II, 1984.

[47] C. R. Dietlein, "Components and metrology for terahertz imaging," Ph.D. dissertation, University of Colorado at Boulder, 2008.

[48] C. Dietlein, J. Chisum, M. Ramirez, A. Luukanen, E. Grossman, and Z. Popovic, "Integrated microbolometer antenna characterization from 95-650 GHz," *Microwave Symposium, 2007. IEEE/MTT-S International*, pp. 1165–1168, June 2007.

[49] G. Rebeiz, "Millimeter-wave and terahertz integrated circuit antennas," *Proceedings of the IEEE*, vol. 80, pp. 1748–1769, November 1992.

[50] P. F. Goldsmith, *Quasioptical Systems*, J. B. Anderson, Ed. IEEE Press, 1998.

[51] A. R. Luukanen and V.-P. Viitanen, "Terahertz imaging system based on antenna-coupled microbolometers," *Proc. SPIE Vol. 3378, p. 34-44, Passive Millimeter-Wave Imaging Technology II, Roger M. Smith; Ed.*, pp. 34–44, Aug. 1998.

[52] A. Luukanen and J. P. Pekola, "A superconducting antenna-coupled hot-spot microbolometer," *Applied Physics Letters*, vol. 82, pp. 3970–3972, June 2003.

[53] A. Luukanen, E. Grossman, A. Miller, P. Helisto, J. Pentilla, H. Sipola, and H. Seppa, "An ultra-low noise superconducting antenna-coupled microbolometer with a room-temperature readout," *Microwave and Wireless Components Letters*, vol. 16, no. 8, pp. 464– 466, August 2006.

[54] L. Jimenez, J. Rivera-Medina, E. Rodriguez-Diaz, E. Arzuaga-Cruz, and M. Ramirez-Velez, "Integration of spatial and spectral information by means of unsupervised extraction and classification for homogenous objects applied to multispectral and hyperspectral data," *IEEE Transactions on Geoscience and Remote Sensing*, vol. 43, no. 4, pp. 844– 851, April 2005.

[55] L. O. Jimenez-Rodriguez and J. Rivera-Medina, "Integration of spatial and spectral information in unsupervised classification for multispectral and hyperspectral data," *Proc. SPIE, Image and Signal Processing for Remote Sensing V*, vol. 3871, pp. 24–33, December 1999.

[56] R. Duda, P. Hart, and D. Stork, *Pattern Classification*. Wiley Interscience, 2000.

[57] T. Hastie, R. Tibshirani, and J. Friedman, *The Elements of Statistical Learning : Data Mining, Inference, and Prediction*, 1st ed., ser. Springer Series in Statistics. Springer, 2003.

[58] R. Duda, P. Hart, and D. Stork, *Pattern Classification*, 2nd ed. Wiley and Sons, 2000.

[59] J. S. Penttilä, H. Sipola, P. Helistö, and H. Seppä, "Low-noise readout of superconducting bolometers based on electrothermal feedback," *Superconductor Science Technology*, vol. 19, pp. 319–322, 2006.

[60] A. H. Lettington, Q. H. Hong, and D. G. Gleed, "Removing line patterns from infrared and passive millimeter wave images," A. G. Tescher, Ed., vol. 2298, no. 1. SPIE, 1994, pp. 208–214.

[61] G. C. Holst, *Testing and evaluation of infrared imaging systems*, 2nd ed. SPIE Optical Engineering Press, 1998.

[62] P. Mouroulis and J. Macdonald, *Geometrical optics and optical design*, ser. Oxford Series in Optical and Imaging Sciences. Oxford Univ. Press, 1997, vol. Vol.7.

[63] C. A. Bryant and J. B. Gunn, "Noncontact technique for the local measurement of semiconductor resistivity," *Review of Scientific Instruments*, vol. 36, no. 11, pp. 1614–1617, 1965.

[64] B. T. Rosner and D. W. van der Weide, "High-frequency near-field microscopy," *Review of Scientific Instruments*, vol. 73, no. 7, pp. 2505–2525, 2002.

[65] E. Ash and G. Nichols, "Super-resolution aperture scanning microscope," *Nature*, no. 237, pp. 510 – 512, June 1972.

[66] J. D. Chisum, M. Ramirez-Velez, and Z. Popovic, "Planar circuits for non-contact near-field microwave probing," *European Microwave Conference*, Submitted 2009.

[67] R. E. Collins, *Foundations for Microwave Engineering*, 2nd ed. Wiley-IEEE Press, 2001.

[68] H. Berger, "Uber das electrenkephalogramm des menchen," *Archiv fr Psychiatrie und Nervenkrankheiten*, vol. 87, pp. 527–570, 1929.

[69] S. Blanco, R. Q. Quiroga, O. A. Rosso, and S. Kochen, "Time-frequency analysis of electroencephalogram series," *Physical Review E*, vol. 51, pp. 2624–2631, 1995.

[70] C. Yamaguchi, "Fourier and wavelet analyses of normal and epileptic electroencephalogram (EEG)," *Proceedings of the First International IEEE-EMBS Conference on Neural Engineering*, pp. 406–409, March 2003.

[71] I. Osorio, M. Harrison, Y. Cheng-Lai, and M. Frei, "Observations on the application of correlation dimension and correlation integral to the prediction of seizures," *Journal of Clinical Neurophysiology*, vol. 18,3, pp. 269–274, 2001.

[72] K. Lehnertz and C. E. Elger, "Can epileptic seizures be predicted? evidence from nonlinear techniques time series analysis of brain electrical activity," *Physical Review Letters*, vol. 80, no. 22, pp. 5019–5022, June 1998.

[73] F. Chung, "Spectral graph theory," ser. Regional Conference Series in Mathematics, vol. 92, CBMS Conference on Recent Advances in Spectral Graph Theory. American Mathematical Society, 1997.

[74] S. Roweis and L. Saul, "Nonlinear dimensionality reduction by locally linear embedding," *Science*, vol. 290, pp. 2323–2326, December 2000.

[75] L. Saul and S. Roweis, "Think globally, fit locally: Unsupervised learning of low dimensional manifolds," *Journal of Machine Learning Research*, pp. 119–155, June 2003.

[76] V. Cherkassky and F. Mulier, *Learning from Data: Concepts, Theory, and Methods.* Wiley and Sons, 1998.

[77] M. Ramírez-Vélez, R. Staba, D. Barth, and F. Meyer, "Nonlinear classification of eeg data for seizure detection," *Imaging Nano to Macro, 2006, 3rd IEEE International Symposium on*, pp. 956–959, April 2006.

[78] T. Hastie, R. Tibshirani, and J. Friedman, *The Elements of Statistical Learning.* Springer, 2001.

[79] J. Cardoso, "Sources separation using higher order moments," *Proceedings of the International Conference on Acoustic, Speech and Signal Processing*, pp. 2109–2112, 1989.

[80] P. Comon, "Independent component analysis, a new concept?" *Signal Processing*, vol. 36, pp. 287–314, 1994.

[81] P. Grassberger and I. Procaccia, "Measuring the strangeness of strange attractors," *Physica D*, vol. 9, pp. 189–208, October 1983.

[82] D. Montgomery, E. Peck, and G. Vining, *Introduction to Linear Regression Analysis*, third edition ed. John Wiley and Sons, Inc., 2001.

[83] G. Healey and D. Slater, "Models and methods for automated material identification in hyperspectral imagery acquired under unknown illumination and atmospheric conditions," *IEEE Transactions on Geoscience and Remote Sensing*, vol. 37-6, pp. 2706–2717, 1999.

[84] R. Q. Quiroga, "Time-frequency methods and chaos theory," Ph.D. dissertation, Medical University of Lübeck, Germany, May 1998.

[85] M. Belkin and P. Niyogi, "Laplacian eigenmaps for dimensionality reduction and data representation," *Neural Comput.*, vol. 15, no. 6, pp. 1373–1396, 2003.

[86] ——, "Semi-supervised learning on riemannian manifolds," *Journal of Machine Learning*, vol. 56, pp. 209–239, July 2004.

[87] V. Vapnik, *Statistical Learning Theory.* Wiley and Sons, 1998.

[88] B. Scholkopf and A. Smola, *Learning with Kernels.* MIT Press, 2002.

[89] J. Tenenbaum and V. Silva, "A global geometric framework for dimensionality reduction," *Science*, vol. 290, pp. 2319–2323, December 2000.

[90] J. Shi and J. Malik, "Normalized cuts and image segmentation," *IEEE Transactions on Pattern Analysis and Machine Intelligence*, vol. 22, pp. 888–905, August 2000.

[91] G. Grudic, "Machine learning course notes," University of Colorado at Boulder, 2005.

[92] P. Gallois, G. Forzy, T. Morineaux, and L. Peyrodie, "Multi-channel analysis of the eeg signals and statistic particularities for epileptic seizure forecast," *Proceedings of the Second Joint EMBS/BMES Conference*, pp. 208–215, October 2002.

[93] H. Lee and S. Choi, "Pca+hmm+svm for eeg classification," *Proc. Int. Symp. Signal Processing and its Applications*, 2003.

[94] D. de Ridder and R. Duwin, "Locally linear embedding for classification," Delft University of Technology, Tech. Rep., 2002.

[95] S. Lang, *Differential and Riemannian Manifolds.* Springer-Verlag, 1995.

[96] D. B. West, *Introduction to Graph Theory.* Prentice Hall, 2000.

[97] M. S. Jones and D. S. Barth, "Spatiotemporal organization of fast (.200 hz) electrical oscillations in rat vibrissa/barrel cortex," *Journal of Neurophysiology*, vol. 82, pp. 1599–1609, September 1999.

[98] J. Sprott, *Chaos and Time Series Analysis.* Oxford, 2003.

[99] M. Ramírez-Vélez and F. G. Meyer, "Nonlinear classification of EEG data for seizure detection," University of Colorado at Boulder, Tech. Rep., 2006.

[100] K. Lehnertz, "Nonlinear EEG analysis in epilepsy: From basic research to clinical applications," *Proceedings of the Second Joint EMBS/BMES Conference*, pp. 25–27, October 2002.

[101] J. R. L. Morrison and J. D. C. Munson, "An experimental study of a new entropy-based sar autofocus technique," *Proc. of the IEEE International Conference on Image Processing*, pp. 441–444, 2002.

[102] P. T. A. Achim and A. Bezerianos, "Sar image denoising via bayesian wavelet shrinkage based on heavy-tailed modeling," *IEEE Transactions on Geoscience and Remote Sensing*, vol. 41, 2003.

[103] M. D. R.L. Morrison and D. Munson, "Sar image autofocus by sharpness optimization: A theoretical study," *IEEE Transactions on Image Processing*, vol. 16, September 2007.

[104] Authors, "Nonlinear classification of EEG data for seizure detection," University of Colorado at Boulder, Tech. Rep., 2006.

[105] R. Hadfield, A. Miller, a. S. R. Nam, S.W, and E. Grossman, "Antenna coupled niobium bolometers for 10 um wavelength radiation detection," *IEEE Transactions on Applied Superconductivity*, vol. 15, no. 2, pp. 541– 544, June 2005.

[106] A. Luukanen, R. H. Hadfield, A. J. Miller, and E. N. Grossman, "A superconducting antenna-coupled microbolometer for thz applications," *Terahertz for Military and Security Applications II. Edited by Hwu, R. Jennifer; Woolard, Dwight L. Proceedings of the SPIE, Volume 5411, pp. 121-126 (2004).*, pp. 121–126, Sept. 2004.

[107] A. Luukanen, A. J. Miller, and E. N. Grossman, "Passive hyperspectral terahertz imagery for security screening using a cryogenic microbolometer," *Passive Millimeter-Wave Imaging Technology VIII. Edited by Appleby, Roger; Wikner, David A. Proceedings of the SPIE, Volume 5789, pp. 127-134 (2005).*, pp. 127–134, May 2005.

[108] A. J. Miller, A. Luukanen, and E. N. Grossman, "Micromachined antenna-coupled uncooled microbolometers for terahertz imaging arrays," *Terahertz for Military*

and Security Applications II. Edited by Hwu, R. Jennifer; Woolard, Dwight L. Proceedings of the SPIE, Volume 5411, pp. 18-24 (2004)., pp. 18–24, Sept. 2004.

[109] R. Driggers, P. Cox, and T. Edwards, *Introduction to Infrared and Electro-Optical Systems.* Artech House, 1998.

[110] A. S. Weling, P. F. Henning, D. P. Neikirk, and S. Han, "Antenna-coupled microbolometers for multispectral infrared imaging," *Infrared Technology and Applications XXXII. Edited by Andresen, Bjørn F.; Fulop, Gabor F.; Norton, Paul R.. Proceedings of the SPIE, Volume 6206, pp. (2006).*, 2006.

[111] T. Hastie, R. Tibshirani, and J. Friedman, *The Elements of Statistical Learning.* Springer, 2001.

[112] T. Yamasaki and D. Gingras, "Image classification using spectral and spatial information based on MRF models," *IEEE Trans. on Image Processing*, vol. 4, no. 9, pp. 1333–1339, September 1995.

[113] F. J. Gonzalez, J. L. Porter, and G. D. Boreman, "Antenna-coupled infrared detectors," in *Infrared Technology and Applications XXX. Edited by Andresen, Bjorn F.; Fulop, Gabor F. Proceedings of the SPIE, Volume 5406, pp. 863-871 (2004).*, B. F. Andresen and G. F. Fulop, Eds., Aug. 2004, pp. 863–871.

[114] M. Belkin, "Problems of learning manifolds," Ph.D. dissertation, University of Chicago, Chicago, Illinois, August 2003.

[115] Tech. Rep.

[116]

[117] E. Grossman, "The coupling of submillimeter corner-cube antennas to Gaussian beams," *Infrared Physics*, vol. 29, no. 5, pp. 875–885, 1989.

[118] H. Stark and J. Woods, *Probability and Random Processes*, 3rd ed. Prentice Hall, 2002.

[119] J. D. Dyson, "The equiangular spiral antenna." *Ph.D. Thesis*, 1957.

[120] G. Bendor and T. Gedra, "Single-pass fine-resolution sar autofocus," *Proc. IEEE Nat. Aerospace Elect. Conf. (NAECON)*, 1983.

[121] W. Ye, T. S. Yeo, and Z. Bao, "Weighted least-squares estimation of phase errors for sar/isar autofocus," *Geoscience and Remote Sensing, IEEE Transactions on*, vol. 37, no. 5, pp. 2487–2494, Sep 1999.

[122] K. D. Wulff, D. G. Cole, R. L. Clark, R. DiLeonardo, J. Leach, J. Cooper, G. Gibson, and M. J. Padgett, "Aberration correction in holographic optical tweezers," *Opt. Express*, vol. 14, no. 9, pp. 4169–4174, 2006.

[123] J. Morrison, R.L. and M. Do, "A multichannel approach to metric-based sar autofocus," *Image Processing, 2005. ICIP 2005. IEEE International Conference on*, vol. 2, pp. II–1070–3, Sept. 2005.

[124] A. H. Lettington, D. Dunn, M. Attia, and I. M. Blankson, "Passive millimetre-wave imaging architectures," *Journal of Optics A: Pure and Applied Optics*, vol. 5, no. 4, pp. S103–S110, 2003.

[125] L. Zhang, J. Stiens, A. Elhawil, and R. Vounckx, "Multispectral illumination and image processing techniques for active millimeter-wave concealed object detection," *Appl. Opt.*, vol. 47, no. 34, pp. 6357–6365, 2008.

[126] M. C. Kemp, P. F. Taday, B. E. Cole, J. A. Cluff, A. J. Fitzgerald, and W. R. Tribe, "Security applications of terahertz technology," R. J. Hwu and D. L. Woolard, Eds., vol. 5070, no. 1. SPIE, 2003, pp. 44–52.

[127] R. Appleby and R. Anderton, "Millimeter-wave and submillimeter-wave imaging for security and surveillance," *Proceedings of the IEEE*, vol. 95, no. 8, pp. 1683–1690, Aug. 2007.

[128] H.-M. Chen, S. Lee, R. Rao, M.-A. Slamani, and P. Varshney, "Imaging for concealed weapon detection: a tutorial overview of development in imaging sensors

and processing," *Signal Processing Magazine, IEEE*, vol. 22, no. 2, pp. 52–61, March 2005.

[129] L. Zhang, J. Stiens, A. Elhawil, and R. Vounckx, "Multispectral illumination and image processing techniques for active millimeter-wave concealed object detection," *Appl. Opt.*, vol. 47, no. 34, pp. 6357–6365, 2008.

[130] E. N. Grossman and A. J. Miller, "Active millimeter-wave imaging for concealed weapons detection," R. Appleby, D. A. Wikner, R. Trebits, and J. L. Kurtz, Eds., vol. 5077, no. 1.   SPIE, 2003, pp. 62–70.

[131] D. Sheen, D. McMakin, and T. Hall, "Three-dimensional millimeter-wave imaging for concealed weapon detection," *Microwave Theory and Techniques, IEEE Transactions on*, vol. 49, no. 9, pp. 1581–1592, Sep 2001.

[132] R. Appleby and H. Wallace, "Standoff detection of weapons and contraband in the 100 ghz to 1 thz region," *Antennas and Propagation, IEEE Transactions on*, vol. 55, no. 11, pp. 2944–2956, Nov. 2007.

[133] A. Luukanen, L. Gronberg, T. Haarnoja, P. Helisto, K. Kataja, M. Leivo, A. Rautiainen, J. Penttila, J. E. Bjarnason, C. R. Dietlein, M. D. Ramirez, and E. N. Grossman, "Passive thz imaging system for stand-off identification of concealed objects: results from a turn-key 16 pixel imager," R. Appleby and D. A. Wikner, Eds., vol. 6948, no. 1.   SPIE, 2008.

[134] S. Kalinin and A. Gruverman, *Scanning Probe Microscopy*, ser. Electrical and Electromechanical Phenomena at the Nanoscale. Springer New York, 2007, vol. 1.

[135] C.-I. Chang and H. Ren, "An experiment-based quantitative and comparative analysis of target detection and image classification algorithms for hyperspectral data," *IEEE Transactions on Geoscience and Remote Sensing*, vol. 38-2, pp. 1044–1063, 2000.

[136] F. D. A. Chein-I Chang, Hsuan Ren and J. O. Jensen, "Subpixel target size estimation for remotely sensed imagery," *Proceedings of SPIE : Algorithms and Technologies for Multispectral, Hyperspectral and Ultraspectral Imagery IX*, vol. 5093, pp. 398–407, 2003.

[137] S. Rosario-Torres, "Iterative algorithms for abundance estimation on unmixing of hyperspectral imagery," Master's thesis, University of Puerto Rico at Mayaguez, Mayaguez, Puerto Rico, 2004.

[138] R. P. Antonio Plaza, Pablo Martinez and J. Plaza, "Spatial/spectral endmember extraction by multidimensional morphological operators," *IEEE Transactions on Geoscience and Remote Sensing*, vol. 40, no. 9, pp. 2025–2041, September 2002.

[139] R. Clark, G. Swayze, R. Wise, K. Livo, T. Hoefen, R. Kokaly, and S. Sutley, "Usgs digital spectral library," United States Geological Survey, Tech. Rep., 2003.

[140] C.-I. Chang, *Hyperspectral Imaging: Techniques for Spectral Detection and Classification.* Springer, 2003.

[141] C. Gao and X.-D. Xiang, "Quantitative microwave near-field microscopy of dielectric properties," *Review of Scientific Instruments*, vol. 69, no. 11, pp. 3846–3851, 1998.